




Universitetet
i Stavanger

FACULTY OF SCIENCE AND TECHNOLOGY

MASTER'S THESIS

Study program/specialization: Master of Science in Energy & Petroleum Engineering/ Drilling Engineering	Spring semester, 2023 Open access
Author: Stine Lise Landaas	 _____ (Author's signature)
Supervisor(s): Dr. Mahmoud Khalifeh Dr. Reidar Inge Korsnes	
Title of master's thesis: Investigating the Necessity of Standardized In-Situ Testing Procedures for One-Part Granite-based Geopolymers: An Experimental Study of the Influence of Loading Rate	
Credits: 30 ECTS	
Keywords: Rock mechanical Properties Stress and strain Granite-based Geopolymers Triaxial Testing Loading Rate	Number of pages: 121 Stavanger, 1 st July 2023

**Investigating the Necessity of Standardized In-Situ Testing Procedures
for One-Part Granite-based Geopolymers: An Experimental Study of the
Influence of Loading Rate**

Written by

Stine Lise Landaas

Master's thesis

Presented to the Faculty of Science and Technology

The University of Stavanger

THE UNIVERSITY OF STAVANGER

JULY 2023

Acknowledgements

I would like to express my outer gratitude and acknowledge to the following individuals, institution, and organization who have contributed to the successful completion of my mater thesis.

First and foremost, I would like to acknowledge and extend my appreciation to the Research Council of Norway (RCN) for their financial support through the founding of the Centre for Research-based Innovation “SWIPA - Centre for Subsurface Well Integrity, Plugging and Abandonment,” (RCN proj. no. 309646). This founding has been instrumental in enabling me to carry out the experimental work portion presented in this thesis.

I am also grateful to the Department of Energy and Petroleum Engineering at UiS for providing me with the opportunity to pursue my studies and undertake this research project on the JAW-B geopolymers with SafeRock.

I would like to express my deep appreciation to TotalEnergies, AkerBP, ConocoPhillips and the Research Council of Norway for their financial support the SafeRock KPN Project (RCN #319014) at the University of Stavanger, Norway. Their contribution and support have greatly enhanced the resources and facilities available for this research.

I am indebted to my supervisors Dr. Mahmoud Khalifeh and Dr. Reidar Inge Korsnes, for the opportunity, guidance, expertise and invaluable support throughout my research process. Their insights and advice greatly help me carry out the experimental testing and writing of this thesis. I would also like to express my gratitude to Seyed Hassan Hajiabadi and Jostein Djuve for their training and guidance during the laboratory preparation of test samples of JAW-B geopolymers. Their assistance and expertise have been indispensable to conducting and improving the preparation of the geopolymers samples.

I would like to extend a special mention goes out to my fellow student research partners Pedram Gargari and Vidar Sandvik. Their collaboration and positive spirits have made the research a joyful and enjoyable journey.

Lastly, I must express my heartfelt appreciation to my family for their unwavering support, encouragement and understanding throughout my years at university and during the process of researching and writing this thesis. This thesis would not have been possible without their help.

In conclusion, the contribution of the following individuals, institution, and organization have made this master thesis possible. I am sincerely grateful for their encouragement, assistance, mentorship throughout this endeavour.

Stine Lise Landaas

Stavanger, 2023

Abstract

Ordinary Portland cement (OPC) is the most popular choice for cementing material for petroleum well cementing. Since cement is used in the petroleum industry as an essential part of creating zonal isolation and ensuring well integrity during and after decommissioning. The drawback with using OPC is responsible for 8% of the worlds carbon dioxide emissions and to produce one tonne of OPC, emits 0.9 tonne of CO₂. Hence the objective of this thesis to test if a rock geopolymer cement can be an alternative to OPC. Which have up to 80% less emission of CO₂ compared to OPC.

Table 1 Summary of load rate impact on average compressive strength

Piston load rate [MPa/min]	Confining pressure [MPa]	Average compressive strength [MPa] Deviatoric phase 0.2 % offset
0.5	8	18
12	8	20
High	8	18.25
0.5	17.2	21
12	17.2	28
High	17.2	28
0.5	26	34.75
12	26	35.75
High	26	40.25

This thesis is one part of a three-part study of the properties to the rock based geopolymer Just add water (JAW-B). JAW-B is a granite-based rock-based polymer where all the activators are in the dry phase and only water is to be added to make the cement. The objective of thesis is to test the impact of different loading rates on the in-situ mechanical properties of the rock-based geopolymer JAW-B. A triaxial cell was used to simulate the downhole conditions and in-situ stress conditions of a petroleum wellbore. The test samples of JAW-B were prepared and cured for one week at 90°C at 2000 psi. A total of 18 JAW-B test samples were prepared and subjected to nine tests, each with duplicates, utilizing three different loading rates (0.5, 12, and 17.97+ MPa/min) and three distinct confining pressures

(8, 17.2, and 26 MPa) Table 1 presents a summary of the different load rates and confining pressure used in this theses.

Regarding Young's modulus, holding the piston load rate constant at 0.5 MPa/min and increasing the confining pressure from 8 MPa to 17.2 MPa resulted in a change in Young's modulus from a range of 0.71-0.73 GPa to 0.51-0.72 GPa. Further increasing the confining pressure from 17.2 MPa to 26 MPa led to an increase in Young's modulus to 1.01-1.09 GPa. Similarly, when holding the piston load rate constant at 12 MPa/min, increasing the confining pressure resulted in an increase in Young's modulus. A similar trend was observed for a piston load rate range of 17.97-23.3 MPa/min. Overall, increasing the confining pressure led to an increase in Young's modulus.

Poisson's ratio was also examined in relation to confining pressure and piston loading rate. The results showed that increasing the confining pressure generally resulted in changes in Poisson's ratio, except for the case of a piston load rate of 0.5 MPa/min, where no noticeable change was observed. Increasing the piston loading rate generally led to an increase in Poisson's ratio, indicating that the samples became more ductile as the applied stress increased.

The compressive strength of the samples was influenced by both confining pressure and piston loading rate. Increasing the confining pressure generally led to an increase in compressive strength, while the effect of piston loading rate was more variable and dependent on other factors.

The bulk modulus of JAW-B was found to increase as the confining pressure increased from 8 to 26 MPa. This suggests that the material became less compressible and more resistant to changes in shape or volume under higher confining pressures.

In conclusion, this study demonstrates that changes in both confining pressure and piston loading rate can significantly impact the mechanical properties of JAW-B.

Based on the results of this thesis, it is recommended to conduct further testing on JAW-B geopolymer at low and high piston load rates under a confining pressure of 8 MPa. To qualify and establish a standard for JAW-B as an OPC substitute in well cementing, further testing

against OPC benchmark properties is required. The obtained results are promising, but additional testing is necessary to ensure quality.

Acronyms

ν – Poisson's ratio

E – Young's modulus

K – Bulk modulus

Pa – Pascal (Pressure unit)

psi - pound per square inch

min – minutes

s – seconds

ml – millilitres

M – Mega [10^6]

G – Giga [10^9]

OPC – Ordinary Portland Cement

AAFA – Alkali activated fly ash

List of Contents

Acknowledgements	3
Abstract	5
List of Contents	9
Figure list.....	12
Table list.....	16
1. Introduction	17
1.1 Objective	18
2. Literature review section.....	18
2.1 Petroleum well life cycle.....	18
2.1.1 Drilling	19
2.1.2 Completion.....	21
2.1.3 Production	21
2.1.4 Plug and Abandonment	21
2.1.5 Challenges when doing P&A	22
2.1.6 Well Integrity NORSOK-D10.....	22
2.1.7 Well barrier elements	23
2.1.8 Well barrier.....	23
2.2 Portland cement.....	24
2.2.1 Challenges with Ordinary Portland cement	26
2.2.2 CO ₂ emission during manufacturing	27
2.3 Geopolymer.....	27
2.3.1 Possible replacement for OPC.....	28
2.3.2 Rock-based geopolymer manufacturing:.....	29
2.4 Rock mechanics.....	30
2.4.1 Stress	31

2.4.2 Strain	33
2.4.3 Hooke's law and Young's modulus	35
2.4.4 Poisson's ratio	37
2.4.5 Compressive strength	38
2.5 Triaxial Cell.....	38
2.5.1 Triaxial cells test sample requirements	39
2.5.2 Triaxial laboratory equipment	40
2.5.3 Purpose of hydrostatic test (hydrostatic phase).....	42
2.5.4 Purpose of triaxial compression test (deviatoric phase).....	42
2.5.5 Data Utilisation	43
3. Experimental Methodology and Experimental set up	43
3.1 Preparation of JAW-B Geopolymer test samples.....	43
3.1.1 Preparation of equipment and weighing of dry and liquid components.....	44
3.1.2 Mixing dry phase and liquid phase	45
3.1.3 Preparing the consistometer and conditioning the geopolymer slurry	46
3.1.4 Greasing of moulds	48
3.1.5 Filling of moulds with geopolymer slurry and placing the moulds in an autoclave cell.....	49
3.1.6 Curing of samples.....	50
3.1.7 Removal of autoclave cell from the oven	51
3.1.8 Removal of test moulds from autoclave cell.....	51
3.1.9 Measuring, marking and cutting the test sample.....	52
3.1.10 Polishing of test samples	53
3.2 Triaxial cell testing	55
3.2.1 Triaxial cell preparation	55
3.2.2 Triaxial cell assembly.....	57
3.2.3 Placing the confining chamber and assembling the triaxial cell	60

3.2.4 Pump and logging program setup.....	62
3.2.5 Increasing of confining pressure to 0.5 MPa.....	63
3.2.6 Lowering piston	65
3.2.7 Increasing of temperature to 90°C	66
3.2.8 Triaxial cell sample test.....	67
3.2.9 Cooling of the triaxial cell and lifting of piston to start position	69
3.2.10 Disassembly of the triaxial cell	71
3.3 Data analysing methods	71
3.3.1 Hydrostatic loading phase	72
3.3.2 Deviatoric loading phase	75
4. Results and Discussion.....	78
4.1 Hydrostatic phase	79
4.1.1 Confining pressure of 8 MPa	80
4.1.2 Confining pressure 17.2 MPa.....	87
4.1.3 Confining pressure 26 MPa.....	95
4.1.4 Discussion of the hydrostatic phase	99
4.2 Deviatoric phase	100
4.2.1 Piston load rate 0.5 MPa/min	100
4.2.2 Piston Load rate 12 MPa/ min.....	103
4.2.3 Piston Load rate 17.97 to 23.3 MPa/min.....	105
4.2.4 Different load rates at confining pressure 8 MPa.....	107
4.2.5 Different load rates at confining pressure 17.2 MPa.....	108
4.2.6 Different load rates at confining pressure 26 MPa.....	110
4.2.7 Discussion of the Deviatoric phase	111
4.3 Future improvement for testing JAW-B samples using a triaxial cell	113
5. Conclusion.....	114
References	119

Figure list

Figure 1 Lifecycle of a Petroleum well	18
Figure 2 Figure 2 Example of a typical vertical wellbore schematic (Crumpton 2018 p.67)	19
Figure 3 Cross-section of a cemented wellbore	20
Figure 4 Example from NORSOK on a two-barrier envelope of permanent abandonment (NORSOK D-10, 2021, page 101)	23
Figure 5 Stress-strain diagram of sample 10 of JAW-B geopolymer	31
Figure 6 Tension and compression forces acting on a body	32
Figure 7 Local stress acting on a selected cross-sectional area ΔA_i (Fjær et al.2008, page 3).....	32
Figure 8 Illustration of a force acting on a surface yielding normal stress and shear stress	33
Figure 9 Normal strain (Middle) and Shear strain (Right) acting on a body	34
Figure 10 Sample SLL14 Illustrating Young's modulus in the elastic region of deformation	36
Figure 11 Illustration of difference of behaviour between a brittle(left) and a ductile material(right).....	36
Figure 12 Principal sketch of stress-strain diagram for a uniaxial compression test, illustrating the material behaviour from elastic to brittle. (Fjær et al., 2008 page 56).....	38
Figure 13 Effect of length and diameter ratio on uniaxial compressive strength of a rock sample [Fjær,2008].....	39
Figure 14 P&ID schematic of a triaxial cell without the water injection pump.....	40
Figure 15 Mixing cup and OFITE Model 20 Constant Speed Blender for cement mixing	46
Figure 16 Conditioner cup and mixing blade	47
Figure 17 OFITE model 60 Atmospheric consistometer used to condition the geopolymer	47
Figure 18 Setup of 4 curing cells, before greasing and assembly	48
Figure 19 Autoclave curing cell	49
Figure 20 Autoclave cell Inner (left) and Outer lid (right).....	50
Figure 21 Autoclave key	52
Figure 22 Discotom Cutting machine	52

Figure 23 Baldor GCTS RSG-75 cutting and polishing machine	53
Figure 24 Close up of sample lined up with the polishing surface	54
Figure 25 Baldor cutting, and polishing machine left side handle	54
Figure 26 Sample between drainage plates and water injection equipment.....	56
Figure 27 Water drainage plates and rubber rings	57
Figure 28 Bottom of the triaxial cell	57
Figure 29 Sample with 3/4 heated shrink sleeve.....	58
Figure 30 Top of water injection unit.....	58
Figure 31 GCTS Extensometer	59
Figure 32 Fully assembled test set-up on the inner part of the confining chamber of a triaxial cell.....	59
Figure 33 Confining chamber correctly placed on the bottom of the Triaxial cell	60
Figure 34 Confining pressure installed, from above and from the side	60
Figure 35 Top of triaxial cell (left) and installed top of the triaxial cell on the confining chamber	61
Figure 36 LVDT Axial movement logging equipment	61
Figure 37 Fully assembled triaxial cell	62
Figure 38 VPware the pump program used to control the pumps.....	63
Figure 39 Vidum VP-series High-Pressure Metering Pumps	64
Figure 40 LabView Logging program used to log data	64
Figure 41 Figure illustrating how the piston was lowered from the top to the sample	66
Figure 42 Pressure control valve used to regulate the pressure during heating of confining oil.....	67
Figure 43 LabView graph showing the initial position of the piston and its movement during the test.....	70
Figure 44 P&ID schematic of the triaxial cell and pump setup for piston and confining pumps	70
Figure 45 Geopolymer samples after the deviatoric phase (failed samples).....	71
Figure 46 How sample SLL14 axial stress was calculated in excel.....	72
Figure 47 How sample SLL14 axial strain was calculated in excel.....	73
Figure 48 How sample SLL14 radial strain was calculated in excel	73
Figure 49 How sample SLL14 volumetric strain was calculated in excel.....	74
Figure 50 How sample SLL14 isotropic volumetric strain was calculated in excel	74

Figure 51 Example on how the bulk modulus was derived method 1 and 2, with sample SLL18 as an example	74
Figure 52 Example on how the bulk modulus was found for isotropic volumetric stress-strain diagram with sample SLL18 used as an example	75
Figure 53 How deviatoric axial strain was calculated in excel (sample SLL14 as an example).....	75
Figure 54 How deviatoric radial strain was calculated in excel (sample SLL14 as an example).....	76
Figure 55 Deviator phase of sample 18 which depicts how the Young's modulus was found and how the compressive strength was estimated.....	77
Figure 56 Example on how Poisson's ratio was calculated, with sample SLL18 used as an example	77
Figure 57 Example on how the actual piston load rate was estimated.....	78
Figure 58 Example on how the values for the offset graph was calculated for sample SLL18.....	78
Figure 59 Axial strain for samples SLL8 to SLL13 with Confining pressure 8 MPa at an increase of 1.67 MPa/min.....	81
Figure 60 Radial strain for samples SLL18 to SLL13 with Confining pressure 8 MPa at an increase of 1.67 MPa/min.....	82
Figure 61 Volumetric strain for samples SLL8 to SLL13 with Confining pressure 8 MPa at an increase of 1.67 MPa/min.....	83
Figure 62 Isotropic volumetric strain based on axial strain only for samples SLL8 to SLL13 with Confining pressure 8 MPa at an increase of 1.67 MPa/min.....	84
Figure 63 Axial strain for all samples up to Confining pressure of 8 MPa at an increase of 1.67 MPa/min	85
Figure 64 Radial strain for all samples up to Confining pressure of 8 MPa at an increase of 1.67 MPa/min	86
Figure 65 Radial strain for all samples up to Confining pressure of 8 MPa at an increase of 1.67 MPa/min	86
Figure 66 Axial strain for samples SLL1 to SLL7 with confining pressure of 17.2 MPa at an increase of 1.67 MPa/min.....	89
Figure 67 Radial strain for samples SLL1 to SLL7 with confining pressure of 17.2 MPa at an increase of 1.67 MPa/min.....	90

Figure 68 Volumetric strain for samples SLL1 to SLL7 with confining pressure of 17.2 MPa at an increase of 1.67 MPa/min	91
Figure 69 Isotropic volumetric strain for samples SLL1 to SLL7 with confining pressure of 17.2 MPa at an increase of 1.67 MPa/min	92
Figure 70 Axial strain for all samples up to Confining pressure of 17.2 MPa at an increase of 1.67 MPa/min.....	93
Figure 71 Radial strain for all samples up to Confining pressure of 17.2 MPa at an increase of 1.67 MPa/min.....	94
Figure 72 Volumetric strain for all samples up to Confining pressure of 17.2 MPa at an increase of 1.67 MPa/min.....	94
Figure 73 Axial strain for samples SLL14 to SLL20 with confining pressure of 26 MPa at an increase of 1.67 MPa/min.....	96
Figure 74 Radial strain for samples SLL14 to SLL20 with confining pressure of 26 MPa at an increase of 1.67 MPa/min.....	97
Figure 75 Volumetric strain for samples SLL14 to SLL20 with confining pressure of 26 MPa at an increase of 1.67 MPa/min	98
Figure 76 Picture of sample SLL4 (left) after removal from mould and sample SLL8 (right) sample cut and polished	99
Figure 77 Deviatoric phase with piston load rate of 0.5 MPa/min with different confining pressures	102
Figure 78 SLL14 and SLL15 deviatoric phase comparison.....	102
Figure 79 Deviatoric phase with Piston load rate of 12 MPa/min with different confining pressures	104
Figure 80 Deviatoric phase with Piston load rate between 17.97 to 23.3 MPa/min with different confining pressures SLL13 is an outlier very high bulk modulus.....	106
Figure 81 Deviatoric loading phase at 8 MPa with different piston loading rates.....	108
Figure 82 Deviatoric loading phase at 17.2 MPa with different piston loading rates.....	109
Figure 83 Deviatoric loading phase at 26 MPa with different piston loading rates.....	111
Figure 84 Deviatoric phase of Adijat Ogienagbonb’s study of mechanical behaviour of cementing materials [Adijat Ogienagbonb, 2022]	113

Table list

Table 1 Summary of load rate impact on average compressive strength.....	5
Table 2 Standards for OPC cement from API 10 A (Khalifeh, Saasen, 2020, page 101)..	24
Table 3 JAW-B recipe.....	44
Table 4 Length, diameter and weight of samples before triaxial testing	55
Table 5 Test program	68
Table 6 Pump schedule values for the two test phases (Hydrostatic and Deviatoric).....	68
Table 7 Test results for hydrostatic phase for confining pressure 8 MPa at 90°C.....	80
Table 8 Test results for hydrostatic phase for confining pressure 17.2 MPa at 90°C.....	87
Table 9 Test results for hydrostatic phase for confining pressure 26 MPa at 90°C.....	95
Table 10 Results of test with piston loading rate 0.5 MPa/min	100
Table 11 Results of test with piston loading rate 12 MPa/min	103
Table 12 Results of test with piston loading rate between 17.97 to 23.3 MPa/min.....	105
Table 13 Results of the deviatoric phase at 8 MPa confining pressure with different piston load rates	107
Table 14 Results of the deviatoric phase at 17.2 MPa confining pressure with different piston load rates.....	108
Table 15 Results of the deviatoric phase at 26 MPa confining pressure with different piston load rates.....	110

1. Introduction

As the world advances towards its goal of achieving net-zero carbon dioxide emissions by 2050. There is an increasing need to explore sustainable alternatives to conventional materials and practices. The petroleum industry, like other sectors, is not exempt from the imperative to address the pressing issue of reducing CO₂ emissions. To align with global sustainability goals, the industry must embrace innovative solutions and adopt new materials to effectively mitigate their carbon footprint. One solution is to reduce the CO₂ emissions is by reducing the dependency of ordinary Portland cement (OPC) and concrete, which produces 0.9 tonnes of CO₂ per 1 tonne of OPC produced. The reason of the dependence of on OPC, is that OPC is relatively cheap and is the standard when it comes to well cementing and creating zonal isolation in the downhole. The downside besides the high CO₂ emissions is that the cement will easily get contaminated by different drilling fluids and have a brittle failure mode. Which in turn, impacts the ability of the OPC to bond to casing steel and formation and keep this bond intact as the formation moves due tectonic activities.

Geopolymer-based cements are a promising alternative to replace OPC as a well cementing material. As geopolymers have a lower CO₂ impact up to 90% of OPC production and have a more ductile failure mechanism. A property which allows the geopolymer to keep its bonding to formation and casing during changes due to temperature, pressure, and overburden pressure. Although unlike OPC, geopolymers does not currently have a set standard for its material properties. The standards for geopolymers must be established along developments of geopolymers through research and laboratory testing.

The development of a standard to geopolymers will be based on rock mechanics and laboratory testing for each recipe. Since the geopolymer cement will be subjected to the stresses and strains from the formation. A technique to simulate these downhole conditions is the usage of a triaxial cell. The triaxial cell test will provide the necessary data to determine the following mechanical properties bulk modulus, Young's modulus, Poisson's ratio and compressive strength.

1.1 Objective

This thesis intends to study the impact of axial loading on mechanical properties such as failure strength (Compressive strength), Young's modulus, and Poisson's ratio at a constant temperature with varying confining pressures. Stress-strain curves will be plotted to visualize the impact of axial loading on the mechanical properties of the Geopolymer JAW-B.

2. Literature review section

2.1 Petroleum well life cycle

A Petroleum well will through its life cycle go through four phases, drilling, completion, production and permanent plug and abandonment. Figure 1 below illustrates this life cycle. During three of the four phases, cement material is used to isolate the wellbore from the surrounding environment. The petroleum well is constructed in segments, like the vertical schematic illustrated in Figure 2 on the next page.

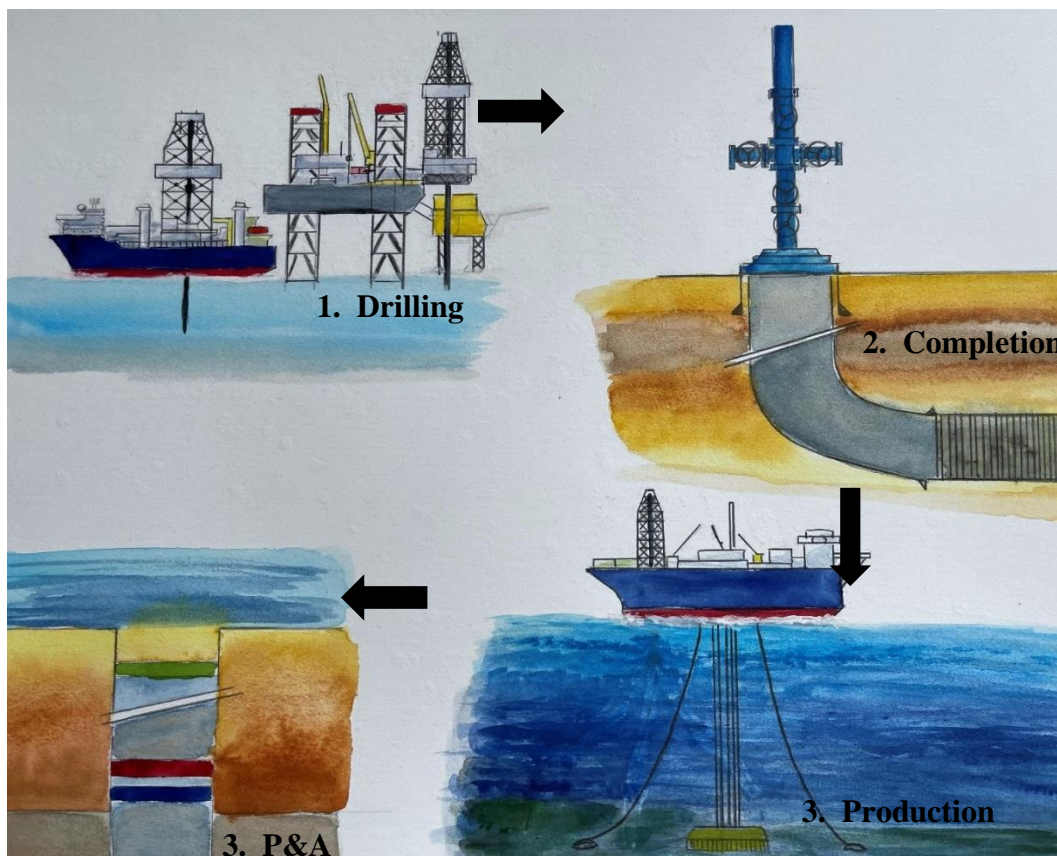


Figure 1 Lifecycle of a Petroleum well

2.1.1 Drilling

The drilling of a petroleum wellbore starts with drilling the surface conductor a 32” or 36” hole and setting the 30” casing and cementing. This will be the main space which will house the wellhead and bear the weight of the following segments. The next segment is called the surface casing, and it is usually cemented up to the conductor. Once the surface casing is cemented in place, a blow-out preventer is installed on the wellhead allowing for well control (Crumpton, 2018).

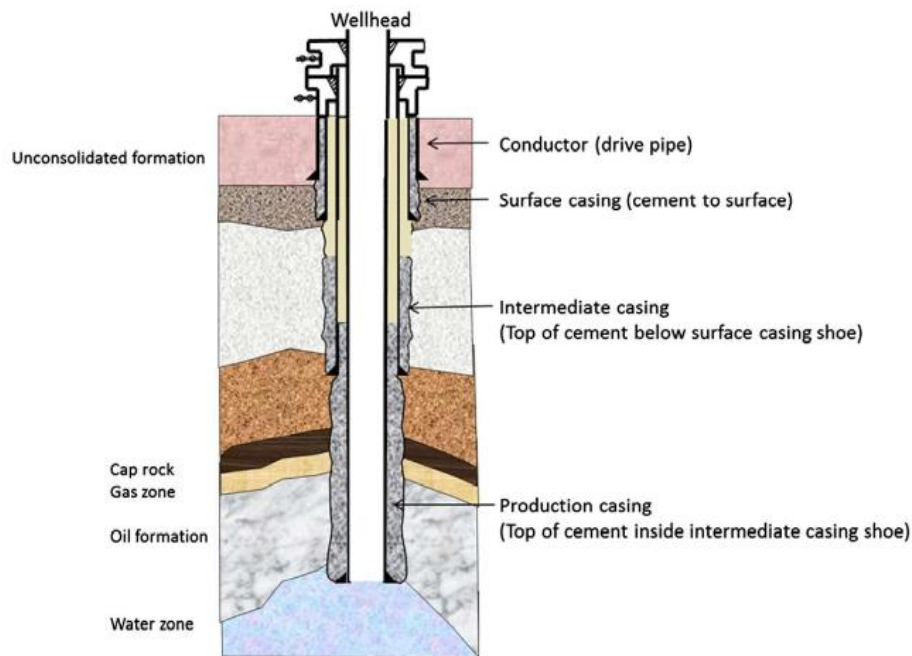


Figure 2 Example of a typical vertical wellbore schematic (Crumpton 2018 p.67)

The following segment is the intermediate segment. The segment used to deepen the wellbore. The cementing of this segment depends on the strengths of the formation and if the formation is permeable and fluid bearing. If the formation is weak or is not approved by governing regulations it needs to be isolated to maintain well integrity (Crumpton, 2018). The isolation is achieved by using cement.

If the cement of the intermediate segment is placed below the previous casing shoe. Then during permanent plug and abandonment the casing can be cut and pulled out. Or it allows for a side track, without drilling through casing cement. It also allows for gas or other fluids to

migrate to an overlaying porous formation, instead of building up pressure in the annular volume. Speciality when the temperature in the annular space increase during production.

Then the production casing is the last casing and in many wellbores is cemented up above the production interwall. Then the casing shoe of the production casing, cap rock is drilled, and a plug is set with in the wellbore. The wellbore is thereafter handed over to the completion engineers.

A casing is cemented in place, to establish a bonding and isolate the space between the formation and casing steel, which is illustrated in the Figure 3 below.

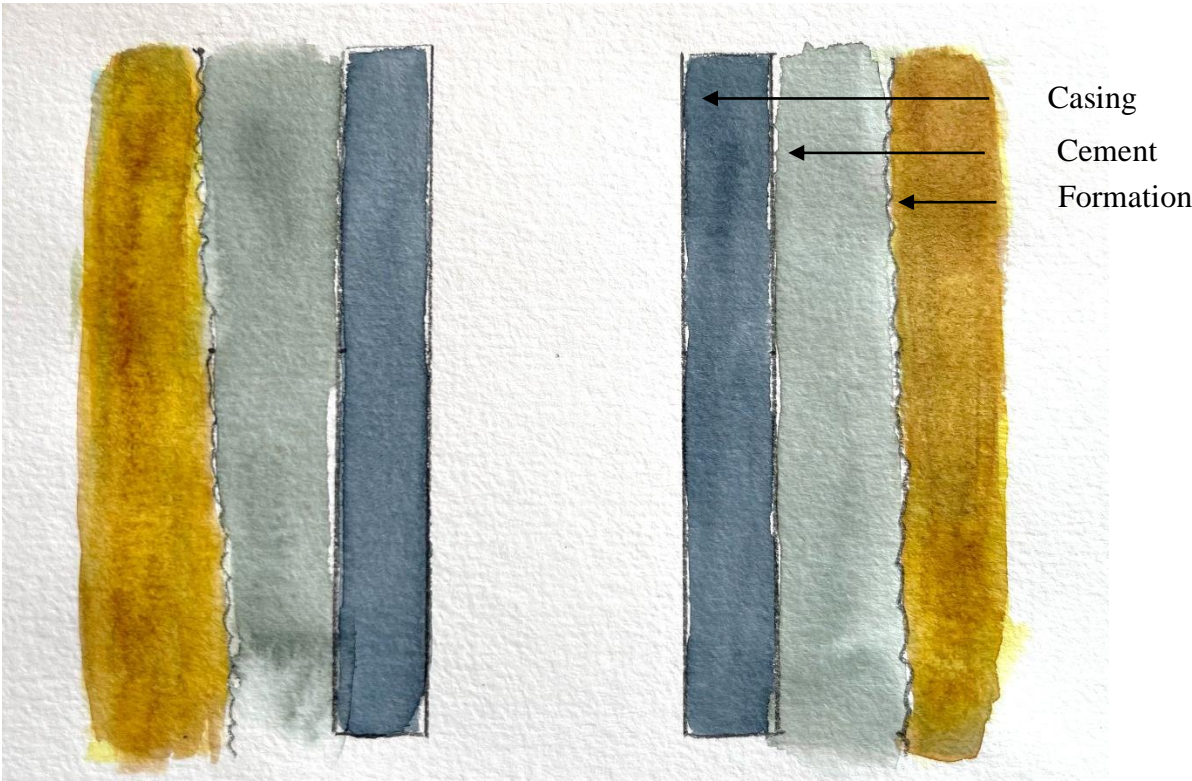


Figure 3 Cross-section of a cemented wellbore

If the casing is properly cemented to both the formation and the casing steel, it will provide isolation between layers in the formation and the steel pipe. The casing and casing cement is designed to maintain the well integrity throughout the life of the wellbore (Crumpton, 2018).

2.1.2 Completion

The second phase of a petroleum well and it is the last part of the construction of the well, and it called completion. Completion is defined as the equipment, tubing and materials used to isolate the interface between the reservoir and the surface production equipment. The goal of the completion is to create a design, which makes the production of the reservoir fluids as safely and efficiently as possible. This is achieved by using a design derived by combination of various disciplines including physics, mathematics, geology, chemistry, engineering, experience, regulations and material science (Bellarby, 2009).

The well can be completed either as a producer or as an injection well. The injector well will be used to stimulate the reservoir to enhance the production of hydrocarbons by injecting gas, sea water or stimulating chemicals. While the producer well will be the pathway of the hydrocarbon to the surface. A completion operation can be divided into three phases, reservoir completion, middle completion and upper completion. Where there are different approaches on how to finish the reservoir completion. From leaving it as an open hole or by cementing it and installing a screen to avoid the production of sand (Crumpton, 2018).

2.1.3 Production

During the production phase of a petroleum wellbore hydrocarbons are flowing from the reservoir though a production tubing to the surface. The goal of this phase is to maximize the production of oil and gas while maintaining well integrity and the well barriers. To ensure a safe production. The produced hydrocarbon is transported to a process facility.

2.1.4 Plug and Abandonment

Permanent plug and abandonment (P&A) where OPC are a significant contributor are the final phase of the lifecycle of a petroleum well. This operation is a cost only operation, therefore there is a need for a cost-efficient operation. This efficiency cannot compromise the scope of the operation and the eternality perspective of the well barriers and the wellbore well integrity (Khalifeh, Saasen, 2020, page 7).

Permanent abandonment can be divided into four phases (Khalifeh, Saasen, 2020, pages 26-27).

0. *Information gathering and planning phase.* Where the wellbore's pressure and the condition of the wellbore is logged.
1. *The reservoir abandonment,* where two barrier envelopes are used to restore the caprock.
2. *The intermediate abandonment.* In phase two casing is retrieved, barrier envelopes are placed to isolate intermediate formations which are either hydrocarbon or water-bearing formations.
3. *Cut and removal of wellhead.* This is the phase where an environmental barrier is placed under the wellhead before the well head and the conductor is removed.

The reason to do P&A is to avoid hazardous fluids, chemical components and pressure migrating from the subsurface through human made pathways to the surface. As these fluids and the pressure can do large environmental damage and affect marine food reserves and fresh ground water.

2.1.5 Challenges when doing P&A

Every petroleum wellbore is a unique construction and will have different challenges associated with it. Challenges such as the following (Khalifeh, Saasen, 2020, page 3):

- High temperature and high pressure
- Unconsolidated formations
- Corroded pipe, tubing or downhole equipment
- Sustained casing pressure, from gas or fluid migration from tubing to the annular space
- Uncertain ultimate reservoir pressure, after restoring the cap rock.

The cement used to secure and isolate the casing steel and the wellbore, needs to have a sufficient strength to withstand the overburden stress from the overlying layers of sediment.

2.1.6 Well Integrity NORSOK-D10

Well integrity can be defined as the application of operational, technical and organizational solutions to reduce risk of uncontrolled release of formation fluids, well fluids and downhole pressure throughout the life cycle of the well (NORSOK D-10, 2021).

2.1.7 Well barrier elements

A well barrier element is a material, when combined with another or more make up a well barrier envelope. NORSOK-D10 regulation defines a well barrier element as an object that alone cannot prevent flow from one side to the other side of itself. The barrier elements can be steel, steel-alloys, cements or elastomers. Newer barrier materials which can replace ordinary cements is geopolymer cement or for shallow barriers bismuth plugs (Khalifeh, Saasen, 2020, page 16)

2.1.8 Well barrier

A well barrier, is an envelope of one or several dependent barrier elements preventing fluid or gases from flowing unintentionally from the formation into another formation or to surface (NORSOK D-10, 2021). Casing steel and cement like illustrated in Figure 3, is an example on a well barrier. All barriers should therefore be equipped with sufficient well barrier elements to prevent leakage from permeable formations and reservoirs (Khalifeh, Saasen, 2020, page). As a single failure will lead to leaks and loss of well integrity. This loss can lead to unacceptable consequences for the environment and working crew. Therefore, the usage of two independent well barrier envelopes is used to ensure if one fails there is a secondary barrier. It is necessary for the two barrier envelopes to have different materials used for the barrier elements. If not, it is a question of time before the secondary barrier also fails. The petroleum engineer archive this by designing two barrier envelope systems, where different barrier elements which makes up a single barrier envelope, which is illustrated in Figure 4.

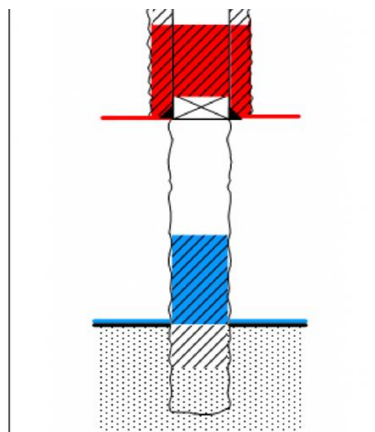


Figure 4 Example from NORSOK on a two-barrier envelope of permanent abandonment (NORSOK D-10, 2021, page 101)

2.2 Portland cement

Table 2 Standards for OPC cement from API 10 A (Khalifeh, Saasen, 2020, page 101)

Class	Curing Time [Hours]	Curing Temperature [°C]	Curing Pressure [MPa]	Typical Compressive strength [MPa]
API Class G	24	95	5.51	17.51
API Class H	24	95	5.51	14.54
API Class G	24	110	11.03	20.09
API Class H	24	110	11.03	17.40

Table 2 above presents the API standard requirements for the typical compressive strength of OPC class G and H under atmospheric conditions, with two different temperatures 95°C and 110°C.

There are several ceramics materials which can be classified as inorganic cements. The ceramics produced in extremely large quantities are Portland cement, Plaster of Paris or lime. Cements are mixed with water to form a paste, which will subsequently set and harden. As it is a paste (thick fluid) it can set to any shape, as long as it is a liquid (Callister, Rethwisch, 2011, pages 481-482).

Cements like Ordinary Portland cements, OPC, also contain materials which makes it possible for the cement to create both a chemical and hydraulic bonding (Callister, Rethwisch, 2011, pages 481-482). This bonding is crucial to ensure that the cement bounds to the formation and casing steel and this bound remains intact to preserve well integrity The term "ordinary" in OPC refers to its manufacturing process, where it is produced in a rotary kiln from a molten matrix to form clinker. OPC serves as a common choice for various well cementing operations. The strength of OPC is derived from the hydration reactions that occur when water is added to the dry phase (Schlumberger, Nelson, 2006, page 23).

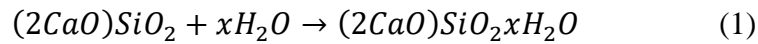
The reason Portland cement is a popular construction material, is that is able to set both in air and submerged in water. It has predictable, uniform and relative fast setting time and development of strengths, and low permeability and low solubility in water. These properties

are essential to be able to achieve and maintain zonal isolation in the wellbore (Schlumberger, Nelson, 2006, page 23).

PCC- Portland cement concrete can include fine aggregates such as sands or coarse aggregates like gravel. The aggregate acts like a filler material to reduce the overall cost of the concrete. As sands and gravel being cheaper than Portland cement. (Callister, Rethwisch, 2011, pages 543-545). The main difference between concrete and cement, is cement acts like a binder whereas concrete is the resulting composite material of the addition of cement to a stone-based aggregate (Davidovits, 2013).

Cements contain chemical binder agents, which binds particulate aggregates into a cohesive structured material. Portland Cement (PC) is the cement which is the most consumed cement in the world. This cement is produced by grinding and intimately mixing clay and lime bearing minerals in correct proportions. The mineral mixture is then heated to about 1400°C in a rotary kiln to produce clinker. This process is called calcination. The clinker is then grounded to a very fine powder to which a small amount of the mineral gypsum ($\text{CaSO}_4 \cdot 2\text{H}_2\text{O}$) is added as a retarder. An additive to slow down the setting process of the cement. (Callister, Rethwisch, 2011, pages 543-545). Clinker can be divided into two types, calcareous materials and argillaceous (aluminous silica iron). The properties of Portland cement are determined by mineralogical composition of the clinker. When selecting the raw materials and kiln fuel (for heating), determines the purities of the clinker. If there is manganese content of 0.5 weight % of the clinker, will lead to a formation of large alite crystals, which can act as a retarder for the strength development of the cement (Schlumberger, Nelson, 2006, page 25). The strength and other material properties of OPC depends on the composition of the dry mixture, setting time and the added amount of water, (Callister, Rethwisch, 2011, pages 543-545).

During the hardening and setting of OPC, relative complicated hydration reactions will react among the various cement binders (Calcium silicates) and the added water. The calcium silicates hydrates will create complex gels or crystalline substances during the hydration. These molecule structures are the backbone to cementitious materials, where one of them is Portland cement. With the addition of inert particles like a rock substance, the cement becomes a part of a concrete system (Callister, Rethwisch, 2011, pages 543-545)



Where the x depends on the amount of water added to the dry phase of the Portland cement.

2.2.1 Challenges with Ordinary Portland cement

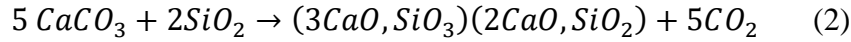
During hardening and setting, the cement slurry will undergo a net volume diminution. This shrinkage is due to during and after the curing the solid cement is denser than the slurry. To counter act this an additive agent can be used. Addition of calcium chloride will decrease the volume of the cement by between 10-50% (Schlumberger, Nelson, 2006, page 53). Another problem with OPC, is the effect of temperature on the setting of the cement slurry. At elevated temperatures, the curing of the cement will be accelerated. The resulting cement will have a weaker ultimate strength, than a cement which is cured 40°C (Schlumberger, Nelson, 2006, page 37).

The OPC dry phase needs to be isolated from any moisture, even water vapor from the atmosphere can react with the dry phase of the cement. The resulting product will be a partial hydration of free calcium oxide (CaO) and tricalcium aluminate ($3CaO \cdot Al_2O_3$). This will cause an imbalance with the aluminates, silicates and alkali phases of the dry phase. In hot climates, the gypsum in Portland cement dry phase can be dehydrated. The water from the gypsum can react with the other dry components and cause imbalance and leading to false-set phenomenon. If a storage silo reaches an internal temperature of 93°C, it will lead to dehydration of the gypsum and false setting of the dry phase (Schlumberger, Nelson, 2006, page 38).

Subsurface formations and completion brines (salt-based solutions) commonly contain sulphates like magnesium and sodium sulphates. These sulphates can react with certain cement hydrates products. The resulting product will cause swelling, an increase in porosity, decrease in ultimate strength and an increase of permeability for the material (Schlumberger, Nelson, 2006, page 40).

2.2.2 CO₂ emission during manufacturing

Portland concretes is one of the most used construction materials. Production of Portland cement leads to large CO₂ emissions. These emissions are due to the refining process of grounded limestone and clay, this process is called calcination and the produced product is called clinker.



Total emissions from production of 1-ton ordinary Portland cement will emit 0.95 ton of carbon dioxide. Geopolymer cements do not require calcium carbonate, therefore there is a reduction of emissions in a range of 40% to 90% of CO₂ (Davidovits, 2013).

-Addition of impact of Drilling fluid contamination and other problems

2.3 Geopolymer

Geopolymer cement is a binding system that can harden at room temperature. If the geopolymer compound needs heat to cure, it is defined as a geopolymer binder. Geopolymers can be divided into four main categories:

- Slag based geopolymer cement.
- Rock based geopolymer cement.
- Fly ash based geopolymers, which is divided into two types.
 - o Type 1: alkali-activated fly ash geopolymers.
 - o Type 2: slag/ fly ash based geopolymers.
- Ferro-silicate based geopolymers.

Slag-based geopolymers was the first geopolymer cement developed in the 1980s. Where Potassium-, Natrium- or Calcium-polysilicate are different slag-based geopolymer cements.

Metakaolin (MK-750), which is an anhydrous calcined form of the clay mineral kaolinite, is commonly used in the production of slag-based geopolymer cement when combined with blast furnace slag and alkali silicate. However, an alternative approach involves substituting MK-750 with carefully selected volcanic tuffs. This substitution not only reduces CO₂ emissions but also enhances the strength of the slag-based geopolymer cement (Davidovits, 2013).

Fly ash, a biproduct of combustion of coal, is commonly used as the base for Type 1 fly ash-based geopolymers or added to OPC clinker during manufacturing (Davidovits, 2013 Hemalatha, 2022). Unlike traditional cement, these geopolymers require heat for the curing process, typically at temperatures ranging from 60°C to 80°C. These geopolymer cements are the base for a fly ash-based concrete. The two bases used as the alkali activators are potassium hydroxide and sodium hydroxide, with a Si:Al ratio of 1 to 2. The zeolites which are used in type 1 fly ash based geopolymer are Chabazite $(\text{N}_2, \text{K}_2 \text{ or } \text{Ca})_2[\text{Al}_2\text{Si}_4\text{O}_{12}]_2 \cdot 12\text{H}_2\text{O}$ and Sodalite $\text{Na}_8(\text{Al}_6\text{Si}_6\text{O}_{24})\text{Cl}_2$ (Davidovits 2013).

Type 2 slag, fly ash based geopolymer cement is a more user-friendly, due to not being activated by strong alkali bases. Cures at room temperature, and the cement hardening silicate solution is mixed with blast furnace slag and/or fly ash. With a silicon aluminium ratio of Si:Al = 2. Where the poly silicate-siloxo is bounded to Calcium or Potassium

Ferro-silicate based geopolymers, are geopolymers which contains iron. With the chemical structure $(\text{K}, \text{Ca}) - (\text{Fe}-\text{O}-\text{Si}-\text{O}-\text{Al}-\text{O}) - (\text{K}, \text{Ca})$ and have similar properties as rock based geopolymers (Davidovits, 2013).

2.3.1 Possible replacement for OPC

Geopolymer has the potential to be a real alternative to the conventional used cementation material for both onshore and offshore well applications and for other construction industries. One of the main advantages of geopolymers to OPC is the usage of minimal processed natural material and or the usage of by-products from industrial combustion processes (Davidovits, 2013). This makes the carbon footprint of the production of geopolymers less than the production of cement.

Addition the effect of drilling fluid contamination on Geopolymer will be added

Geopolymers have resistance to many durability issues that plague conventional concretes used in wellbore activities. One of these differences is the geopolymer gains most of its strengths during the first 24h of curing. Another difference is that geopolymers can form chemical bonds with all kinds of rock-based aggregates (Davidovits, 2013).

A study of the stress-strain behaviour of an ASTM class 'F' fly ash geopolymer cured in 15% saline water in 28 days by Giasuddin et al. The resulting data from a uniaxial compressive test showed that the geopolymer was stronger than an oil well cement class G, (66 ± 1.45 MPa) and (30.5 ± 1.08 MPa) this was a difference of 35.5 MPa (Giasuddin et al. 2013). Meaning the class G cement is more vulnerable to decrease in compressive strength when placed in 15% saline water. In fact, the study found that the 'F' class geopolymer increased its compressive strength from being cured in saline water compared to fresh water, increase from (47.5 ± 1.05 MPa) to (66 ± 1.45 MPa) (Giasuddin et al. 2013). Therefore, 'F' class geopolymers can be a better alternative than class G cement for offshore cementing, as the effect salt water does not decrease the compressive strength of 'F' class geopolymers.

The effect of synthetic-based drilling mud (SBM) contamination on Portland cement can lead to poor cementation and thereby risk the cement integrity. Therefore, an alternative to OPC needs to have a compatibility with SBMs. A study by Liu et al. in 2016 found that a geopolymer cement lost 30% of its strengths compared neat Portland class H cement which lost up 70% of its strength (Liu et al. 2016). The result indicates geopolymers material strengths are less effected by contamination of SBMs, compared to neat Portland class H cement.

2.3.2 Rock-based geopolymer manufacturing:

The production process of rock-based geopolymers begins with the heat treatment of kaolin clay, aimed at removing the water content within the clay mineral. Afterwards to produce metakaolin, the anhydrous kaolin is heated to 700°C together with calcium. Additionally, the other components of the dry phase, namely fly ash and blast furnace slag, are obtained as by-products from coal power plants and steel-making facilities, respectively. The alkali base required for the geopolymerization process is produced through the method of electrolysis of brine (McLeellan et al., 2011, Davidovits, 2013).

In comparison the energy needed to produce OPC is around 4700 MJ/ton. While rock based geopolymers require 41% of the OPC energy needs, around 1927 MJ/ton. In the least favourable is case, 57% of the OPC energy around 2679 MJ/ton, is needed to produce

geopolymers. This energy reduction reduces the CO₂ emissions reduction to 70-80% of the CO₂ emissions of OPC (Davidovits, 2013).

2.4 Rock mechanics

This chapter is based on the two books “*Petroleum Related Rock Mechanics 2nd edition*” (Fjær et al. 2008) and “*Mechanics of Materials*” (Hibbeler, 2013).

Elasticity is a materials, object or body’s ability to resist and recover from deformations formed due to applied force or stress on the body. The elasticity of a material is usually not enough to predict a materials behaviour. A materials elasticity is expressed through its Young’s modulus, the ratio of stress to strain (Fjær et al. 2008, page 1). The value of a materials the Young’s modulus (E) relays the materials behaviour is either ductile or brittle when exposed to stress. A further explication of Young’s modulus is relayed later in chapter 2.4.3 of this thesis. The reaction of the material to applied stress can be illustrated in a stress-strain diagram, see Figure 5 below for the reaction of one of the samples tested in a triaxial stress cell. The triaxial stress test is used to test and gather data on a materials behaviour and is describe in greater detail in chapter 3.2 in this thesis. This raw data collected from the triaxial test used to calculate the axial strain, which was plotted against a calculated axial stress (y-axis). Further explanation on how Figure 5 was plotted is described in chapter 3.3 Data analysing methods of this thesis.

In a stress-strain diagram, the stress application will usually produce a linear strain response in the beginning, and the deformation is called elastic deformation. When staying inside the elastic area the material is able to return to close its original form without being permanently deformed and the material properties do not degenerate. Once the material leaves the elastic deformation and enters the plastic deformation the materials properties and shape will be permanently altered (Fjær et al. 2008, Hibbeler, 2013).

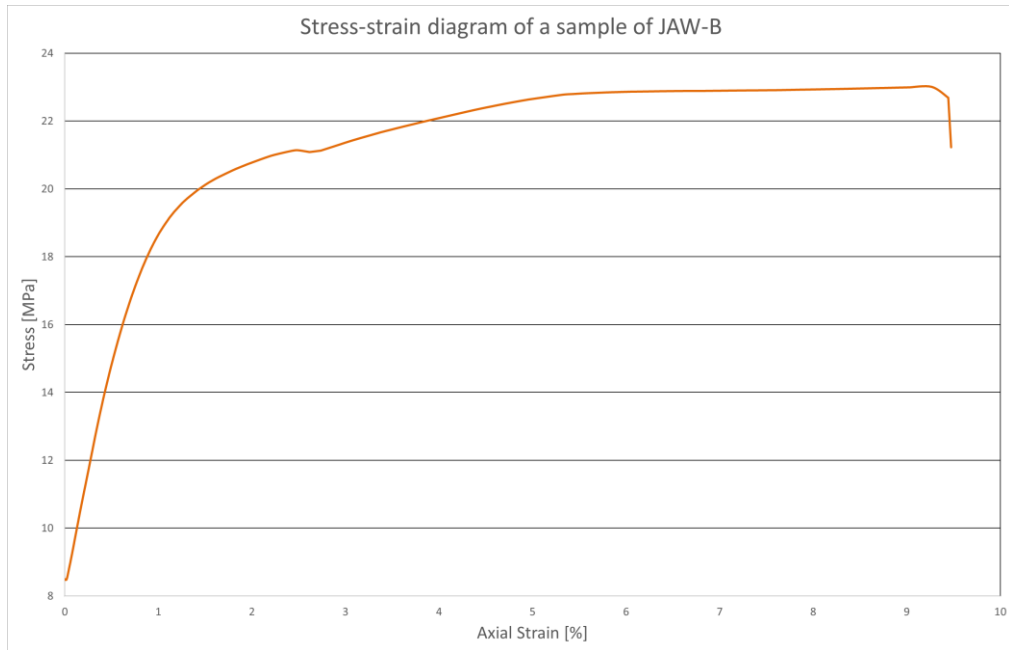


Figure 5 Stress-strain diagram of sample 10 of JAW-B geopolymer

2.4.1 Stress

To determine the material strengths of the geopolymer JAW-B, a piston will apply a force on the cylindrical sample in the vertical direction and a confining pressure will also be applied to the sample. When a force (F) is acting on a cross-sectional area (A_{cross}), then the stress (σ) across the cross-section is defined in equation 3 as

$$\sigma_{stress} = \frac{F}{A_{cross}} \quad (3)$$

Stress as the International System of Unit of Pascal (Pa) and for Oil Field units stress is assigned pound per square inch (psi) (Fjær et al. 2008 page 1). These units are also commonly used for pressure.

In rock mechanics if the sign in front of stress is negative it denotes that the material or body is in tension, and if it is positive the material is in compression. The notation between compression (positive) and tension (negative) is due to historically in rock mechanics mostly studied the compressive stresses in formation, caused by the over layering layers.

Figure 6 depicts how tension and compression forces changes the length of a body. Where tension is when an object is being pulled in one or multiple directions. While compression is when an object is being pressed in one or multiple directions.

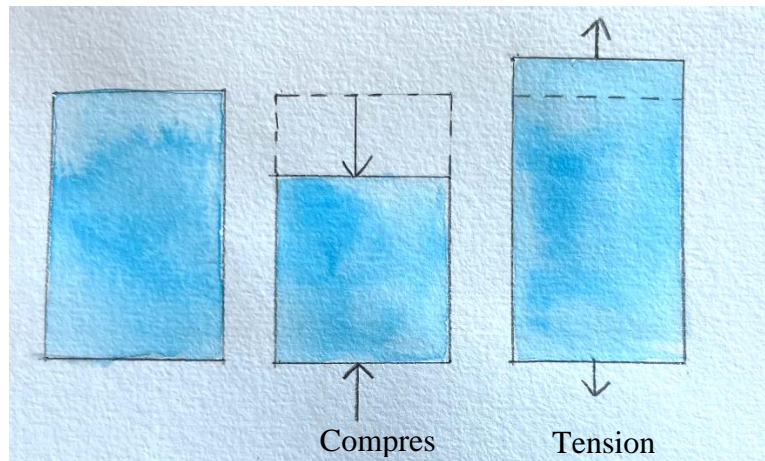


Figure 6 Tension and compression forces acting on a body

A non-homogenous body is a body which is not of a singular geometric shape, for example circles, triangles or squares, cylinders, and cubes. For a non-homogenous body, like the geopolymer samples a localized stress point can be expressed through the general stress formula (Hibbeler, 2013 page 24). This is achieved by simplifying the non-homogenous body into set number of subsection of cross-sectional areas ΔA_n , see Figure 7 below. Where the impact of the force ΔF_i , the stress at a point in a subsection i. Equation 4 defines stress at a subsection i as the impact force acting on the subsection cross-sectional area ΔA_i .

$$\sigma_i = \frac{\Delta F_i}{\Delta A_i} \quad (4)$$

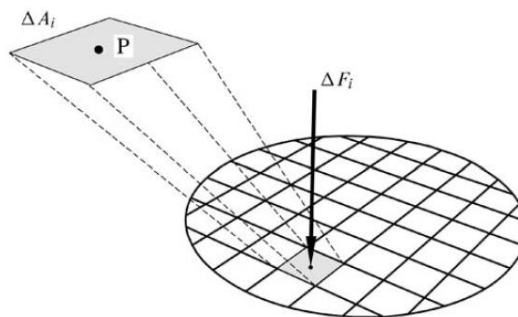


Figure 7 Local stress acting on a selected cross-sectional area ΔA_i (Fjær et al.2008, page 3)

So, when the stress state at a specific point, the local stress is therefore expressed. The force orientation on to the cross-sectional area impacts the type of stress that is experienced

by the body. A force acting normal (90°) on the cross-section it, as illustrated in Figure 8 below. This force will produce a normal stress and a shear stress on the body. The shear stress will act in tangent to the area ΔA (Fjær et al. 2008, Hibbeler, 2013). Shear stress is usually denoted by τ while normal stress is denoted σ . Shear stress is defined in equation 6 and the normal stress is defined in equation 5.

$$\sigma_{normal} = \frac{F_{normal}}{A_{cross}} \quad (5)$$

$$\tau_{shear} = \frac{F_{parallel}}{A_{cross}} \quad (6)$$

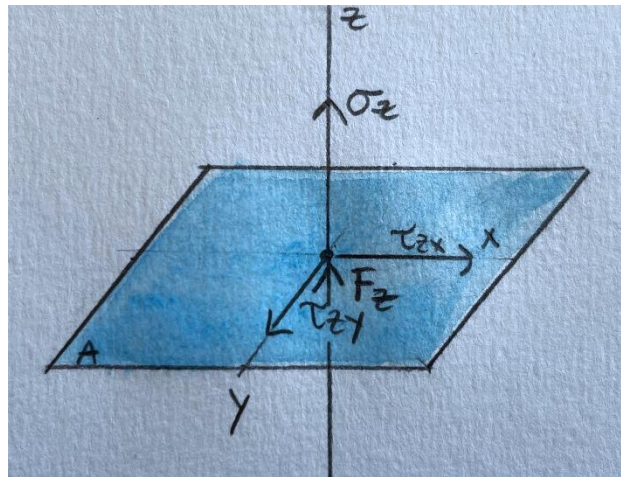


Figure 8 Illustration of a force acting on a surface yielding normal stress and shear stress

In three dimensions there is nine stress components, which is presented in the 3x3 matrix below matrix 1. This matrix is also known as a stress tensor and gives a complete description of the stress state at a point (P) on a cross-sectional area (Fjær et al. 2008, page 4).

$$\begin{pmatrix} \sigma_x & \tau_{xy} & \tau_{zx} \\ \tau_{xy} & \sigma_y & \tau_{zy} \\ \tau_{xz} & \tau_{zy} & \sigma_z \end{pmatrix} \quad (\text{matrix 1})$$

2.4.2 Strain

The concept of strain was developed to describe the deformation of a body caused by an external or internal force acting on the body. Strain is denoted by the Greek letter (ϵ) and characterizes the changes in the geometry of the body (Hibbeler, 2013, pages 68-67). Where positive strain is defined as compression of the body and negative will elongate the body.

Strain can be categorized into two main types, normal strain and shear strain (Hibbeler, 2013, pages 68-67). The difference between the two is illustrated in the Figure 9 below. Shear strain pertains to the deformation of a body in which the displacement acts perpendicular to the applied force or stress. Other factors like pressure and temperature can also change the geometry on the body. Whereas normal strain is associated with change in length (L) of the body and can be expressed in the following equation 7.

$$\epsilon_n = \frac{L_0 - L_1}{L_0} = \frac{\Delta L}{L_0} \quad (7)$$

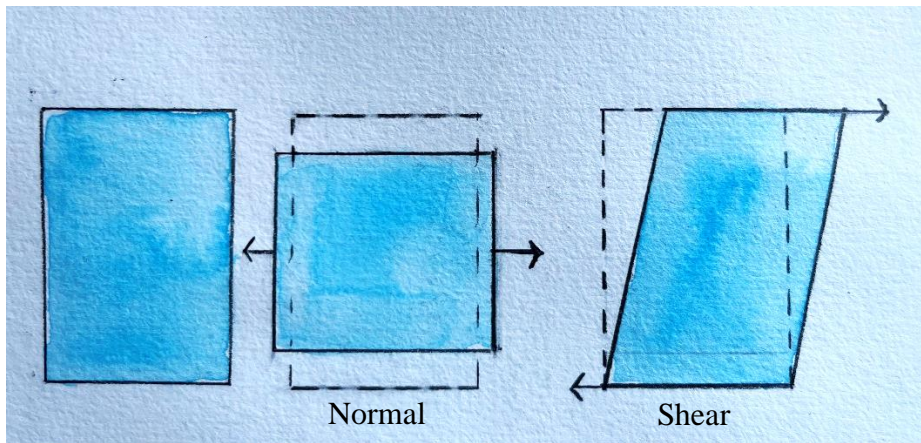


Figure 9 Normal strain (Middle) and Shear strain (Right) acting on a body

Normal strain (ϵ_n) is a dimensionless quantity as it represents the ratio of two lengths. For a cylindrical wellbore there are three main strains and stresses acting on the wellbore wall. These are the axial, radial and tangential stress and strains. Axial strain can be considered as a specific type of normal strain derived from the overburden stress from layers of rock. Hence ϵ_n is equal to ϵ_{axial} . Radial strain is defined as the deformation occurring in the radial direction from the radial stress, expressed as the change in the circumference (C) relative to the original circumference (Fjær et al. 2008, pages 135-37). The radial strain is defined in equation 8. This change is quantified by the following equation. The last strain is the hoop also known as the tangential strain ϵ_θ , which act tangential to the wall.

$$\epsilon_{radial} = \frac{C_0 - C_1}{C_0} = \frac{\Delta C}{C_0} \quad (8)$$

Volumetric strain is the change in the volume (V) resulting from the deformation of the body (Fjær et al. 2008, page 17). It can also be calculated using the equation for normal strain, expressed in equation 9.

$$\varepsilon_{Volumetric} = \frac{V_0 - V_1}{V_0} = \frac{\Delta V}{V_0} \quad (9)$$

For non-homogenous materials the volumetric strain can also be derived from the axial and radial strain expressed by following equation 10. Where the assumption is that the radial and hoop strain is equal in a system with a set confining pressure.

$$\varepsilon_{Volumetric} = \varepsilon_{axial} + 2\varepsilon_{radial} \quad (10)$$

In the case of isotropic or homogenous material, where the material properties remain constant in all directions. The volumetric strain can be expressed as three times the axial strain, as in equation 11.

$$\varepsilon_{Volumetric\ isotropic} = 3\varepsilon_{axial} \quad (11)$$

2.4.3 Hooke's law and Young's modulus

In the elastic region of most materials, there exists a linear relationship between stress and strain. This is illustrated in the Figure 102 below. As the applied stress increase, the resulting strain will also increase proportionally (Hibbeler, 2013, page 92-93)

. This fundamental relationship, known commonly as Hooke's law, was discovered by Robert Hooke in 1676 through the study of spring behaviour. Hooke's law can be expressed as the equation 10.

$$\sigma = E\varepsilon \quad (12)$$

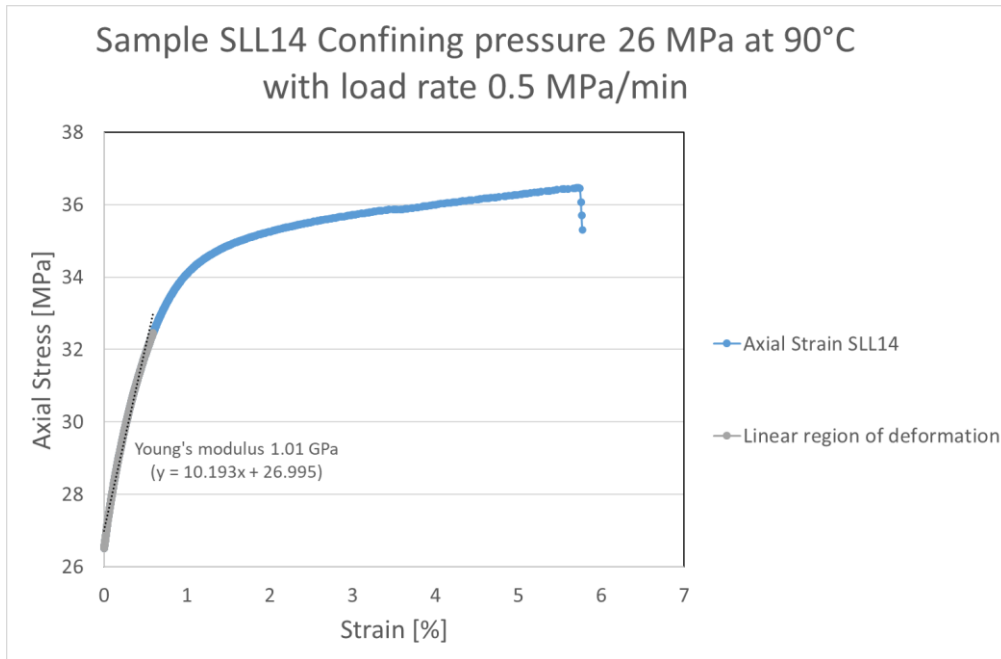


Figure 10 Sample SLL14 Illustrating Young's modulus in the elastic region of deformation

In the equation 10 (E) denotes Young's modulus, (σ) represents stress and (ϵ) denotes strain. Young's modulus the modulus of a materials elasticity which represents the slope of the linear relationship between stress and strain. Since strain is a dimensionless property, Young's modulus will have the unit of the stress applied to the material. Modulus of elasticity serves as an indicator of a materials stiffness, with higher values corresponding to a stiffer material. The stiffer the material is the less ductile the material is. The difference between a brittle and ductile material is illustrated in the Figure 11 below.

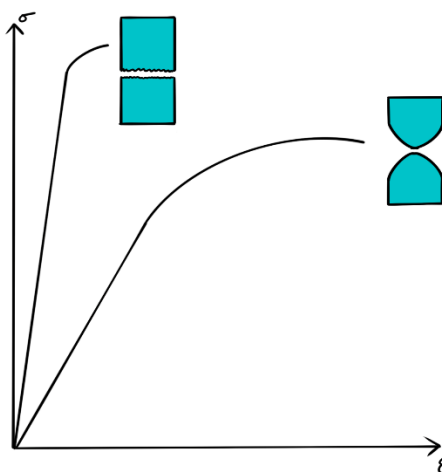


Figure 11 Illustration of difference of behaviour between a brittle(left) and a ductile material(right)

The stresses acting on a cylindrical-shaped samples can be described by three stresses components: radial stress (r), hoop stress (θ)- and axial stress (z). In the case of porous samples, there exists a ratio between bulk modulus (K) at a constant confining pressure and at constant pore pressure (Fjær et al. 2008, page 33). This ratio is known as Biot's coefficient (α). By Hooke's law with Biot's coefficient equal to 1, these stresses can be expressed as in equations 12 to 14.

Another indicator of a materials stiffens is the materials bulk modulus (Hibbeler, 2013, pages 514-515), as the surrounding pressure increases. The geopolymer JAW-B samples will be tested at confining pressures of 8, 17.2 and 26 MPa. For materials which intended to be used in high pressure environments it is important to know how the material will react to the increase in pressure. Bulk modulus (K) is a measure of the stiffness of a volume of a material. It is an important elastic modulus, which is defined as the ratio of hydrostatic stress (σ_{HS}) relative to the volumetric strain. This relationship is expressed though the equation 13.

$$K = \frac{\sigma_{HS}}{\varepsilon_{vol}} \quad (13)$$

Hooke's law in the wellbore can be expressed in the following three equations 14, 15 and 16.

$$E \varepsilon_r = \sigma_r' - \nu(\sigma_\theta' + \sigma_z') \quad (14)$$

$$E \varepsilon_\theta = \sigma_\theta' - \nu(\sigma_r' + \sigma_z') \quad (15)$$

$$E \varepsilon_z = \sigma_z' - \nu(\sigma_\theta' + \sigma_r') \quad (16)$$

If the remaining three shear stresses equations in Hooke's law equals to zero. Then the hoop, radial and axial stress will be equal to the principal stress directions. This is due to the symmetry of the circular cylinder together with the triaxial set up. Where the effective stress σ' equations are valid for both non-porous and porous materials.

2.4.4 Poisson's ratio

Poisson's ratio is a dimensionless value which expresses a deformable body reaction to an axial tensile force. Poisson's ratio is the ratio between the change in length and the change in radius as a material is subjected to a force or stress acting on the body. This ratio is stated mathematically in equation (17)

$$\nu = -\frac{\Delta\varepsilon_{radial}}{\Delta\varepsilon_{length}} \quad (17)$$

The negative denotation is included due to lateral expansion causes longitudinal contraction, and vice versa. Since Poisson's ratio is based on changes in strain, it is also a dimensionless property of a material. The values of Poisson's ratio ranges from 0 to 0.5, where closer to 0.5 the more elastic the material is (Hibbeler, 2013, pages 104-105). Natural rubber has a Poisson's ratio close to 0.5 (Rosato, Rosato 2003).

2.4.5 Compressive strength

The compressive strength a material strength which indicates the ultimate strength of the sample right before it starts to fail. The uniaxial compressive strength is defined as the peak stress of a material at a stress-strain diagram, as illustrated in the principal sketch in Figure 12 (Fjær et al., 2008 page 56).

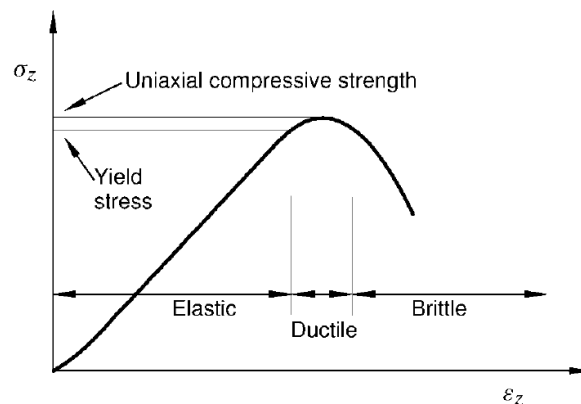


Figure 12 Principal sketch of stress-strain diagram for a uniaxial compression test, illustrating the material behaviour from elastic to brittle. (Fjær et al., 2008 page 56)

2.5 Triaxial Cell

The following chapter is based on the book “*Petroleum Related Rock Mechanics 2nd edition*” (Fjær et al. 2008, pages 251-269)

When gathering data about a materials properties and strengths, laboratory testing is required to determine the materials behaviour. In the field the formation rocks properties can be estimated or determined from logs, core sample gatherings, seismic data, Leak-off or Formation fitness tests (Pressure testing of the formation). These logs and measurements can give an estimate against the depth but is not a direct measurement of a rock formation.

Therefore, in the laboratory setting the goal is to simulate the downhole conditions. Such as the temperature and pressure of the downhole. In rock mechanics, the core analysis is designed after the purpose of the investigation, which parameters of the rock that is of interest. For a geopolymer sample, a possible well barrier element to be used in the wellbore, needs to be tested to determine that the material will be stable at subsurface conditions with high pressure and high temperatures. This testing is done to ensure that the geopolymer does not fail and therefore risk the stability of the wellbore and thereby the well integrity of the petroleum well.

2.5.1 Triaxial cells test sample requirements

The test core sample should ideally not contain any fractures or chips. The size of the core should be of the lengths 1.0'' to 2.5'' in diameter and 4'' to 5'' in length.

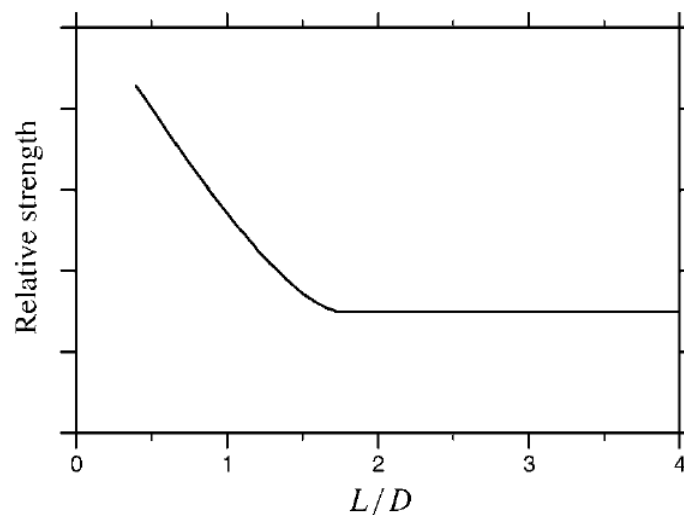


Figure 13 Effect of length and diameter ratio on uniaxial compressive strength of a rock sample [Fjær,2008]

The international Society of Rock Mechanics, ISRM, in 1981 created standards for samples used in rock mechanical test. The standards require the samples to be circular cylinders with a length to diameter ratio between 2 and 3 (Fjær et al. 2008, pages 256-257). The ratio is due to accommodate for a sufficient length for a shear plane to penetrate through the side walls of the cylinder. Therefore, if the sample is too short, the shear plane will propagate through the end faces, and thereby provide additional support. Figure 13 illustrates the expected effect with the variation of the length to diameter ratio on the strength of the test

sample. This chosen criterion, ensures that the length to diameter ratio yields the actual uniaxial compressive strength, rather than the insensitive minor deviations in length to diameter ratio. The diameter should also need to be 10 times larger than the grain size of the test material or rock sample (Fjær et al. 2008, pages 257).

2.5.2 Triaxial laboratory equipment

A triaxial cell test consists of the following a triaxial cell, a confining pressure system, pore pressure system, piston pressure system and a computer for controlling the different systems, and data gathering and processing (Fjær et al. 2008, pages 257-258). The pressure systems consist of pumps, valves, reservoirs and waste gathering, as illustrated in the Figure 14. Which was the triaxial cell setup which the geopolymer was tested in.

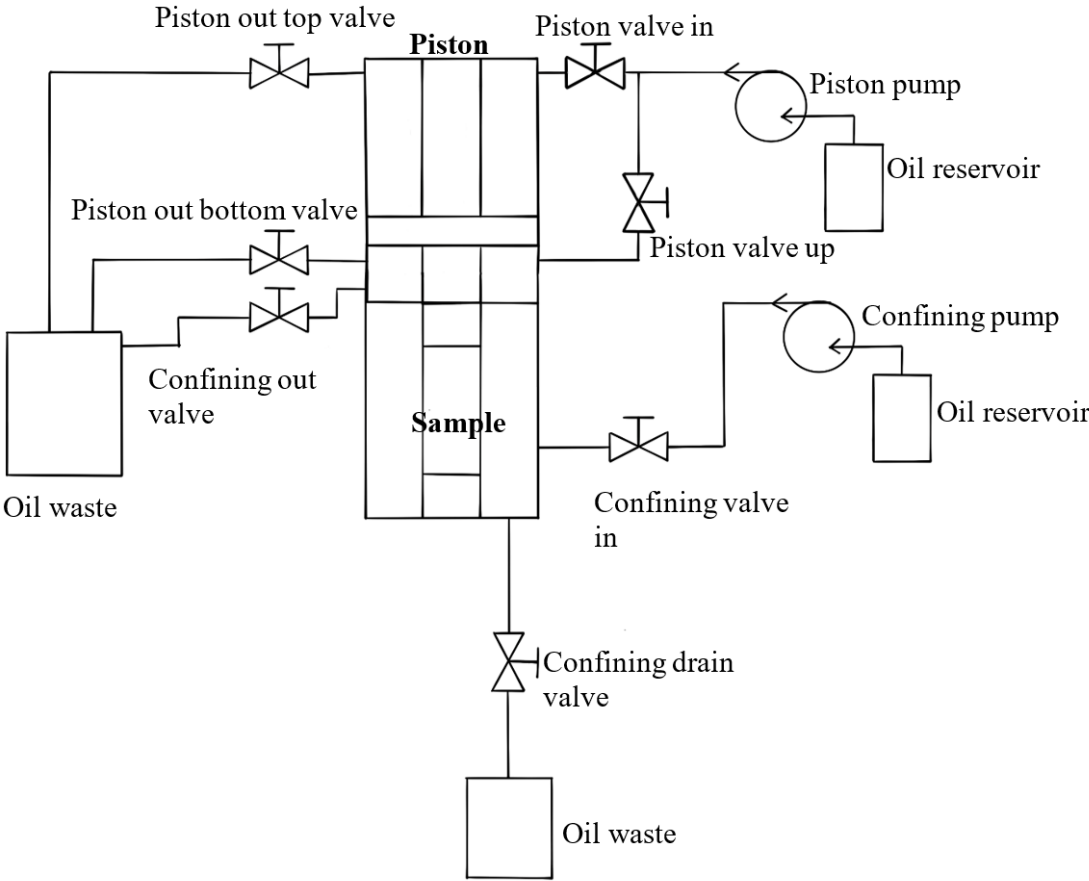


Figure 14 P&ID schematic of a triaxial cell without the water injection pump

The piston, drainage disc and pedestal for the cell, should be the same size as the test sample to ensure that the force applied by the piston is distributed equally on the surface of

the test sample. Both the piston, pedestal and water spreader also must be of a material which have a greater hardness than the test sample. Material like steel or steel alloy.

At the top of the triaxial cell axial piston, there is an opening allowing for a linear variable differential transformer (LVDT) axial measuring tool to be fitted (Fjær et al. 2008, page 261). Allowing for measuring axial movement during the triaxial test. All the measuring tools needs to be calibrated before the usage.

The sample will be covered by a thin sleeve, which is soft enough to avoid giving any significant support to the sample during the test core. The sleeve can be of heat activated plastics, which has a thickness of a few millimetres. This allows for a more accurate radial strain readings by a circumferential extensometer and hinders the confining oil from filling the sample (Fjær et al. 2008, page 260).

For the triaxial stress cell used to test the JAW-B geopolymers samples the axial stress applied on the test sample, was derived using equation 18. The recorded confining pressure and piston pressure and internal friction during the triaxial stress test.

$$\sigma_{axial} = P_{Confining} + f_{internal}(P_{piston\ pressure\ factor}) * (-0.00994908 * P_{Confining} + 0.195673) \quad (18)$$

The strains of the sample were determined by analysing the recorded change in axial movement (axial strain), change in circumference (radial strain) and the change in both axial and circumference (volumetric strain). This is described in further detail in chapter 3.3 of this thesis.

During a triaxial drained test, the collected data get presented in a stress-strain curves. These curves are split in two phases called the hydrostatic phase, the increase of confining pressure, and the deviatoric phase, the load phase where the piston pressure is increased. In the hydrostatic phase the stresses in the horizontal direction is equal and the materials bulk modulus can be determined by the following equation with the change in volumetric strain against the effective axial stress.

2.5.3 Purpose of hydrostatic test (hydrostatic phase)

The hydrostatic measurements are mainly performed to determine the bulk modulus of a sample. Which can be of the following materials rocks, ceramics like ordinary Portland cements, geopolymers, concrete, etc (Fjær et al. 2008, page 268).

This is the first phase of the triaxial test, where the test sample usually does not fail. Unless the confining pressure is too high for the material to withstand. For a drained closed system, the pore pressure does not change during the test. Therefore, the slope of the volumetric strain-stress curve will be equal to the bulk modulus of the test material. For a very weak or poor consolidated sedimentary rocks, like chalk, if a high pore pressure is applied to the sample and it is higher than the failure strength of the chalk, it will destroy the sample (Fjær et al. 2008, page 268). With cements and geopolymer cements this is unlikely to happen.

2.5.4 Purpose of triaxial compression test (deviatoric phase)

The purpose of a triaxial compression test is to determine the Young's modulus, Poisson's ratio and the compressive strength of a material test sample under representative reservoir stress conditions. The triaxial test are normally executed on a 90° vertical plane. A single-stage test, requires a minimum of 3 tests (McPhee et al. 2015). Where the plug or test samples are tested at different confining pressures. While a multiple-stage tests are carried out on a single plug sample with multiple increments of confining pressure steps.

The rock sample peak strength will increase with the surrounding confining pressure increases in value. Thereby the choice of value of confining pressure is an important decision. It should also be linked to downhole conditions, or the possible stress planes the material or rock is going to be subjected to. If reservoir pressure is going to be the reference for the confining pressure it should be the pressure before the start of production of petroleum. To determine the materials strengths (McPhee et al. 2015).

2.5.5 Data Utilisation

The Young's modulus and Poisson's ratio (ν) will be determined for each confining pressure at around 40% to 60% of the peak stress. Where the confining pressures, may be selected for wellbore stability analysis and not for in-situ, original stress plane, for rock properties like stress strength (McPhee et al. 2015).

In these tests the deviatoric phase might be restricted to ensure the data is acquired in a linear elastic regime. Meaning the test plug is not tested to failure, but to 40% to 60% of the maximum strength of the material (McPhee et al. 2015).

At higher in-situ pressures, formations are less likely to fail due to shear and fracturing due to the surrounding stress will hinder movement of the grains in the rock as it has to overcome in-situ stress to move. While at lower in-situ stress, the force applied on the formation is less and therefore the movement within the formation has less force to overcome. At lower confining pressures materials will act in a more brittle way than at higher confining pressures. While at higher confining stress, the material's stress-strain relationship will have less brittle behaviour and more plastic in deformation (McPhee et al. 2015).

3. Experimental Methodology and Experimental set up

The testing was performed at UIS SWIPA (Subsurface Well Integrity Permanent Abandonment) and Core laboratories with assistance from lab personnel. The testing was divided in two operations; prepare geopolymer samples and perform stress tests on the samples in a Triaxial cell. Total of 20 samples was made and tested.

3.1 Preparation of JAW-B Geopolymer test samples

The preparation of the samples is a meticulous process. The geopolymer mix require one hour to make the sample ingredients to make the slurry, as outlined in Table 3. To minimize sources of error and ensure reproducibility, the responsibility of mixing the slurry was assigned to a fellow student. Further the samples underwent a week-long curing period under controlled conditions, allowing the geopolymer to undergo geopolymerization. This dedicated

procedure was repeated to ensure consistency and repeatability in the subsequent testing and analysis of test data.

Table 3 JAW-B recipe

Component	Amount [g]
Granite	340
Ground-Granulated Blast Furnace Slag	330
Micro silica	30
Potassium Silicate (Solid activator)	145.3
Distilled water	254.2
Potassium hydroxide (KOH) 12M (Liquid accelerator)	64.55

3.1.1 Preparation of equipment and weighing of dry and liquid components

Safety measures and preparation were implemented prior to the preparation of the samples. These measures included ensuring the availability of appropriate safety gear and clean tools. The safety gear consisted of glasses, gloves, a laboratory coat, a respirator, and a fume cupboard. Due to the sample components consisting of fine particles, wearing a respirator was necessary to prevent breathing in the dry components. The weighing of the dry components occurred in the fume cupboard, to further minimizing any potential exposure. in a bucket placed in the fume cupboard while wearing the respirator.

To prevent cross-contamination a designated bucket was used to weigh the dry components. The bucket was divided into separate sections, and the dry components was placed in the separate sections, resembling pyramids. Each component was carefully weighed any excess material was easily removed without contaminating the other components. Once all the dry components were weighted, the bucket was sealed with a lid to properly seal the bucket to avoid spreading the fine particles. Then to ensure proper mixing of the dry components, the sealed bucket was vigorously shaken for a minimum of one minute. Thereby, effectively blending the components together.

3.1.2 Mixing dry phase and liquid phase

The dry mix was carefully transferred into a metal cup using a funnel, ensuring a mess-free transfer from the bucket. Before proceeding with the mixing, the blade of the mixing cup was checked for smooth movement and any sign of leakage. Next, the distilled water and the liquid accelerator were weighed and added and mixed in the mixing cup. Further, the mixing cup was placed on the OFITE Model 20 Constant Speed Blender for cement, pictured in Figure 15. The mixer was turned on with the pre-set mixing mode and the dry components were gradually added to the mixing cup. To ensure a complete mixing, a spatula was used to push the dry any components sticking on the top down towards the mixing blade.

Once a homogenous slurry was achieved, about 75% of the slurry was carefully transferred to a clean and dry conditioner cup, pictured in Figure 16. While the rest of the slurry was discarded in a designated waste container. The conditioner cup was secured by aligning the lid with the pins and carefully turning lid, to create a tight seal.



Figure 15 Mixing cup and OFITE Model 20 Constant Speed Blender for cement mixing

3.1.3 Preparing the consistometer and conditioning the geopolymer slurry

To ensure a homogenous mixture and simultaneously raising the slurry temperature, the utilization of a consistometer (*OFITE model 60 Atmospheric consistometer*) as depicted in Figure 17. Before commencing the conditioning of the slurry, the water level within the consistometer was inspected and adjusted to ensure the water covered the conditioning cup. The conditioner cup was inserted in the consistometer. To promote the desired slurry temperature, the consistometer was set to 30°C. The slurry was left to be conditioned for 30 minutes slurry at 30°C. During the conditioning of the slurry a autoclave cell was filled with room temperature water.



Figure 16 Conditioner cup and mixing blade



Figure 17 OFITE model 60 Atmospheric consistometer used to condition the geopolymer

During the initial stages of the experimentation, it was observed that after the conditioning the slurry was not 100 % homogenous. A thin layer on the top, indicating inadequate mixing of the slurry. This inconsistency was initially ignored for the first seven samples. This inconsistency was detected in a discrepancy in the yield stress, of 3 MPa or more, of the first

seven samples. This prompted a change in the procedure from the eight sample (SLL8) to address this discrepancy. The solution was to carefully to mix the slurry with the mixing blade manually and then mixing with a spatula.

3.1.4 Greasing of moulds

To facilitate smooth release of the samples from the moulds, High temperature grease (Superfilm HI-temp extreme pressure grease) was used. This choice of grease proved crucial to ensuring the samples had a consistent release from the moulds. As during the initial stages of testing a low-cost silicone-bases grease was used and it led to damaged samples. To remove additional sources of errors, a systematic approach was utilized by using the same moulds to increase the repeatability of the samples structure. The moulds were assembled and numbered from 1 to 4, ref Figure 18. The numbering system from one to four minimized the potential variability between the mould, thereby increasing the repeatability.

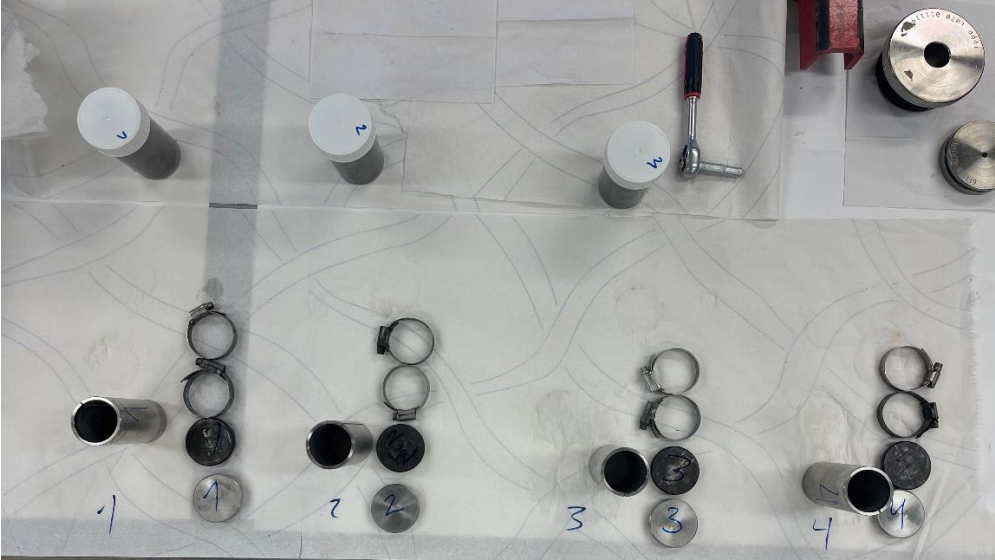


Figure 18 Setup of 4 curing cells, before greasing and assembly

3.1.5 Filling of moulds with geopolymer slurry and placing the moulds in an autoclave cell

The curing mould was carefully filled with the prepared slurry, leaving a gap of 0.5 cm at the top. In the case of the first seven samples, a small amount of water was added on top of the slurry. However, from the eighth sample, topping of water was omitted since it could dilute the slurry top layer and introduce another source of error. To avoid slurry spilling out of the mould lid a paper towel was placed on top before securing the lids. Next, the filled moulds were gently placed in the Autoclave curing cell, which naturally reduced the water level in the Autoclave cell. After the addition of the moulds, the water level was adjusted by adding or removing room tempered tap water until the water level reached the designated mark. Once the water level was properly adjusted, the inner autoclave cell lid was secured by using the key tool pictured in Figure 21. Any excess water which remained in the curing cell was removed using paper towels and a compressed air gun. After ensuring the area was fully dry, the outer lid of the Autoclave cells was secured. The autoclave lids are pictured in Figure 20. To finalize the preparation, any spilled water was cleaned up, and the fully assembled Autoclave cell was placed in a heat cabinet set to 90°C.



Figure 19 Autoclave curing cell



Figure 20 Autoclave cell Inner (left) and Outer lid (right)

3.1.6 Curing of samples

Prior to increasing the pressure in the Autoclave cell, several steps were taken to ensure a smooth operation. Firstly, the water level in the pump reservoir checked to avoid any intake of air into the pumps. If the water level was low, it was replenished with distilled water. Distilled water was used to minimize the risk of deposits forming in the pump and piping. To identify The pump was then turned off, and if there were any other Autoclave curing cells inside the heat cabinet, their inlet valves were closed (one inside and one outside). This was to prevent any pressure shocks from opening unused valves.

To identifying an unused pipe within the heat cabinet, the pump was restarted pump mode was changed to Paired delivery rate (PDR) with a rate of 3 ml/min. Once a suitable line was located, the pump was stopped, and the pipe was connected to the upper inlet valve of the Autoclave cell with a wrench. To eliminate any trapped air are within the Autoclave cell, water was pumped into the cell while loosening and tightening the nut.

Once the air was removed, the pressure within the Autoclave cell was gradually increase by using the PDR pump mode. The pump rate was 15 ml/min until reaching 1800 psi. At this point the pump rate was changed to 10 ml/min, which facilitated better control when stopping the pump at 2000 psi. The pump mode was then changed to pump mode to Pair Pump bi-directional (PPBD) and the inlet valves in use were slowly opened. Finally, the fully assembled Autoclave cell was left in the oven to cure at 2000 psi and 90°C for a duration of one week. This controlled environment allowed for the proper development of material strengths.

3.1.7 Removal of autoclave cell from the oven

After a one week of curing period, the pumps were promptly stopped, and all valves were slowly closed. To handle the equipment inside of the heat cabinet, heat protection gloves were worn to disconnect the connected line to the Autoclave cell. The Autoclave cell was removed carefully from the heat cabinet and marked with “High pressure and temperature – HOT, Do NOT Touch”. This sign served as a visual reminder to handle the hot cell with care. To allow the cell to gradually cool down to room temperature, it was transferred to a designated cooling area. The cooling process took approximately 7 hours.

3.1.8 Removal of test moulds from autoclave cell

After the Autoclave cell had fully cooled down to ambient temperature, proper protection gear including protective glasses, gloves and a lab coat was worn. The upper valve was slowly opened to release the accumulated pressure inside the Autoclave cell. If necessary, the lower valve of the Autoclave cell could be opened to allow for better drainage of pressure. To open the cell, the outer lid was partially turned to facilitate an opening for the inner lid. Subsequently, the inner lid was opened by using a key as depicted in Figure 21. Both lids were removed, and the wastewater and samples were drained into a prepared bucket. Any accidental spilled wastewater was cleaned up using paper towels, to maintain a clean and safe working environment. The wastewater was carefully disposed in a sink with running water, to minimize any potential damage to the plumbing system.

The moulds were disassembled, and the individual test cells were placed in separate plastic cups filled with tap water. In case any test cells were firmly stuck in the moulds, warm tap water was employed to help releasing the test cells from the moulds. Following the removal of the samples the moulds were thoroughly cleaned and any traces of geopolymer residue were removed with the aid of steel wool or a steel brush.



Figure 21 Autoclave key

3.1.9 Measuring, marking and cutting the test sample

The sample was extracted from its cup and clearly labelled with arrows point upwards marked with a pencil. A length of 75 mm of the sample was measured and marked, from the bottom to the top. This specific length was chosen to remove the top of the sample, which might contain contaminations from the tap water used during the curing process. The sample was securely fastened with utmost care in a clean cutting machine, *Discotom* ref. Figure 22, since build-up of residue and dust can affect the cut of the sample. The sample were cut at the designated 75 mm mark, and any residual debris was promptly removed by vacuuming.



Figure 22 Discotom Cutting machine

3.1.10 Polishing of test samples

The sample was polished by using a Baldor GCTS RSG-75 cutting and polishing machine as depicted in Figure 23. To ensure the sample's integrity and prevent any damage the sample was secured in a manual feeder. The sample was carefully secured in the feeder to avoid damaging the sample. Next, the sample was aligned against the polishing surface of the machine, only leaving a paper-thin gap against the polishing surface. As shown in Figure 24. The increment handle of the machine was set to zero, to ensure a consistent polishing interval.



Figure 23 Baldor GCTS RSG-75 cutting and polishing machine

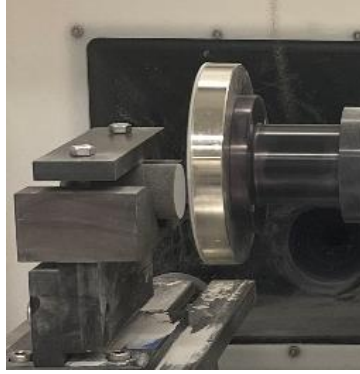


Figure 24 Close up of sample lined up with the polishing surface

The machine was turned on and the polishing process commenced by incrementally advancing the sample by steps of 0.5 (0.005" or 0.127mm) per pass, as pictured in Figure 25. The lid of the machine closed the vacuum system was activated. The sample underwent the polishing until its surface achieved a consistent and uniform. Since a uniform colour indicated an even and smooth surface texture. This polishing procedure was performed on both sides of the sample to ensure optimal results.

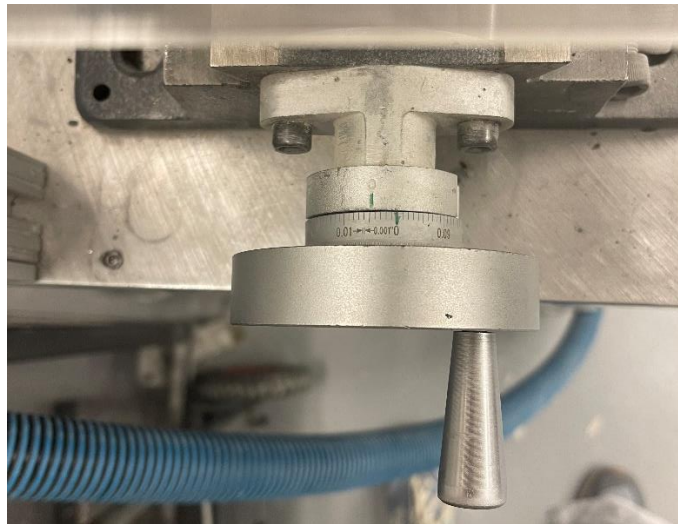


Figure 25 Baldor cutting, and polishing machine left side handle

After the cutting and polishing process, the sample was measured. To prevent any chipping of the sample corners, the sample was submerged in water for a minimum 30 seconds in the water, carefully dried, and then weighted. The detailed measurements can be found in Table 4 on the next page.

Table 4 Length, diameter and weight of samples before triaxial testing

Sample	Length [mm]	Diameter [mm]	Weight [g]
SLL1	73.75	37.99	-
SLL2	72.28	37.98	-
SLL3	76.38	37.95	165.71
SLL4	69.45	37.88	148.28
SLL6	75.57	37.93	156.94
SLL7	74.83	37.89	159.09
SLL8	73.25	37.94	159.69
SLL9	74.17	37.95	161.28
SLL10	74.44	37.94	160.72
SLL11	69.65	37.98	151.41
SLL12	73.65	37.98	159.90
SLL13	73.35	37.98	158.98
SLL14	74.27	37.97	160.24
SLL16	74.81	37.99	162.62
SLL17	73.58	37.95	159.20
SLL18	74.15	37.96	162.10
SLL19	72.5	37.98	158.38
SLL20	73.81	37.96	159.67

3.2 Triaxial cell testing

After the preparation of the samples, a triaxial cell was utilized to conduct all necessary testing to require the essential data to be able determine the material strengths of the samples.

Following the sample preparation, a triaxial cell was employed to perform testing and obtain data for determining the material strengths of the samples.

3.2.1 Triaxial cell preparation

To ensure a reliable and repeatable testing process, multiple steps were taken to prepare the triaxial cell. Firstly, the confining chamber drainage valve was securely closed, to prevent

any leakage of confining oil during filling of the confining chamber. Next, the water injection inlet and outlet tubing were flushed with air, to remove residue from the previous test. A shrinking sleeve measuring 12 cm was prepared, which was large enough to cover the sample and the two O-rings on the upper and lower pistons, as shown in Figure 29. The O-rings of the confining chamber and equipment were checked to ensure they maintained their round shape. Vacuum cream grease was used to lubricate the O-rings to create a good seal, separating the confining oil from the test sample, shrink sleeve and the water injection equipment.

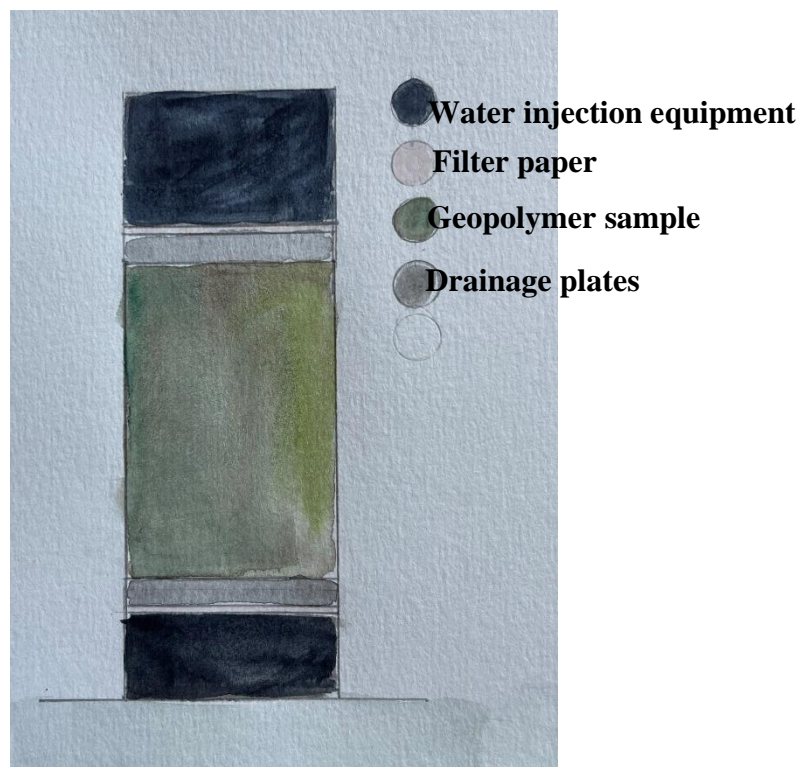


Figure 26 Sample between drainage plates and water injection equipment

To prevent clogging of the tubing piping from test sample residues, two filter papers with the size of the draining plate were cut out from coffee filter paper. These filter papers were installed before the top draining plate and after the bottom draining plate, as illustrated in Figure 26. Additionally, rubber sleeves were utilized to cover the end faces of the sample, drainage plates, and the end faces of the steel pistons. These sleeves helped centralize the core and drainage plates above the steel pistons, as depicted in Figure 27. Ensuring proper alignment is crucial as an off-centre core and drainage plates can cut the shrinking sleeve at high pressures, leading to leakage and test failure.



Figure 27 Water drainage plates and rubber rings

3.2.2 Triaxial cell assembly

The test sample was carefully positioned on the elevated cylinder located at the bottom of the triaxial cell, as depicted in Figure 28. This setup involved connecting the sample, drainage plates, filter paper, and rubber packers. Next, the shrink sleeve was threaded around the sample with the water injection unit positioned above it. The shrink sleeve was precisely aligned to cover both O-rings and the sample, as shown in Figure 29.

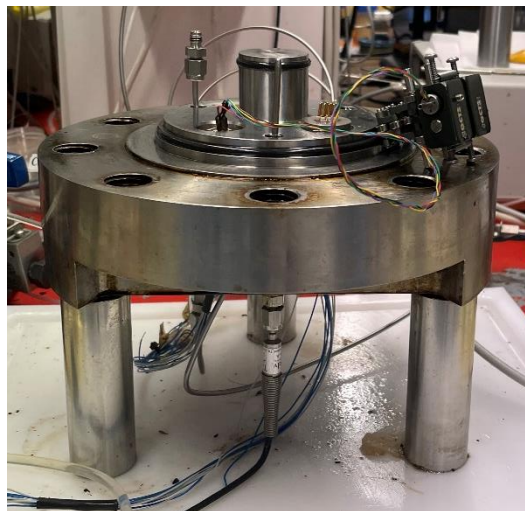


Figure 28 Bottom of the triaxial cell

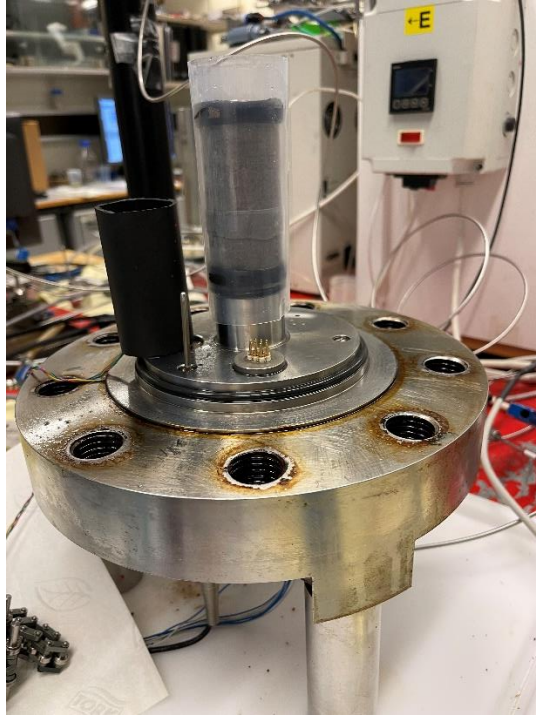


Figure 29 Sample with 3/4 heated shrink sleeve

To facilitate the installation of the extensometer, the water injection unit was temporarily removed Figure 30, and the exposed wires were securely covered with a rubber cylinder. Three-fourths of the shrink sleeve were heated using a heat gun, starting from the bottom and moving upwards. Subsequently, an extensometer Figure 31, serving as a logging tool for measuring the diameter during the test, was carefully placed around the sample, following the configuration shown in Figure 32.



Figure 30 Top of water injection unit

A calibration check of the extensometer was performed by measuring the sample diameter within the range of 38.8 mm to 39 mm, using the LabVIEW logging program. Additionally,

the extensometer was manually extended to verify if the extension was accurately reflected in LabVIEW, ensuring its proper functionality.

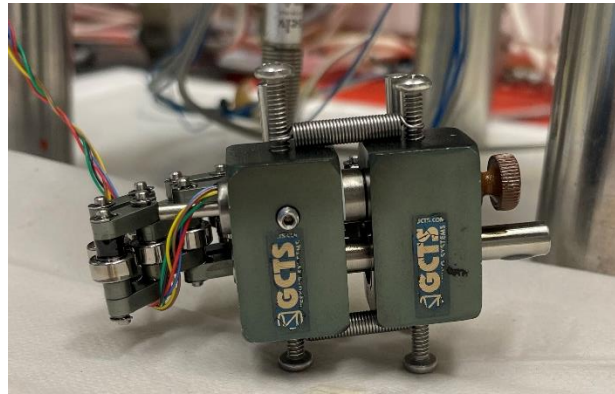


Figure 31 GCTS Extensometer

Once the extensometer was successfully verified, it was repositioned to the bottom of the sample to prevent any potential damage to the electronic cables during the final heating of the shrink sleeve. The top water injection unit was then reinstalled on the top of the test sample, ensuring that the simmering covered the interface between the unit and the sample. It was subsequently adjusted to align the pipe with the connection outlet. The remaining portion of the shrink sleeve was heated in place using a heat gun, while simultaneously holding down the top of the water injection unit to prevent movement. Finally, the tubing from the top of the water injection unit was connected to the outlet tubing and securely tightened.



Figure 32 Fully assembled test set-up on the inner part of the confining chamber of a triaxial cell

3.2.3 Placing the confining chamber and assembling the triaxial cell

The Extensometer was positioned at the centre of the test sample, while the confining chamber was carefully placed at the bottom of the triaxial cell. To ensure uniformity, the space between the bottom and the chamber was adjusted to have the same height all around, facilitating the movement of the chamber without any difficulty, as depicted in Figure 33. Additionally, the confining chamber Figure 34, was rotated to prevent any potential clash between the heating jacket power cable and the Triaxial cell fastening bolts. Once the chamber was correctly positioned, it was filled with Marcol 82 oil up to the designated mark inside the confining chamber. Prior to installing the top of the confining chamber, the confining outlet valve was opened to allow for any excess oil to be drained into a container.



Figure 33 Confining chamber correctly placed on the bottom of the Triaxial cell



Figure 34 Confining pressure installed, from above and from the side

Due to the confining chamber top weight (20 kg), a special designed crane was used to install it on the confining chamber Figure 35. All nine bolts were installed, first by hand tightening, and then by performed the final fastening win an electric torque wrench the bolts holes where line up the top with the bottom, allowing for the bolts to be screwed in easily. The nine bolts were installed / torqued 500 Nm, first by hand tightening and then finally by using an electric torque wrench and tightened every third bolt in two rounds. A protective aluminium plate was placed above the confining chamber top to protect its surface. The upper piston outlet valve was connected to the top of the triaxial cell. The axial LVDT Figure 36, was placed on the top of the triaxial cell and making sure that the axial pin could move freely. The fully assembled triaxial cell is represented in Figure 37.



Figure 35 Top of triaxial cell (left) and installed top of the triaxial cell on the confining chamber



Figure 36 LVDT Axial movement logging equipment

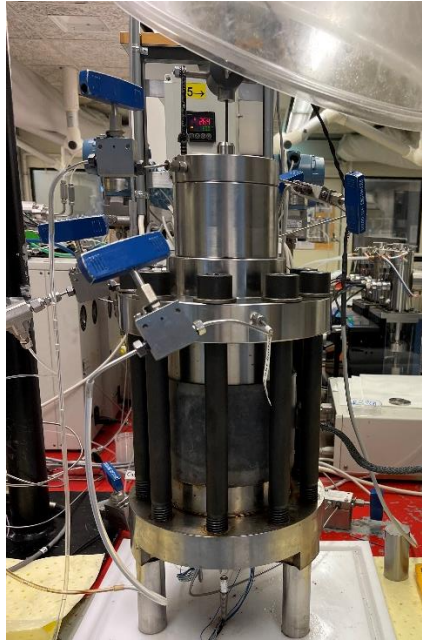


Figure 37 Fully assembled triaxial cell

3.2.4 Pump and logging program setup

Prior to starting the test, it was necessary to release any residual pressure from the valve cavities, tubing, and pumps Figure 39 in order to reset the pressure sensors to zero. This process, also known as "pressure zero," involved opening all control valves within the pump program VPware, as illustrated in VPware the pump program used to control the pumps Figure 38. Additionally, the pump configuration was accessed, and the auto zero pump feature was enabled. This step ensured that the reference pressure of the pumps matched the atmospheric pressure in the laboratory.

Following the pressure zero procedure, the logging program was restarted and named according to the specific sample being tested, including the test temperature and load rate. The hydrostatic loading program, which incorporated automatic internal piston friction compensation, was activated. The temperature was set to 90°C, and the logging time value was adjusted to 0.1 minutes.

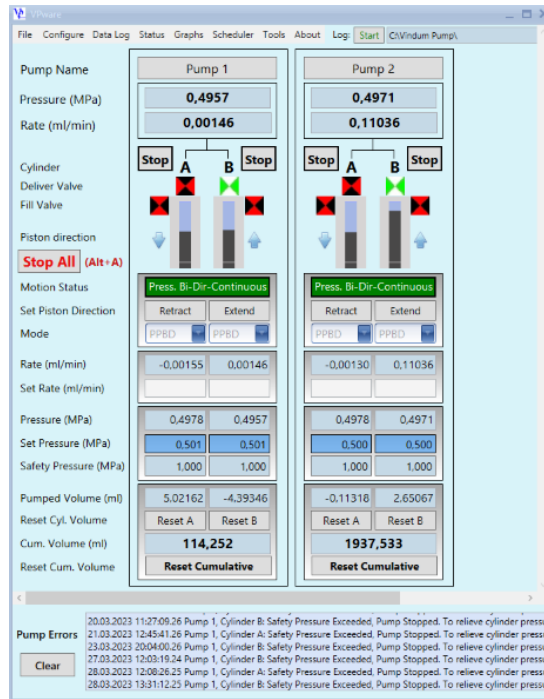


Figure 38 VPware the pump program used to control the pumps

3.2.5 Increasing of confining pressure to 0.5 MPa

Prior to initiating the test, several steps were taken to ensure proper setup and control of the confining pressure. The initial confining pressure was adjusted to 0.5 MPa, and a safety pressure limit of 1 MPa was set. This meant that if the pump pressure exceeded 1 MPa, the pump would automatically stop as a safety precaution. The confining pump, pump 2, was started in Pump mode using the Paired Rate Delivery (PRD) setting, with a pump rate of 3 ml/min. It was important to consider the possibility of trapped air in the confining chamber, so the outlet valve of the chamber was kept open. This allowed any trapped air to be vented until only oil was flowing out of the chamber. Once all air was evacuated, the outlet valve was closed.

To monitor the pressure increase in the confining chamber, the LabView program's axis was changed to confining pressure on the y-axis and time on the x-axis, see Figure 40. After the confining pressure was successfully raised from 0 MPa to 0.5 MPa, the pump mode was switched to Pump Pressure Bi-Directional (PPBD). This mode enabled the pump to maintain the pressure at the predetermined value of 0.5 MPa throughout the duration of the test.



Figure 39 Vidum VP-series High-Pressure Metering Pumps

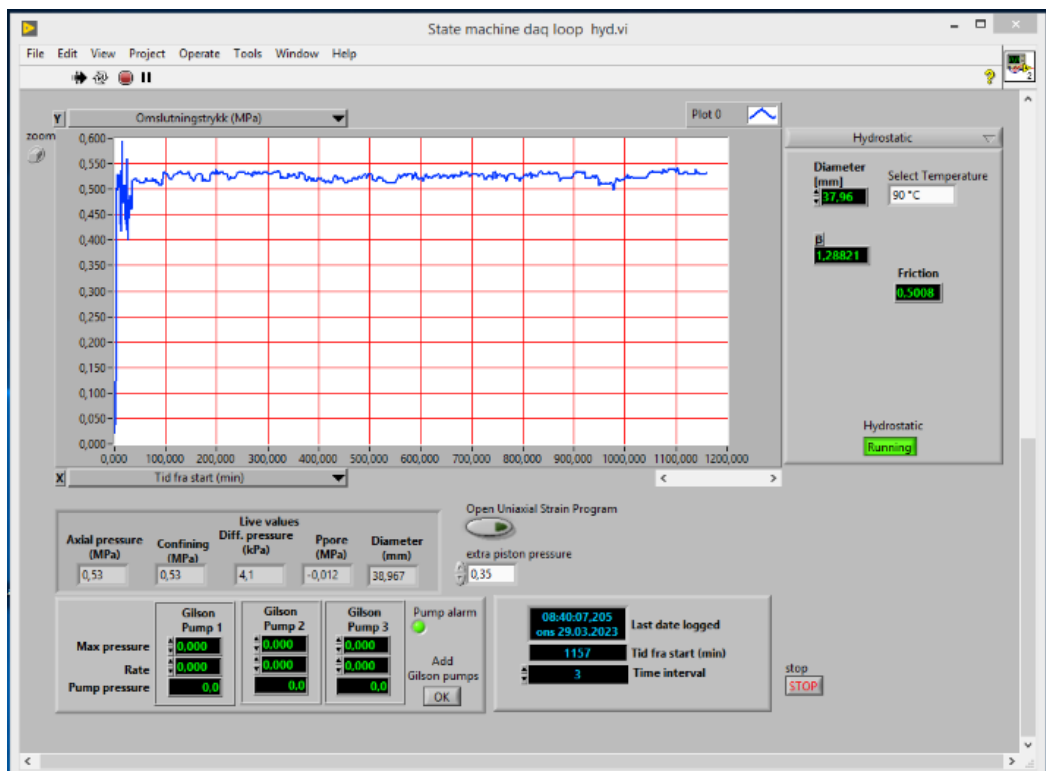


Figure 40 LabView Logging program used to log data

3.2.6 Lowering piston

To initiate the movement of the piston within the top of the triaxial cell Figure 41, the inlet piston valve, upper outlet valve, and lower outlet valve were opened. The LabVIEW configuration was adjusted to reflect the changes in monitoring. The y-axis was set to piston pressure, while the x-axis was set to axial movement. This allowed for real-time observation of the piston's movement during the test. The piston pump, pump 1, was activated in Pump mode using the Paired Rate Delivery (PRD) setting in the VPware program. The pump rate was set to 2 ml/min, and a safety pressure limit of 1 MPa was set. The upper outlet valve connected to the piston was closed once the system had been evacuated of air, ensuring that only oil was flowing through the system. The piston reached the desired position when the safety pressure was achieved, causing the pump to automatically stop.

Subsequently, the pump mode on the piston pump was switched to Pump Pressure Bi-Directional (PPBD) in the VPware program. This mode allowed the pump to maintain a constant piston pressure. In LabVIEW, an additional preset value of 0.35 MPa, referred to as extra piston pressure, was implemented. This additional pressure compensated for internal piston friction and ensured that the piston remained in contact with the sample during its deformation. The compensation for internal friction, caused by the piston O-rings, was regulated by the Hydrostatic program within LabVIEW, which worked in conjunction with VPware to control the piston pump pressure.

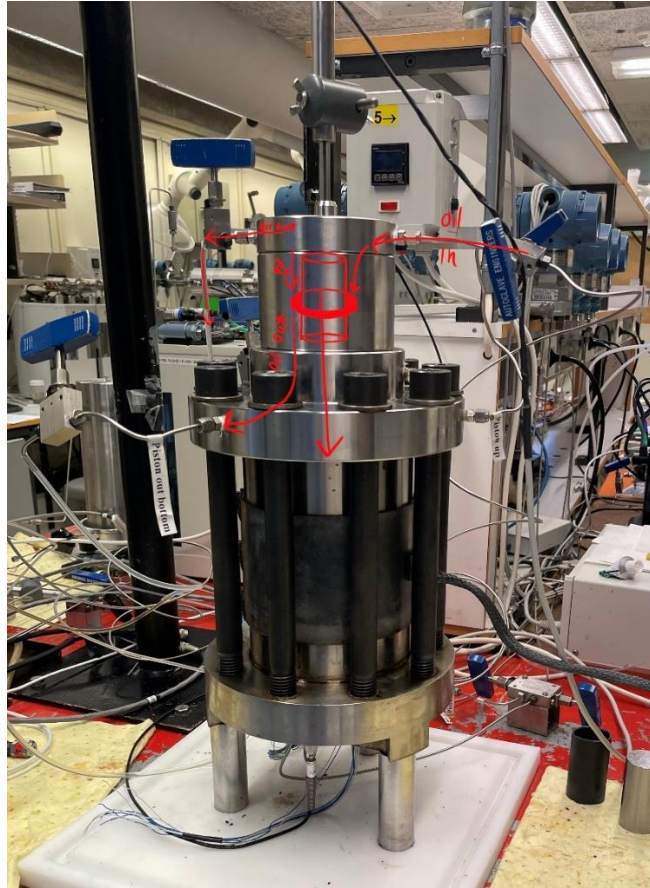


Figure 41 Figure illustrating how the piston was lowered from the top to the sample

3.2.7 Increasing of temperature to 90°C

The temperature of the triaxial cell was raised by connecting the heating jacket to the power cord and activating the temperature regulator, which was set to 90°C. To ensure proper ventilation, a movable fume hood was positioned above the cell. Additionally, a pressure control valve was connected to the outlet of the confining pressure outlet valve.

To maintain control over the confining pressure during the heating process, the confining pump was turned off initially. The pressure increase was manually regulated by monitoring the confining pressure instrument and adjusting the pressure control valve accordingly, as shown in Figure 42 . When the temperature approached approximately 80-85°C, the confining pump was started, and the confining pressure outlet valve was closed. In order to capture data at suitable intervals, the logging interval time was adjusted to 3 minutes. Subsequently, the triaxial cell was left undisturbed for approximately 20 hours to ensure the core temperature stabilized at 90°C. This period of time was necessary to secure a consistent and controlled temperature for the subsequent testing.



Figure 42 Pressure control valve used to regulate the pressure during heating of confining oil

3.2.8 Triaxial cell sample test

A total of 20 samples were subjected to testing following a predefined program, as outlined in Table 5. The system control software was programmed accordingly to accommodate the specific requirements of each test, as detailed in Table 6. The VPware pump control software was configured for both the confining and piston pumps, aligning with the desired confining pressure and piston load rate specified in the program. Additionally, pressure decrease schedules were established. In LabVIEW, the logging time interval was adjusted from 3 minutes to 0.01 minutes for more frequent data recording. The y-axis was set to represent the confining pressure, while the x-axis was adjusted to display axial movement and extensometer readings. To ensure uninterrupted operation during the tests, the safety pressures for both the piston pump and the confining pump were modified to 70 MPa, thus minimizing the risk of the pumps stopping prematurely. The hydrostatic phase was initiated by gradually increasing the confining pressure from 0.5 MPa to the desired levels of 8 MPa, 17.2 MPa, and 26 MPa, with a consistent rate of 1.67 MPa/minute, in accordance with the predetermined schedule. Upon completion of the hydrostatic phase, the piston pressure was recorded in the notepad for future reference. This value was utilized when reducing the pressure in the piston pump after the test core/sample had failed. At this stage, the y-axis in LabVIEW was switched to represent the piston pressure, while the x-axis remained unchanged.

Table 5 Test program

Piston load rate Confining pressure	0.5 [MPa/min]		12 [MPa/min]		35* [MPa/min]	
	8 [MPa]	SLL8	SLL9	SLL10	SLL11	SLL12
17.2 [MPa]	SLL6	SLL7	SLL1	SLL2	SLL3	SLL4
26 [MPa]	SLL14	SLL20	SLL16	SLL17	SLL18	SLL19

Table 6 Pump schedule values for the two test phases (Hydrostatic and Deviatoric)

Schedule	Pump	Pump rate [MPa/min]	Safety pressure [MPa]	Estimated test duration [s]**
Hydrostatic phase				
8 [MPa]	Pump 2	1.67	70	269
17.2 [MPa]	Pump 2	1.67	70	600
26 [MPa]	Pump 2	1.67	70	916
Deviatoric phase				
	Pump 1	0.5	70	7286
	Pump 1	12	70	304
	Pump 1	35*	70	104

* the piston pump was unable to reach a pump rate of 35 MPa/min.

** Since the schedule set-up in the pump control software could only be programmed with start pressure, safety pressure and time to reach duration. The estimated test duration was calculated by dividing

$$1. \text{ Hydrostatic phase: } \frac{\text{Confining pressure [MPa]} - 0.5 \text{ [MPa]}}{1.67 \text{ [MPa/min]}} = \text{time [min]}$$

$$2. \text{ Deviatoric phase: } \frac{60.72 \text{ MPa}}{\text{pump rate } \left[\frac{\text{MPa}}{\text{min}} \right]} * 60 = \text{time [s]}$$

The deviatoric phase commenced by deactivating the hydrostatic program and initiating the piston pressure schedule with the desired piston load rates of 0.5 MPa/min, 12 MPa/min, and 35 MPa/min. The deviatoric loading process ceased upon failure of the sample, which

was indicated by an extensometer reading in LabView that exceeded 40 mm in diameter. Once the sample failed, the piston pump was manually halted, and the piston pressure began to decrease. To ensure controlled depressurization of the piston pump, the depressurization schedule was activated and executed for a duration of 10 minutes. After the piston pressure had reached the value recorded at the end of the hydrostatic loading phase, the hydrostatic program was reactivated. Subsequently, the confining pressure was gradually reduced according to a schedule of 10 minutes for 8 MPa and 17.2 MPa, and 16 minutes for 26 MPa. Following the pressure reduction in the confining chamber, the confining pump was switched to Pump Pressure Bi-Directional (PPBD) mode with a pressure of 0.5 MPa. The power supply to the heating jacket was switched off. The safety pressures for both pumps were reset to 1 MPa. The triaxial cell was then left to cool down until the internal temperature reading reached approximately 35°C, which typically took around 4 hours

3.2.9 Cooling of the triaxial cell and lifting of piston to start position

The piston pump was halted once the temperature of the confining chamber reached 35°C. Subsequently, the lower piston outlet valve was closed, the upper piston outlet valve was opened, and the piston inlet valve was switched from "piston in" to "piston up," as depicted in Figure 44 . The piston pump was then restarted, and in LabVIEW, the y-axis was configured to display piston pressure, while the x-axis was adjusted to show axial movement. The piston was lifted to its initial position once the axial movement graph returned to its starting position, as shown in Figure 43.

Next, the confining pump was stopped, and the confining pressure was gradually released by slowly opening the drain valve. The logging program was stopped. Before draining the oil from the confining chamber, it was ensured that the drain hose was properly connected to the drain container. The chamber was drained by connecting the pressurized air hose to the confining pressure outlet valve and opening the confining drainage valve. This process involved flushing air into the confining chamber, allowing the oil to be drained into a designated waste oil container. For reference, please consult the P&ID schematic of the triaxial cell provided in Figure 44.

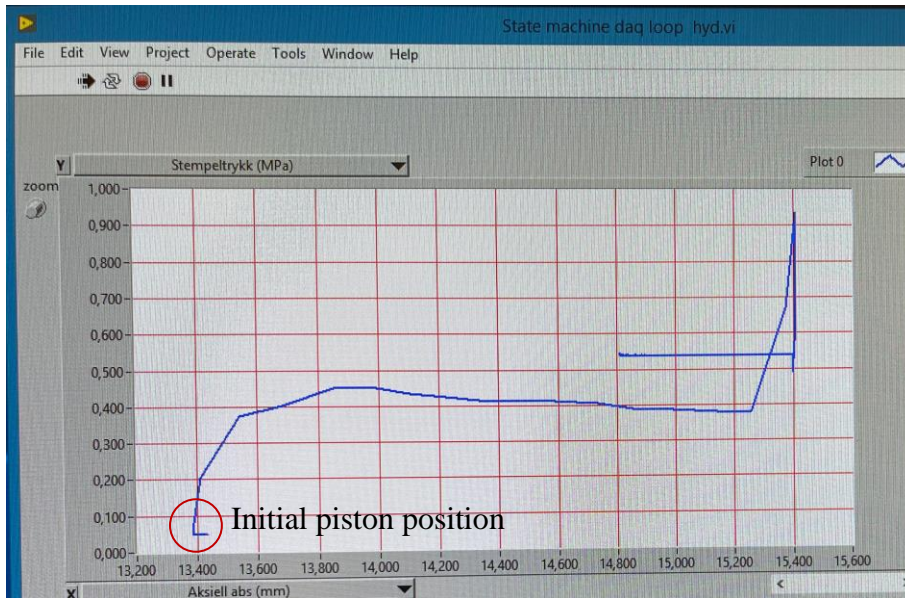


Figure 43 LabView graph showing the initial position of the piston and its movement during the test

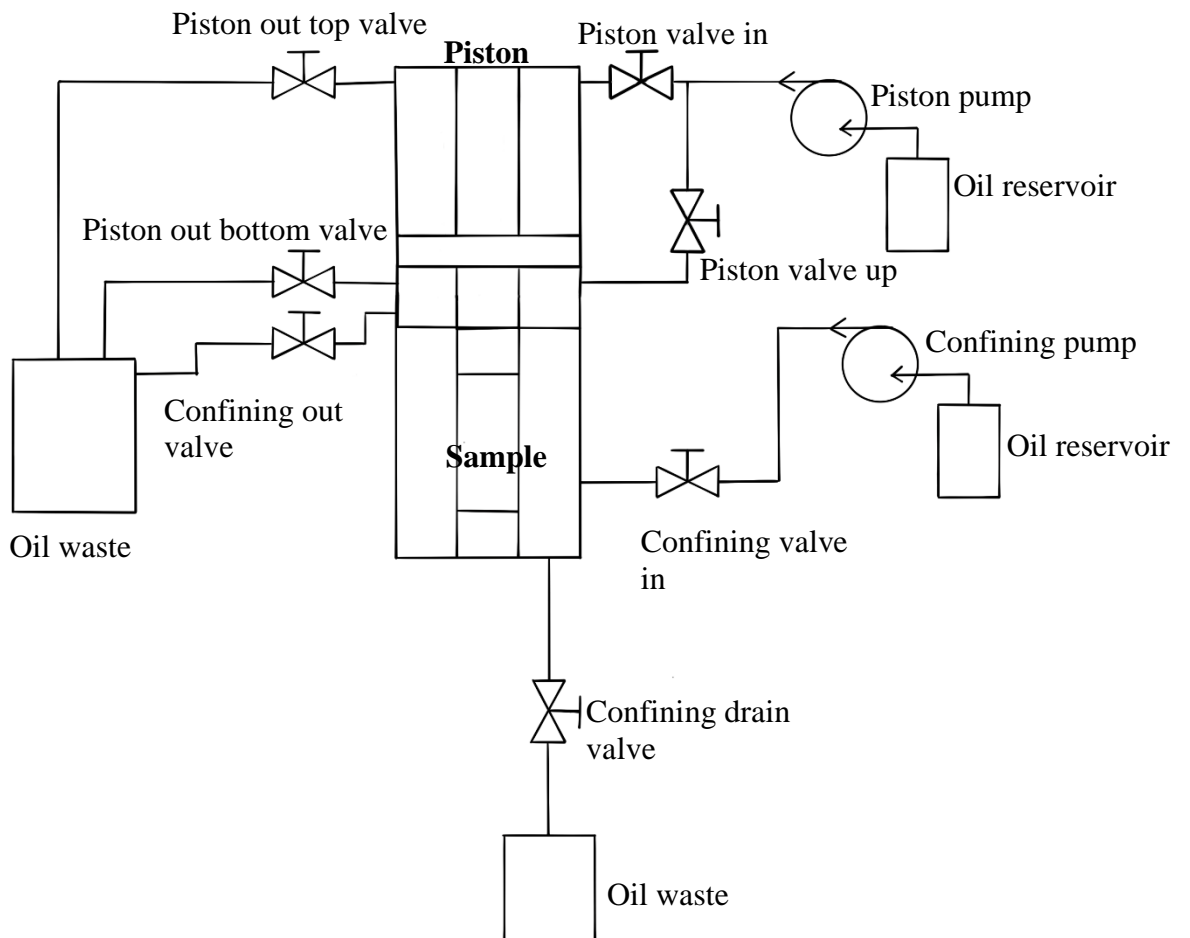


Figure 44 P&ID schematic of the triaxial cell and pump setup for piston and confining pumps

3.2.10 Disassembly of the triaxial cell

The disassembly process of the triaxial cell commenced by removing the LVDT (Linear Variable Differential Transformer) and the axial pin, along with the upper piston outlet valve. Using the electric torque wrench, the bolts were loosened in the same manner they were tightened during the assembly of the triaxial cell. With the assistance of a crane, the top part of the triaxial cell was carefully lifted out, and any excess oil around the piston was wiped clean using a paper towel. Subsequently, the confining chamber was lifted off the lower part of the triaxial cell and placed on the floor beneath the table. Any excess oil present around the sample and on the surface of the bottom of the triaxial cell was cleaned using paper towels. The connecting nuts on the top of the water injection unit tubing were loosened, and the unit was then removed. Following that, the extensometer was handled with care and gently taken out, placing it on a paper towel to absorb any excess oil. Next, the failed sample was removed, and the shrink sleeve was cut using a wallpaper knife. The weight of the sample was measured to assess the amount of water lost during the test. Pictures of the sample were taken, as depicted in Figure 45 below, and the sample was stored in its plastic container for future investigations. The rubber packings, water injection medallions, and the workspace were thoroughly cleaned to maintain a clean and organized environment.



Figure 45 Geopolymer samples after the deviatoric phase (failed samples)

3.3 Data analysing methods

For each test, the LabView software generated a log file that was subsequently imported for in-depth analysis. The log file provided data to calculate various parameters, including axial stress, axial strain, radial strain, volumetric strain, and Poisson's ratio. These calculations played a significant role in understanding the behaviour of the tested sample.

Using the obtained data, stress-strain diagrams were plotted for both the hydrostatic and deviatoric loading phases. These diagrams allowed for a visual representation of the sample's response under different loading conditions. Furthermore, utilizing the stress-strain diagrams, important material properties such as bulk modulus, Young's modulus, and compressive strength were estimated.

3.3.1 Hydrostatic loading phase

The axial stress applied on the test sample, is derived from the recorded confining pressure, piston pressure and internal friction during the triaxial test. The axial stress was calculated based on the following equation 19. Figure 46, depicts an example on how the axial stress was calculated in excel.

$$\sigma_{axial} = P_{Confining} + f_{internal}(P_{piston\ pressure\ factor}) * (-0.00994908 * P_{Confining} + 0.195673) \quad (19)$$

	J	K	L	M	N	O	P	Q	AE
1									
2	Rate(P3)	Temperatur	Diff.trykk	P_piston	P_conf	P_pore	Aksiell abs	Extensomete	Axial Stress
1512	0	89,753131	4,043099	0,499242	0,516	-0,011889	13,967682	38,806533	0,90024437
1513	0	89,723941	4,042169	0,498991	0,516	-0,01189	13,967596	38,806534	0,8999212
1514	0	89,757095	4,041206	0,498762	0,516	-0,011902	13,967806	38,806536	0,89962635

Figure 46 How sample SLL14 axial stress was calculated in excel

The strain of the sample was determined by analysing the recorded change in axial movement, which served as an indicator of axial strain. The calculation of strain was performed using Equation 20, and the values were computed in Excel for each log step. These calculated strain values were then utilized to construct the stress-strain diagram specifically for the hydrostatic loading phase. This phase involved incrementally increasing the confining pressure from its initial value of 0.5 MPa to the desired levels of 8 MPa, 17.2 MPa, and 26 MPa. To provide a visual representation of the calculations, the strain values were plotted using Figure 47.

$$\epsilon_{Axial} = \frac{Axial_0 - Axial}{L_0 * 100} [\%] \quad (20)$$

AF1514												
=(P1514-\$P\$1514)/74,27*100												
	J	K	L	M	N	O	P	Q	AE	AF	AG	AH
1										Hydrostatic		
2	Rate(P3)	Temperatur	Diff.trykk	P_piston	P_conf	P_pore	Aksiell abs	Extensomete	Axial Stress	Axial Strain	Radial Strain	Volumetric Strain
1512	0	89,753131	4,043099	0,499242	0,516	-0,011889	13,967682	38,806533	0,90024437			Start of Hydrostatic phase
1513	0	89,723941	4,042169	0,498991	0,516	-0,01189	13,967596	38,806534	0,8999212			
1514	0	89,757095	4,041206	0,498762	0,516	-0,011902	13,967806	38,806536	0,89962635	0	0	0

Figure 47 How sample SLL14 axial strain was calculated in excel

The radial strain of the sample was determined by analysing the change in circumference, which was quantified using Equation 21. Similar to the calculation of axial strain, the equation 21 was implemented in Excel to compute the radial strain values for each log step. These values were then utilized to construct the stress-strain diagram for the sample.

$$\epsilon_{Radial} = \frac{D_{extensometer\ ini} - D_{extensometer}}{D_{initial}} * 100 \quad [\%] \quad (21)$$

AG1514												
=(Q1514-Q1514)/37,97*100												
	J	K	L	M	N	O	P	Q	AE	AF	AG	AH
1										Hydrostatic		
2	Rate(P3)	Temperatur	Diff.trykk	P_piston	P_conf	P_pore	Aksiell abs	Extensomete	Axial Stress	Axial Strain	Radial Strain	Volumetric Strain
1512	0	89,753131	4,043099	0,499242	0,516	-0,011889	13,967682	38,806533	0,90024437			Start of Hydrostatic phase
1513	0	89,723941	4,042169	0,498991	0,516	-0,01189	13,967596	38,806534	0,8999212			
1514	0	89,757095	4,041206	0,498762	0,516	-0,011902	13,967806	38,806536	0,89962635	0	0	0

Figure 48 How sample SLL14 radial strain was calculated in excel

The volumetric strain was determined by considering the changes in both axial and circumferential dimensions of the sample. To calculate the volumetric strain, Equation 22 was utilized, similar to the approach used for axial and radial strain calculations. The obtained values were then employed to construct the volumetric stress-strain diagram, following the same procedure as for axial and radial strains. By examining the volumetric stress-strain diagram, a comprehensive understanding of the sample's response to various loading conditions was achieved. This diagram provided valuable insights into the sample's deformation characteristics, enabling a thorough analysis of its mechanical behaviour during the testing process. Figure 48 Illustrates the volumetric stress-strain diagram obtained from the calculations

$$\epsilon_{Volumetric} = \epsilon_{Axial} + 2\epsilon_{Radial} [\%] \quad (22)$$

=AF1514+2*AG1514												
	J	K	L	M	N	O	P	Q	AE	AF	AG	AH
1										Hydrostatic		
2	Rate(P3)	Temperatur	Diff.trykk	P_piston	P_conf	P_pore	Aksiell abs	Extensomete	Axial Stress	Axial Strain	Radial Strain	Volumetric Strain
1512	0	89,753131	4,043099	0,499242	0,516	-0,011889	13,967682	38,806533	0,90024437			
1513	0	89,723941	4,042169	0,498991	0,516	-0,01189	13,967596	38,806534	0,8999212		Start of Hydrostatic phase	
1514	0	89,757095	4,041206	0,498762	0,516	-0,011902	13,967806	38,806536	0,89962635	0	0	0

Figure 49 How sample SLL14 volumetric strain was calculated in excel

To account for the isotropic assumption, the volumetric strain was calculated based solely on the axial strain. Equation 23 was employed to determine the isotropic volumetric strain and Figure 50 is an example on how this strain was calculated.

$$\epsilon_{Volumetric} = 3\epsilon_{Axial} [\%] \quad (23)$$

=AF1514*3													
	J	K	L	M	N	O	P	Q	AE	AF	AG	AH	AK
1										Hydrostatic			
2	Rate(P3)	Temperatur	Diff.trykk	P_piston	P_conf	P_pore	Aksiell abs	Extensomete	Axial Stress	Axial Strain	Radial Strain	Volumetric Strain	iso vol
1512	0	89,753131	4,043099	0,499242	0,516	-0,011889	13,967682	38,806533	0,90024437			Start of Hydrostatic phase	
1513	0	89,723941	4,042169	0,498991	0,516	-0,01189	13,967596	38,806534	0,8999212				
1514	0	89,757095	4,041206	0,498762	0,516	-0,011902	13,967806	38,806536	0,89962635	0	0	0	0

Figure 50 How sample SLL14 isotropic volumetric strain was calculated in excel

Bulk modulus was determined with the usage of the volumetric stress-strain curve. From the slope of the graph. The slope was determined in the tree following methods, as some of the stress-strain curves had a curved s-shape. Method 1 for requiring the bulk modulus from the volumetric stress-strain diagram was to plot a trend line from the beginning of the hydrostatic phase until the stress-strain curve started to curve, as shown with the blue line in Figure 51.

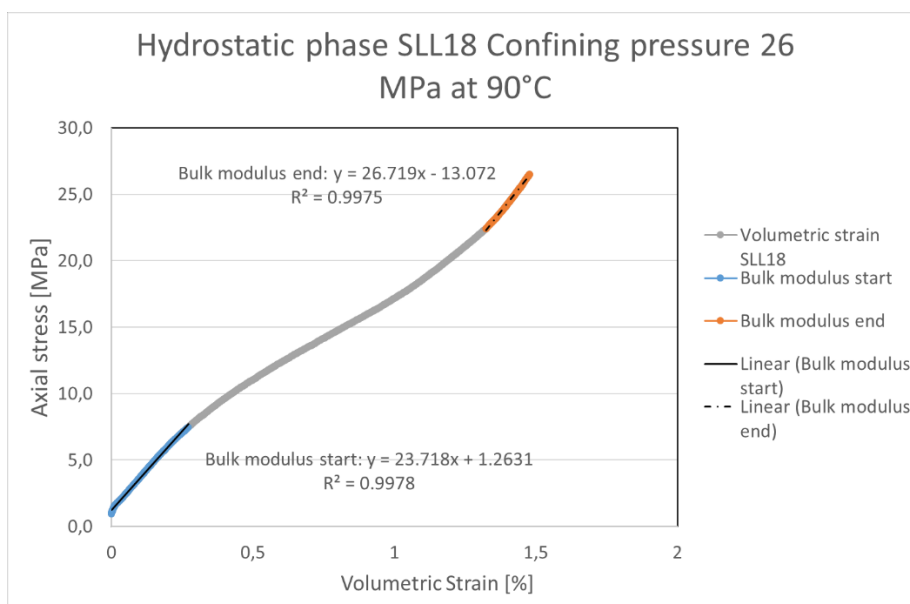


Figure 51 Example on how the bulk modulus was derived method 1 and 2, with sample SLL18 as an example

Method 2 was employed to determine the bulk modulus by using the end of the stress-strain curve. The slope of the curve was derived from this section to calculate the bulk modulus. This approach is represented by the orange line in Figure 51.

Method 3 involved utilizing the isotropic volumetric strain stress-strain curve to estimate the bulk modulus. Similar to method 1, the beginning of the test was utilized to derive the value of the bulk modulus. The orange line in Figure 52 illustrates this process.

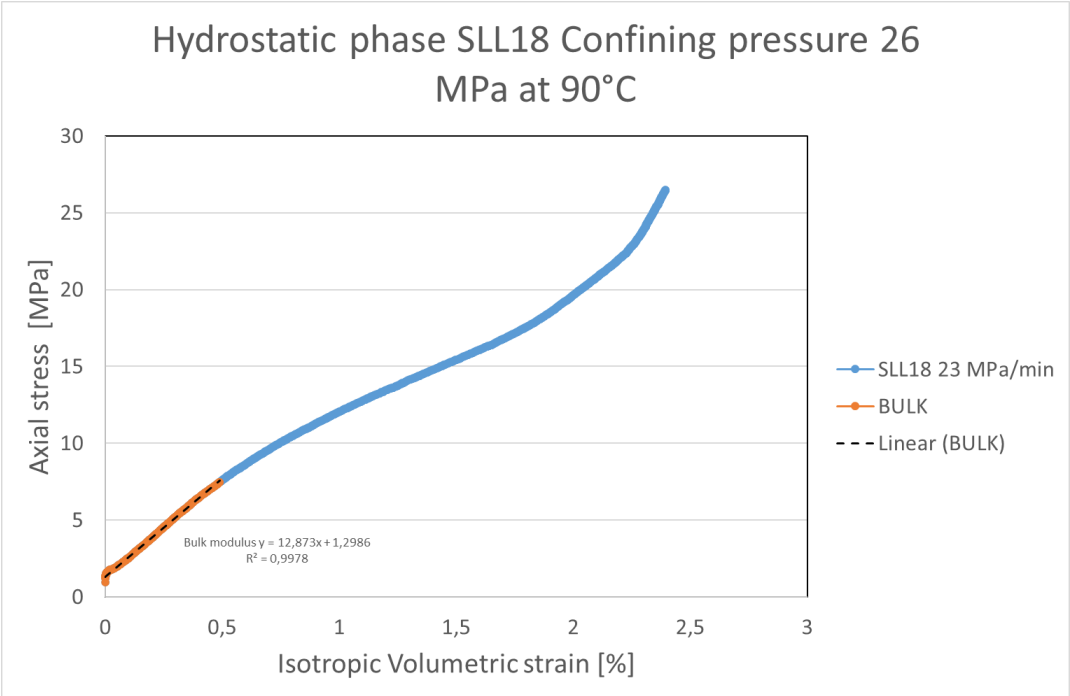


Figure 52 Example on how the bulk modulus was found for isotropic volumetric stress-strain diagram with sample SLL18 used as an example

3.3.2 Deviatoric loading phase

The axial and radial strain was calculated based on the axial and radial strain from the hydrostatic loading phase from equations 23-24. Figure 53 and Figure 54 demonstrates how the axial and radial strains were calculated in excel.

$$\epsilon_{Axial Dev} = \epsilon_{Axial HS} - \epsilon_{Axial HS \text{ at start of deviatoric}} [\%] \quad (23)$$

$$\epsilon_{Radial Dev} = \epsilon_{Radial HS} - \epsilon_{Radial HS \text{ at start of deviatoric}} [\%] \quad (24)$$

	J	K	L	M	N	O	P	Q	AE	AF	AG	AH	AI
1										Hydrostatic			Deviatoric
2	Rate(P3)	Temperatur	Diff.trykk	P_piston	P_conf	P_pore	Aksiell abs	Extensomete	Axial Stress	Axial Strain	Radial Strain	Volumetric Strain	Axial Strain
2991	0	89,62526	4,009324	0,810902	26,052	-0,011078	14,658139	38,606961	26,5104065	0,92949105	0,52561233	1,980715697	
2992	0	89,62526	4,009324	0,810902	26,052	-0,011078	14,658139	38,606961	26,5104065	0,92949105	0,52561233	1,980715697	0

Figure 53 How deviatoric axial strain was calculated in excel (sample SLL14 as an example)

	J	K	L	M	N	O	P	Q	AE	AF	AG	AH	AI	AJ
1										Hydrostatic			Deviatoric	
2	Rate(P3)	Temperatur	Diff.trykk	P_piston	P_conf	P_pore	Aksiell abs	Extensomete	Axial Stress	Axial Strain	Radial Strain	Volumetric Strain	Axial Strain	Radial Strain
2991	0	89,62526	4,009324	0,810902	26,052	-0,011078	14,658139	38,606961	26,5104065	0,92949105	0,52561233	1,980715697		
2992	0	89,62526	4,009324	0,810902	26,052	-0,011078	14,658139	38,606961	26,5104065	0,92949105	0,52561233	1,980715697	0	0

Figure 54 How deviatoric radial strain was calculated in excel (sample SLL14 as an example)

Young's modulus was determined by performing a linear analysis of the axial stress-strain curve, specifically by calculating the slope of the elastic region as seen in Figure 55, with the following formula 25

$$E = \frac{\sigma_{Axial}}{\epsilon_{Axial}} \quad (25)$$

Poisson's ratio was calculated from the start of the deviatoric loading phase to the end of the elastic region of deformation, with the following equation (26). An example of the calculations can be seen in Figure 56, where Poisson's ratio was calculated from the values of the axial and the radial strain. In other words, the calculation was performed from the start of the increase in the piston pump rate until the endpoint of Young's modulus, which corresponds to the point where the axial strain remained linear before the onset of plastic deformation.

$$\nu = - \frac{\epsilon_{Radial \text{ at end Young's } - \epsilon_{ini \text{ Radial Dev}}}}{\epsilon_{Axial \text{ at end Young's } - \epsilon_{ini \text{ Axial Dev}}}} = - \frac{\Delta \epsilon_{Radial Dev}}{\Delta \epsilon_{Axial Dev}} \quad (26)$$

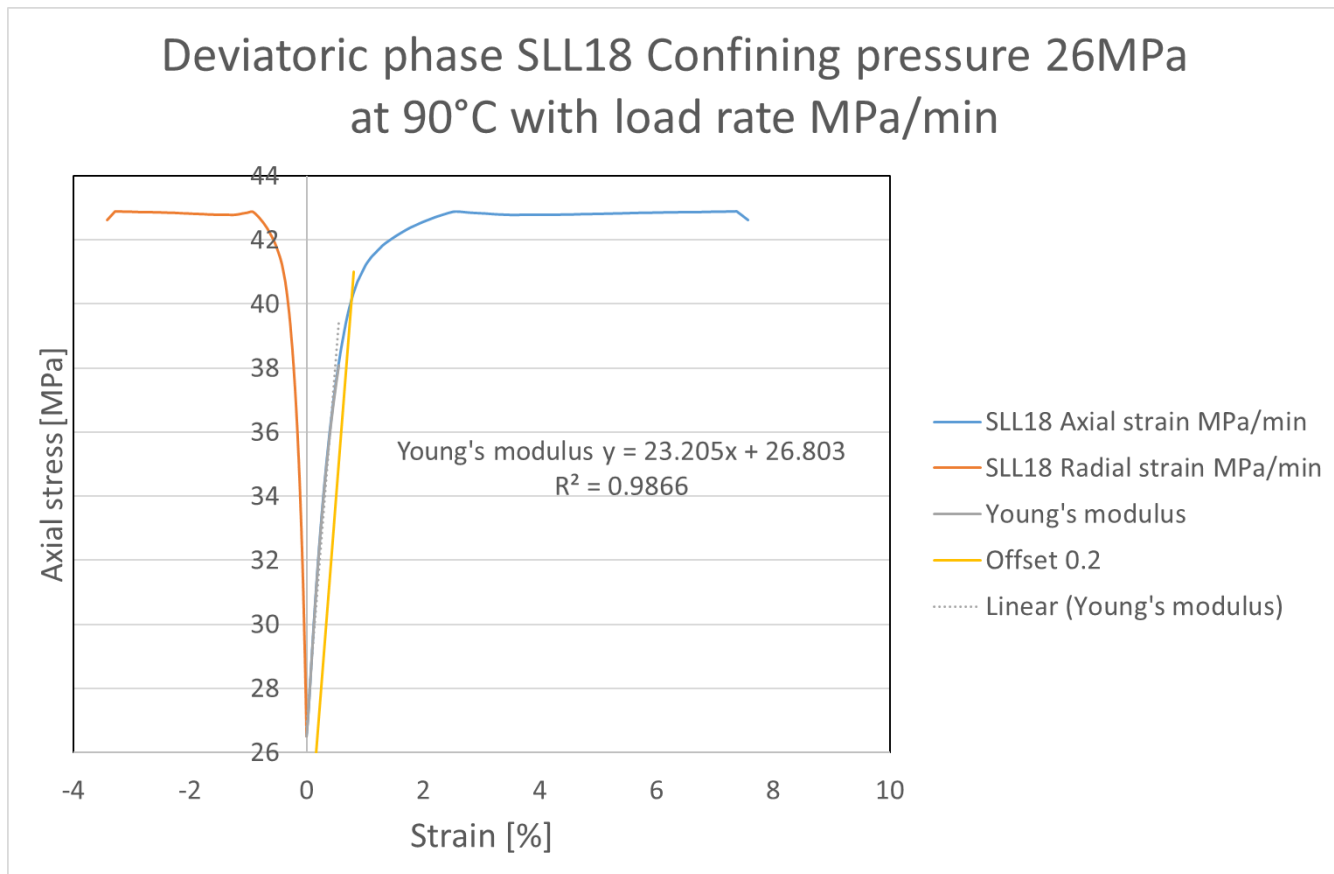


Figure 55 Deviator phase of sample 18 which depicts how the Young's modulus was found and how the compressive strength was estimated

Axial stress	Axial strain	Radial strain	Poisson's ratio
Start	0	0	0,41
End of Young's modulus	0,55	-0,22	

Figure 56 Example on how Poisson's ratio was calculated, with sample SLL18 used as an example

The piston load rate for samples tested with higher load rate than 12 MPa/min, was determined by plotting the recorded piston pressure against time. The slope of the linear part before the sample failed was used to find the actual pump rate. Figure 57 illustrates an example of a plot showing the piston load rate

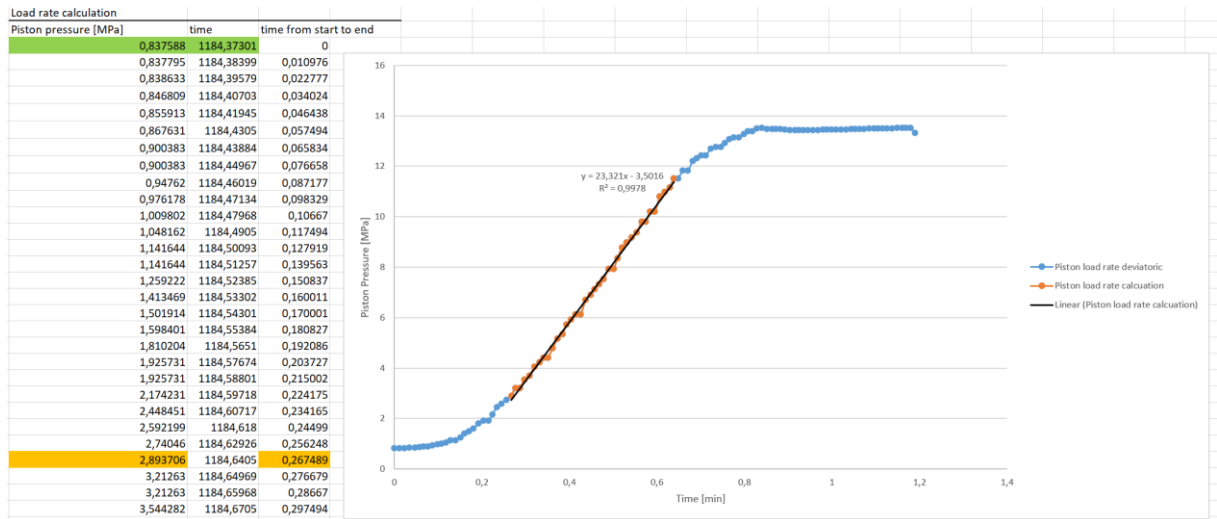


Figure 57 Example on how the actual piston load rate was estimated

The compressive strength of the sample was determined by identifying the point at which the 2% offset curve, with the same slope as the Young's modulus, intersected the axial stress-strain curve. The 2% offset line was plotted by using the linear trend line of the young's modulus and adding an additional 0.2 axial strain, as shown in equation 27, which is illustrated in Figure 58 and plotted in Figure 55 with the yellow line marked offset 0.2.

$$\text{Offset 2\% axial strain} = \frac{\sigma_{axial} - \sigma_{trend\ line\ E}}{E} + 0.2 [\%] \quad (27)$$

	A	B	C	D	E
1					
2		Off-set graph		0,2 %	
3					
4		Axial stress	Axial strain calculated		
5		26	0,165395389		
6		26,5	0,186942469	Young's modulus: $y = 17.077x + 26.829$	

Figure 58 Example on how the values for the offset graph was calculated for sample SLL18

4. Results and Discussion

The material properties for the JAW-B Geopolymer samples were tested in a triaxial cell through two loading phases: hydrostatic and deviatoric. In the hydrostatic loading phase, the bulk modulus of samples SLL1 to SLL20 was determined by increasing the confining pressure from 0.5 MPa to 8, 17.2 or 26 MPa. A constant load rate of 1.67 MPa/min was applied during this loading phase. Once the desired confining pressure was achieved, the samples was subjected to a deviatoric loading increase at different load rates. During this

loading increase the collected data utilized to determine Young's modulus, Poisson's ratio and compressive strength of the samples.

4.1 Hydrostatic phase

The results of the hydrostatic loading were presented in the relation to the applied confining pressure ranging from 8 MPa to 26 MPa. The determination of the bulk modulus involved using the slope of the calculated volumetric stress-strain diagram. However, it was observed that 7 out of the 18 samples had a curved shape, making it difficult to determine the bulk modulus by using method 1, described in chapter 3.3.1. Therefore, to obtain a more accurate value of the bulk modulus, method 2 and 3 described in chapter 3.3.1, was applied. These alternatives methods were utilized to overcome the challenges posed by the curved shapes of the stress-strain diagrams.

4.1.1 Confining pressure of 8 MPa

Six parallel geopolymer samples were tested with the confining pressure of 8MPa at a constant load rate of 1.67 MPa/min.

Table 7 Test results for hydrostatic phase for confining pressure 8 MPa at 90°C

Test plug	Confining pressure [MPa]	Axial strain Hydrostatic phase [%] end	Radial strain Hydrostatic phase [%] end	Bulk modulus [GPa] Method 1	Bulk modulus [GPa] Method 2	Bulk modulus [GPa] end Method 3
SLL8	8	0.24	0.09	1.85	-	1.04
SLL9	8	0.31	0.11	2.18	1.00	1.14
SLL10	8	0.29	0.16	1.21	-	0.84
SLL11	8	0.30	0.14	1.24	-	0.82
SLL12	8	0.36	0.21	0.92	-	0.67
SLL13	8	0.23	0.07	2.05	-	1.05
Average		0.29	0.13	1.58	1.00	0.92

Table 7 presents a summary of the outcomes obtained during the hydrostatic loading phase of 8 MPa of the JAW-B geopolymer samples. The focus of the analysis of the hydrostatic loading phase was primarily on the determination of the bulk modulus. The bulk modulus was one property derived from the hydrostatic loading and was derived by using three bulk modulus methods. Additionally, Table 7 also presents the axial and radial strains at the end of the hydrostatic loading.

A noticeable trend can be observed between the axial and the radial strains, wherein the axial strain surpassed the radial strain by a factor 1,7 (SLL12), factor 2 (SLL8, SLL10, SLL11) and to factor 3 (SLL9, SLL13) showed a similar relationship to the bulk modulus. Factor 1,7 provided the lowest bulk modulus of 0.92 GPa, for factor 2 range of 1.2-1.85 GPa and finally for factor 3 a bulk modulus range of 2.05-2.15 GPa.

Another noteworthy findings from Table 7, was the bulk modulus derived from method 3 had generally a lower value when compared to the other two methods. These observations suggest that the material behaviour of the geopolymer samples does not behave like an isotropic material.

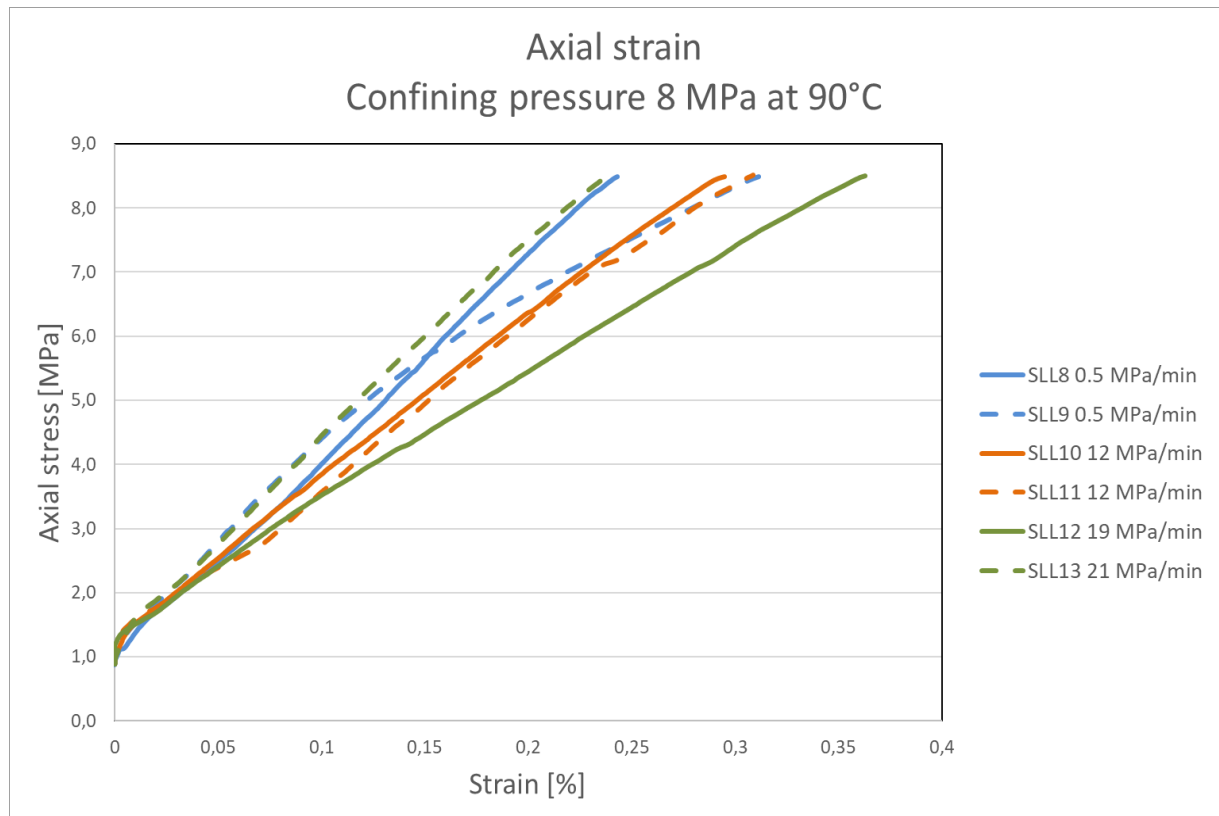


Figure 59 Axial strain for samples SLL8 to SLL13 with Confining pressure 8 MPa at an increase of 1.67 MPa/min

4.1.1.1 Observation of the axial stress-strain curve at confining pressure 8 MPa

Figure 59 depicts the axial stress-strain diagram for the samples subjected to a confining pressure of 8 MPa. The axial strain values ranged from 0.23% to 0.36%. Notably, the sample with 0.36% stood out as an outlier among the six tested samples.

In general, all samples exhibited a predominantly linear relationship between the axial stress and the axial strain. Except for two samples SLL9 (represented by the blue dotted line in Figure 59) and SLL11 (represented by the orange dotted line). These two samples deviated from the linear trend observed in the other samples. Suggesting these two samples have a different mechanical response to the increase in confining pressure from 0.5 to 8 MPa.

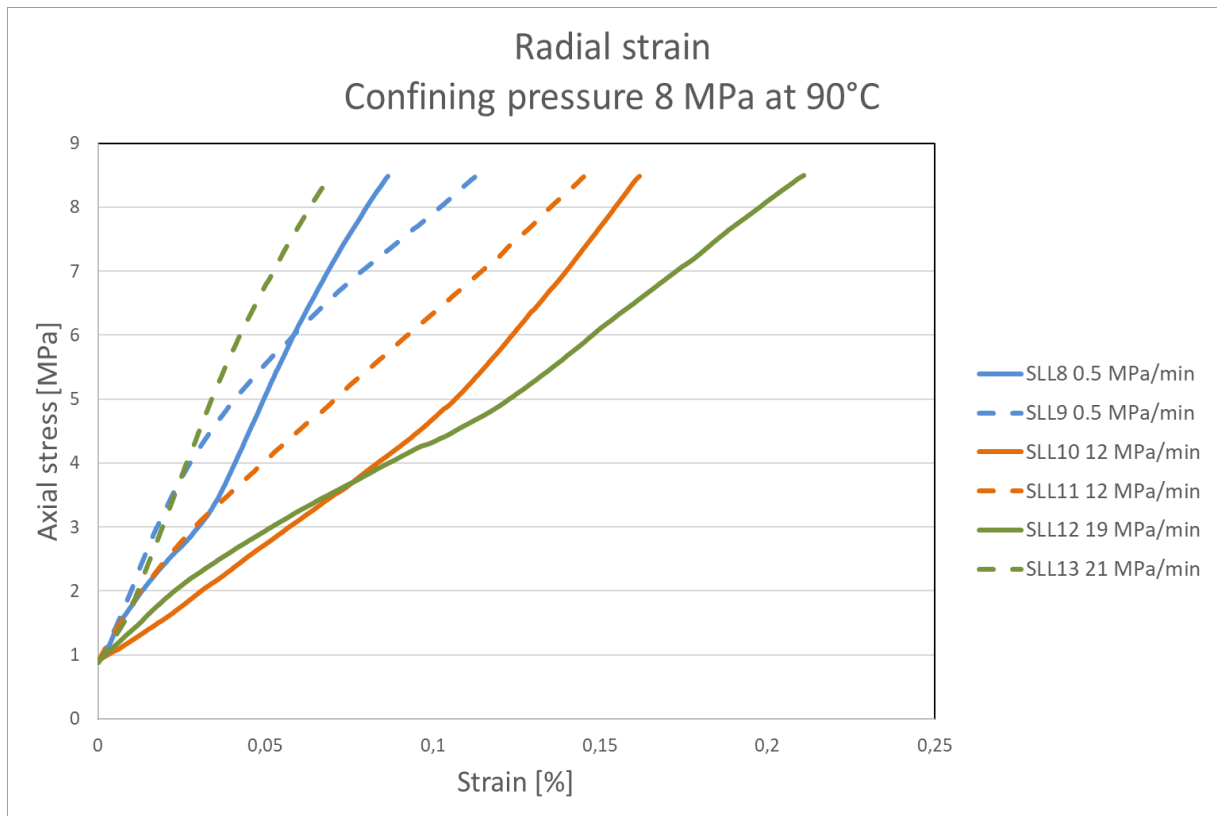


Figure 60 Radial strain for samples SLL18 to SLL13 with Confining pressure 8 MPa at an increase of 1.67 MPa/min

4.1.1.2 Observation of the radial strain axial strain at confining pressure 8 MPa

Figure 60 illustrates the relationship between the radial strain and the axial stress for the tested samples under a confining pressure of 8 MPa. Interestingly, the sample exhibiting the highest radial strain of 0.21% is also the same sample that stood out in Figure 59 as an outlier (SLL12, represented by the green line).

In contrast to axial stress-strain diagram in Figure 59, Figure 60 does not exhibit a clear trend among the six samples tested. The plots shapes and radial strain from Figure 60 Radial strain for samples SLL18 to SLL13 with Confining pressure 8 MPa at an increase of 1.67 MPa/min showed no clear trend among the six samples.

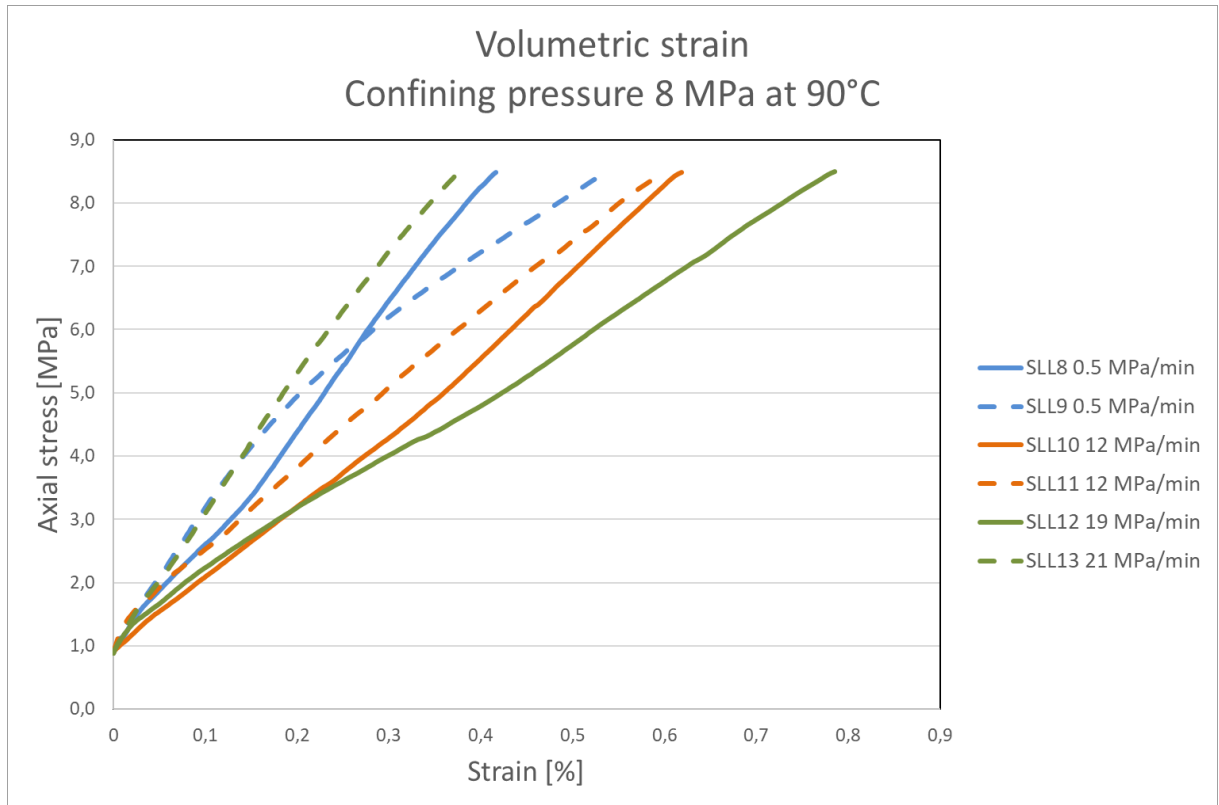


Figure 61 Volumetric strain for samples SLL8 to SLL13 with Confining pressure 8 MPa at an increase of 1.67 MPa/min

4.1.1.3 Observation of the volumetric strain axial strain at confining pressure 8 MPa

Figure 61 depicts the relationship between the volumetric strain and the axial stress for the tested samples under a confining pressure of 8 MPa. The volumetric strain ranged from 0.37% to 0.78%.

As with Figure 60, the relationship between the volumetric strain and axial strain varied among the samples. Some samples exhibit a more linear relationship between stress and strain (samples SLL11 and SLL13), while others displayed a more curved relationship between stress and strain (samples SLL8 and SLL9). However, the variations in Figure 61 were not as prevalent as in Figure 60.

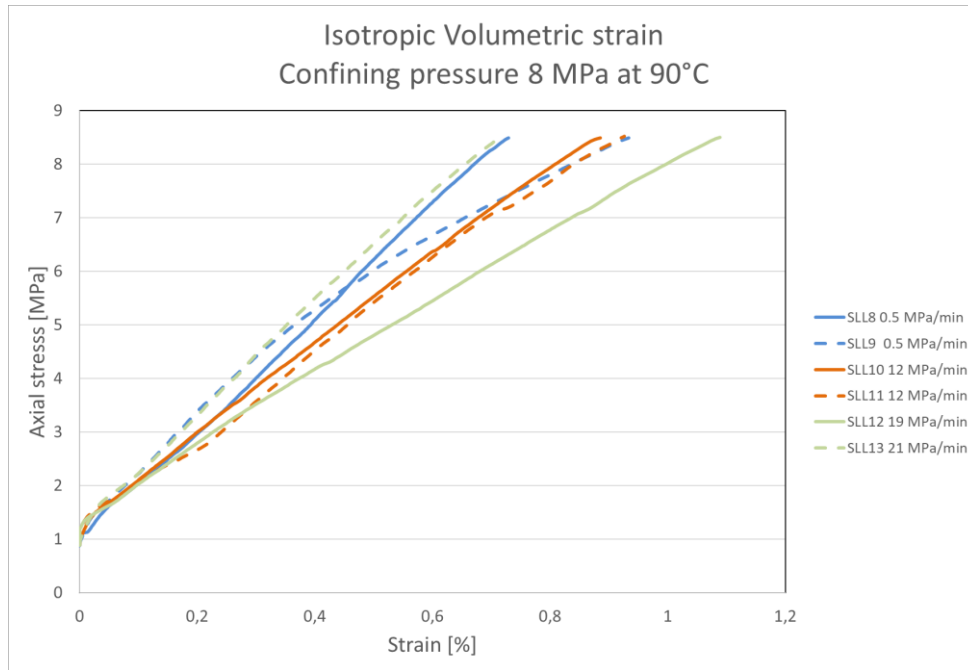


Figure 62 Isotropic volumetric strain based on axial strain only for samples SLL8 to SLL13 with Confining pressure 8 MPa at an increase of 1.67 MPa/min

Figure 62 isotropic volumetric strain based on the axial strain to confining pressure 8 MPa with an increase of 1.67 MPa/min. Figure 18 represents the relationship with the volumetric strain and axial stress, for the samples tested under a confining pressure of 8 MPa. With the assumption of the samples were of a homogenous material and had isotropic properties. Therefore, the volumetric strain-stress diagram mirrored the trends in Figure 61, but at a larger scale are approximately three times larger.

4.1.1.4 Discussion of the results of the hydrostatic phase at confining pressure 8 MPa

The samples tested at 8 MPa confining pressure were prepared using an optimized test sample preparation method. Ensuring the absence of surface damage or silicone grease within the sample, as shown in Figure 76. This change in sample preparation reflected in the axial strain-stress curve in Figure 60, in contrast to the curves presented in Figure 66 the samples tested at 17.2 MPa confining pressure. Which showed a more curved plots, this behaviour is discussed in Chapter 4.1.2.

To gain a comprehensive understanding of the behaviour of the JAW-B geopolymers during hydrostatic loading up to 8 MPa, all the tested samples was plotted in a single plot. As shown in Figure 63. The outliers in Figure 63 corresponds to the axial strain range between

0.12% and 0.45%. Approximately 11 of the samples clustered within the range of 0.23% to 0.36% axial strain. This aligns with the range of Figure 60.

The radial strain exhibited a range of 0.05% to 0.22%, as shown in Figure 64. A cluster of samples can be observed the interval 0.05% to 0.14%. In contrast to the axial strain, the radial strain curves appear more curved. This curvature in the majority of the samples, may be attributed to the sensitivity of the measurement equipment for circumference.

A consistent trend observed in all the samples is that the axial strain exceeds the radial strain. This trend persists across the entire dataset displayed in Figure 63 and Figure 64. Notably, the sample with the lowest radial strain (SLL16 represented with the magenta line Figure 63) also exhibits the second lowest axial strain. Interestingly, the sample with the largest axial strain demonstrates the third largest radial strain.

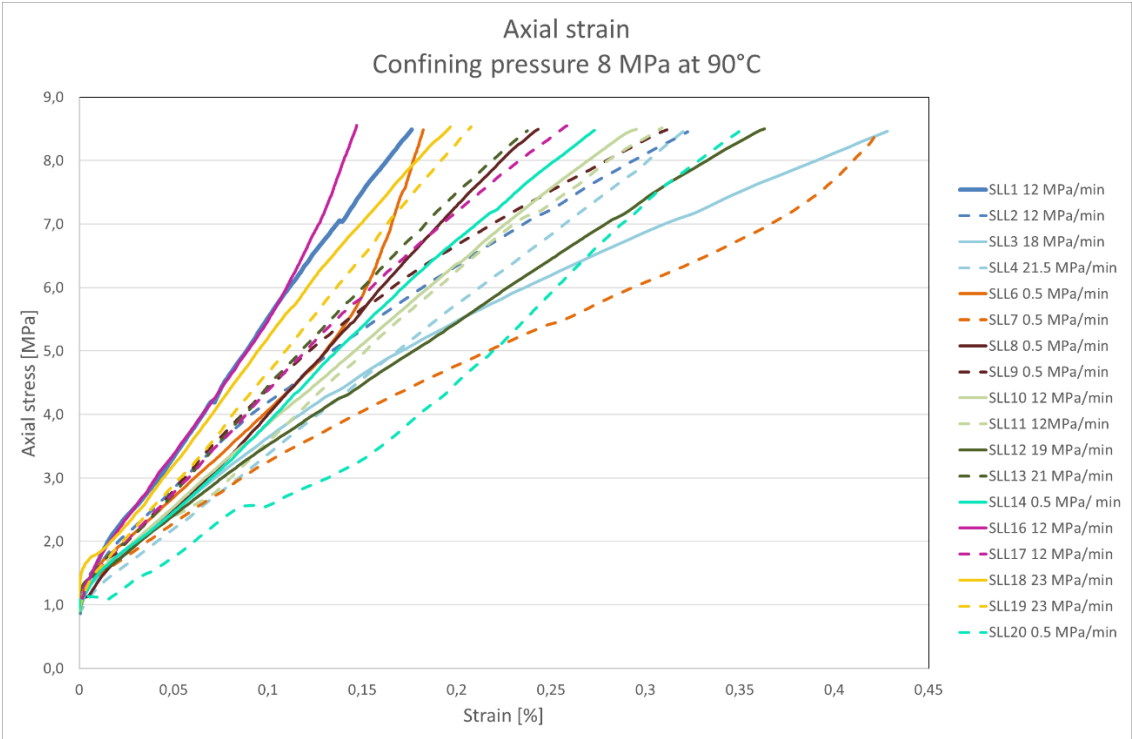


Figure 63 Axial strain for all samples up to Confining pressure of 8 MPa at an increase of 1.67 MPa/min

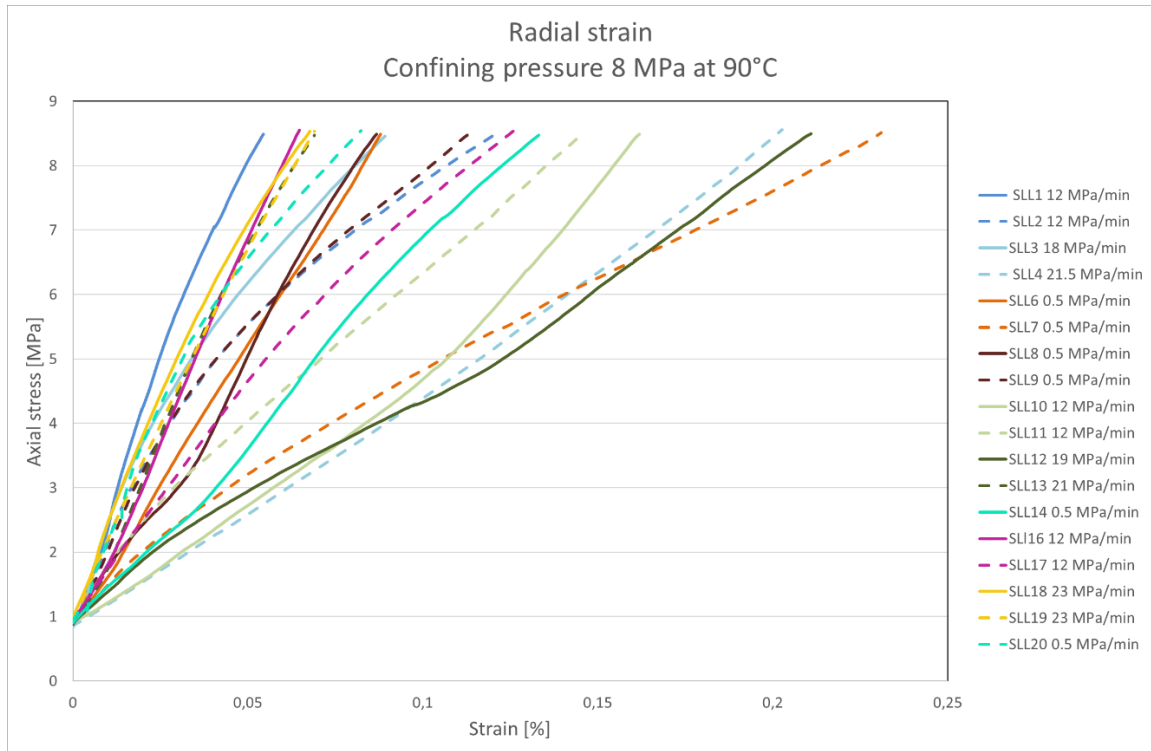


Figure 64 Radial strain for all samples up to Confining pressure of 8 MPa at an increase of 1.67 MPa/min

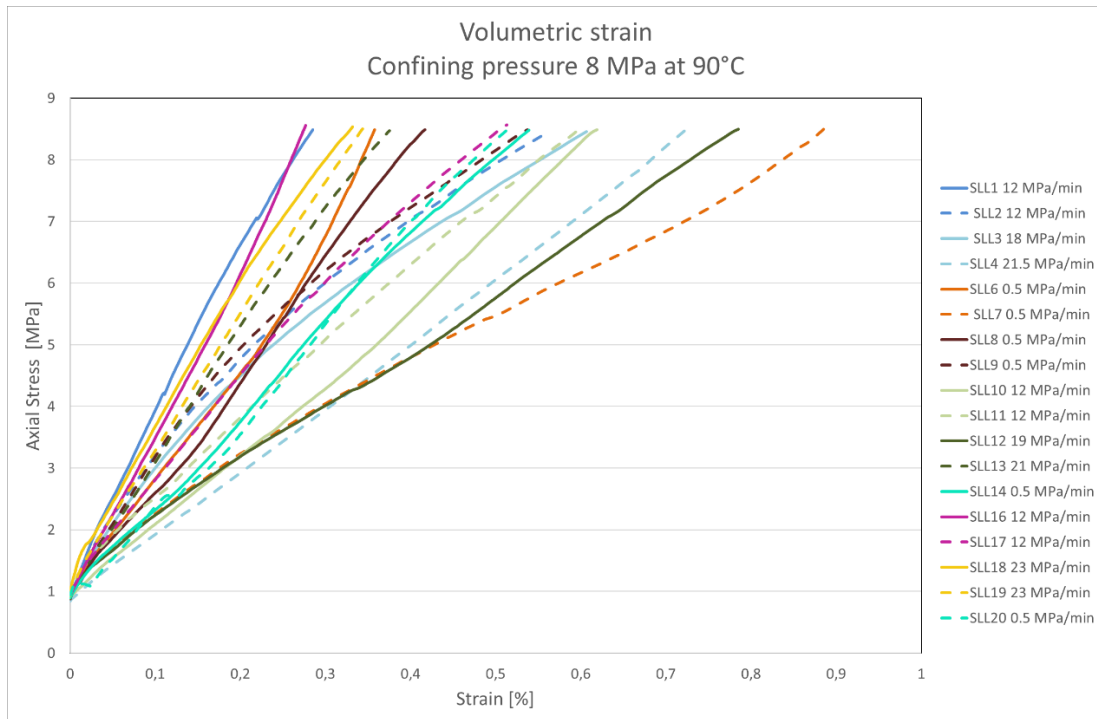


Figure 65 Radial strain for all samples up to Confining pressure of 8 MPa at an increase of 1.67 MPa/min

Similar to Figure 61, Figure 65 follows a similar trend in the relationship between the volumetric strain and the axial strain. The volumetric strain exhibited a range 0.27% to

0.88%. Two distinct clusters were observed, one in the range of 0.27% to 0.37% and another in the range of 0.51% to 0.61%.

Upon examining the Figure 63, Figure 64 and Figure 65 it is evident that there is clear trend in the volumetric strain behaviour among the different test samples. This lack of clear trends could be attributed to potential errors during sample mixing, curing and preparation, or it could be influenced by the sensitivity of the measuring equipment utilized. It is important to note that two samples failed the tests due to the Extensometer being out of range. Which could have also contributed to the variability in the observed strain values.

4.1.2 Confining pressure 17.2 MPa

Table 8 Test results for hydrostatic phase for confining pressure 17.2 MPa at 90°C

Test plug	Confining pressure [MPa]	Axial strain [%] Hydrostatic phase end	Radial strain [%] Hydrostatic phase end	Bulk modulus [GPa] Method 1	Bulk modulus [GPa] Method 2	Bulk modulus [GPa] Method 3
SLL1	17.2	0.56	0.20	2.91	-	0.63
SLL2	17.2	0.73	0.37	2.21	1.51	0.62
SLL3	17.2	0.75	0.24	1.73	2.04	0.51
SLL4	17.2	0.78	0.38	1.10	-	0.71
SLL6	17.2	0.28	0.16	1.82	3.53	2.95
SLL7	17.2	0.69	0.28	0.81	-	1.15
Average		0.63	0.27	1.77	2.36	1.09

Test plug	Confining pressure [MPa]	Axial strain [%] Hydrostatic phase end	Radial strain [%] Hydrostatic phase end	Bulk modulus [GPa] Method 1	Bulk modulus [GPa] Method 2	Bulk modulus [GPa] Method 3
SLL1	17.2	0.56	0.20	2.91	-	0.63
SLL2	17.2	0.73	0.37	2.21	1.51	0.62
SLL3	17.2	0.75	0.24	1.73	2.04	0.51
SLL4	17.2	0.78	0.38	1.10	-	0.71
SLL6	17.2	0.28	0.16	1.82	3.53	2.95

SLL7	17.2	0.69	0.28	0.81	-	1.15
Average		0.63	0.27	1.77	2.36	1.09

Table 8 provides a summary of the results obtained during the hydrostatic loading of JAW-B geopolymer samples at 17.2 MPa confining pressure. Similar to the tests conducted at 8 MPa confining pressure, the focus of the analysis was on the bulk modulus, the axial and radial.

Continuing the trend observed in

Table 8, the axial strain was consistently larger than the radial strain for all the samples

Test plug	Confining pressure [MPa]	Axial strain [%] Hydrostatic phase end	Radial strain [%] Hydrostatic phase end	Bulk modulus [GPa] Method 1	Bulk modulus [GPa] Method 2	Bulk modulus [GPa] Method 3
SLL1	17.2	0.56	0.20	2.91	-	0.63
SLL2	17.2	0.73	0.37	2.21	1.51	0.62
SLL3	17.2	0.75	0.24	1.73	2.04	0.51
SLL4	17.2	0.78	0.38	1.10	-	0.71
SLL6	17.2	0.28	0.16	1.82	3.53	2.95
SLL7	17.2	0.69	0.28	0.81	-	1.15
Average		0.63	0.27	1.77	2.36	1.09

tested at 17.2 MPa. One sample stood out as an outlier of the samples. This was sample SLL6 with 0.28% axial strain and 0.16% radial strain, this represents a value which compared to the rest of the samples is half or more (0.56% to 0.78% axial strain and 0.28% to 0.38%).

One significant observation is the wide range of value for the bulk modulus, which varied from 0.81 to 3.53 GPa. This substantial variation could be attributed to the sample from SLL1 to SLL7 were not samples made under the optimized procedure.

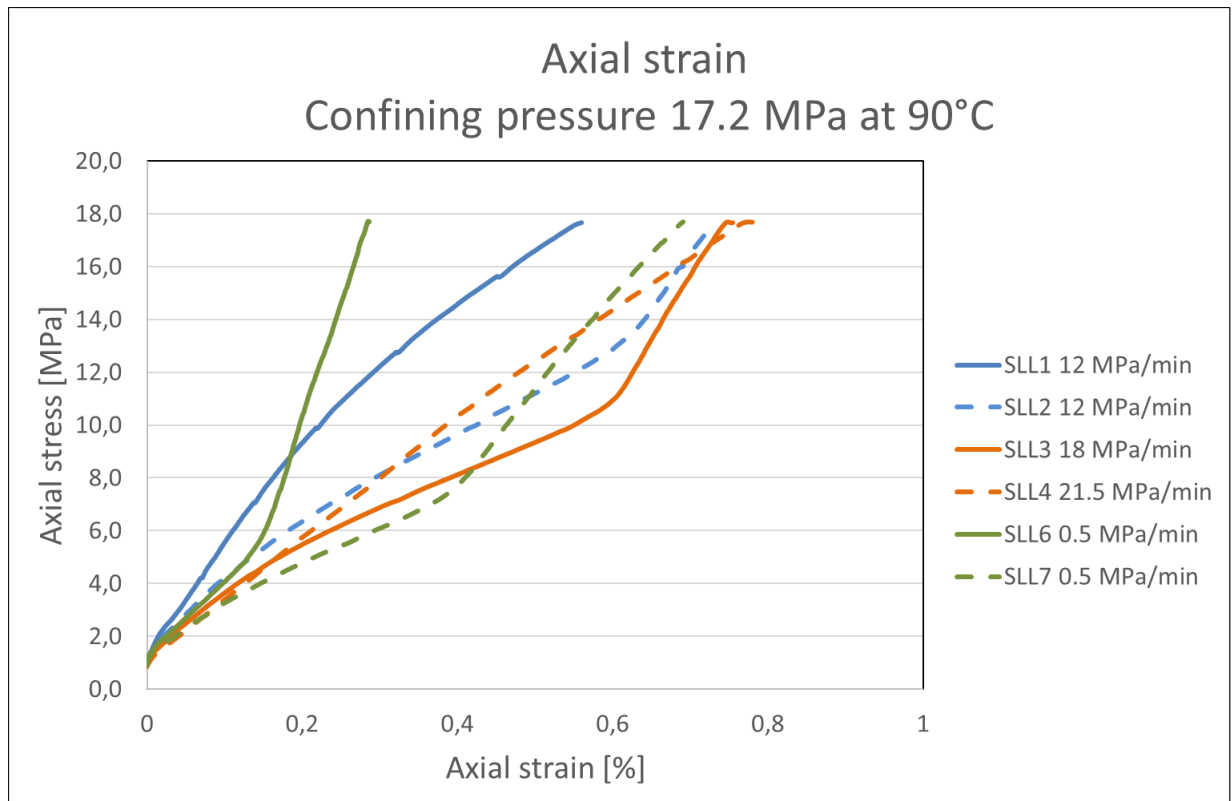


Figure 66 Axial strain for samples SLL1 to SLL7 with confining pressure of 17.2 MPa at an increase of 1.67 MPa/min

4.1.2.1 Observation of axial stress against axial, radial and volumetric strain curve at confining pressure 17.2 MPa

Figure 66 exhibits the relationship between of the axial strains against the axial stress at a confining pressure of 17.2 MPa. While Figure 67 illustrates the relationship between the axial stress against the radial stress. Both figures reveal a similarity in behaviour between axial and radial strains. For instance, sample SLL6, which exhibited the lowest axial strain of 0.28% and the lowest radial strain of 0.16%, demonstrates a mirrored trend in the shape of the curves. This suggests a correlation between the strain exhibited in one direction and the strain observed in the opposite direction within the cores. In simpler terms, cores that display higher or lower strain in one direction tend to show a similar trend of higher or lower strain in the other direction.

However, unlike the clear trends observed in Figure 59 for axial strain, there is no distinct pattern evident among the six samples in Figure 66. As mentioned in chapter 4.1.1.4 this lack of repeatability can be attributed to non-optimized sample preparation. The first test sample

SLL1, experienced a step-like loading due to suboptimal settings for the confining pump. This issue was subsequently addressed.

Sample SLL7, represented by the green dotted line, encountered a problem with the extensometer reading went out of range around 10.6 MPa confining pressure. Therefore, in Figure 67, an assumption was made and included to complete the representation of the data.

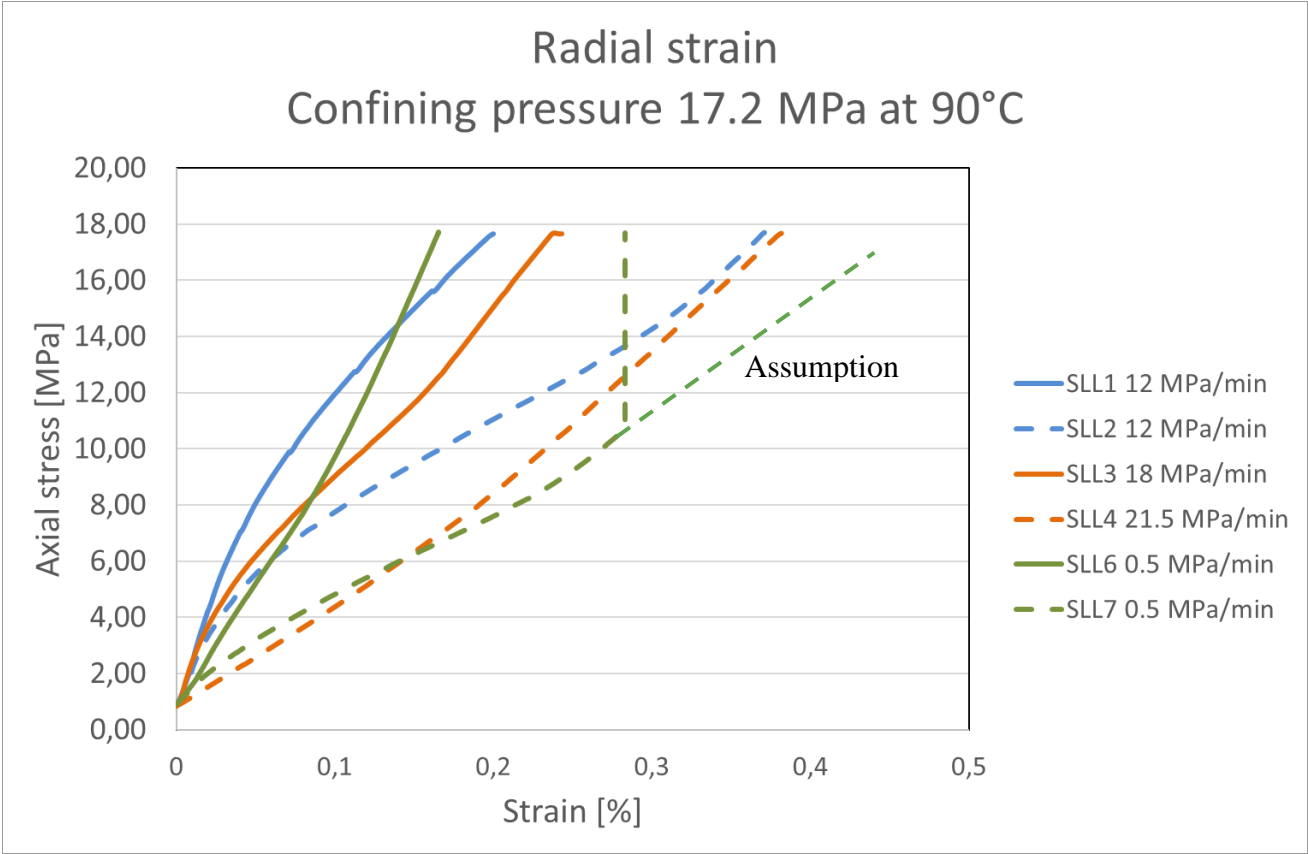


Figure 67 Radial strain for samples SLL1 to SLL7 with confining pressure of 17.2 MPa at an increase of 1.67 MPa/min

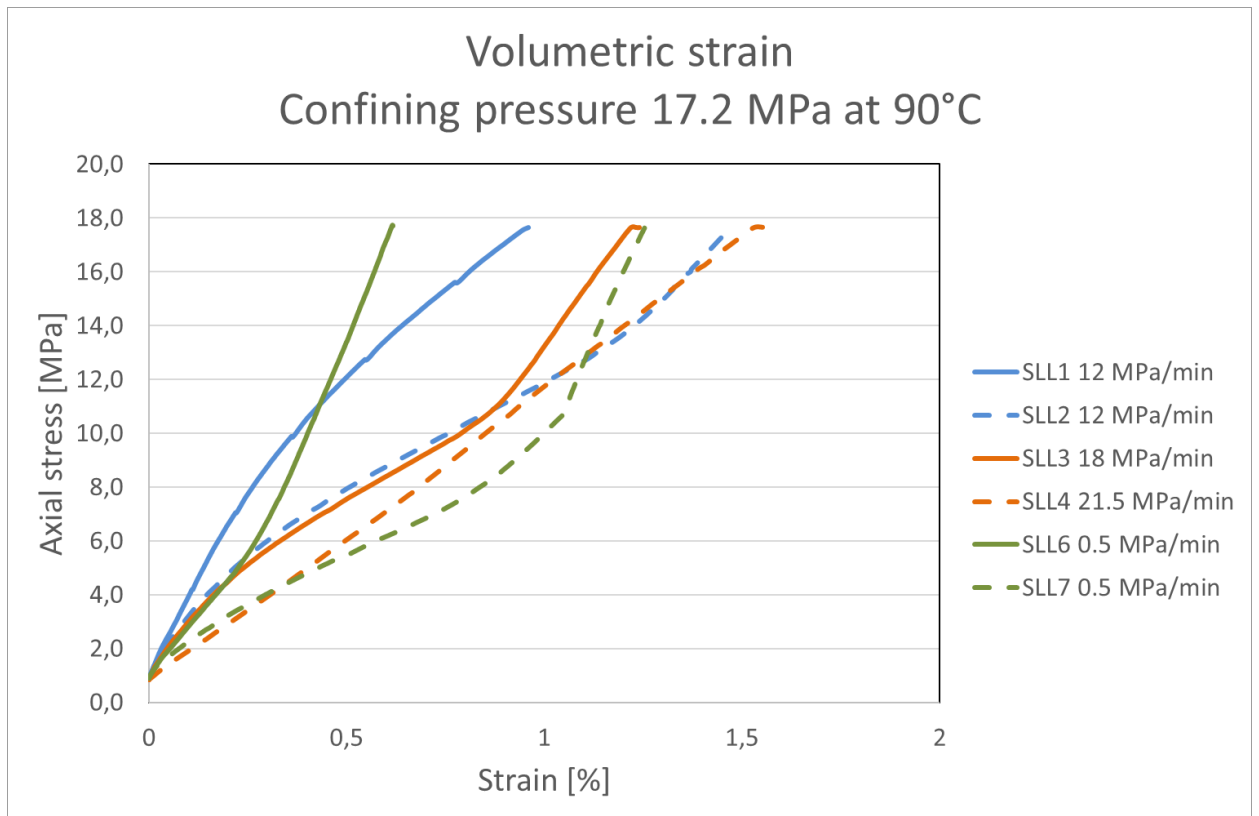


Figure 68 Volumetric strain for samples SLL1 to SLL7 with confining pressure of 17.2 MPa at an increase of 1.67 MPa/min

Figure 68 depicts the relationship between the volumetric strain and the axial stress for the tested samples under a confining pressure of 17.2 MPa. The volumetric strain ranged from 0.61% to 1.55%. Similar to the observations in Figure 66 and Figure 67 the axial and radial strains in, there is no distinct trend of the volumetric strain among the samples. However, it is worth noting that samples SLL2 and SLL4, represented by the blue and orange dotted curves respectively, exhibit the closest repeatability among the six samples tested.

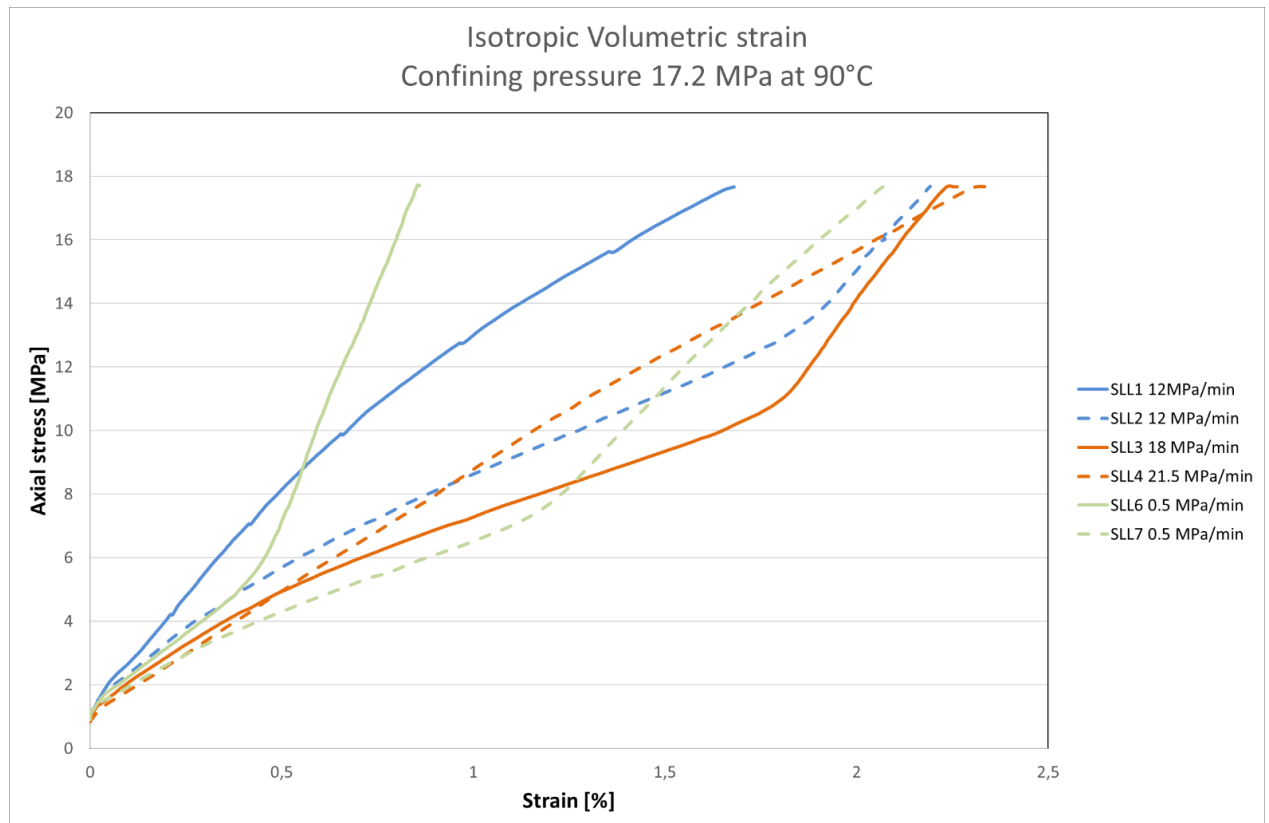


Figure 69 Isotropic volumetric strain for samples SLL1 to SLL7 with confining pressure of 17.2 MPa at an increase of 1.67 MPa/min

As for Figure 69, like Figure 62 this volumetric strain assumes the samples being homogenous. Which from the curved shaped plots in Figure 69, is not the case.

4.1.2.1 Discussion of the result of the hydrostatic phase with confining pressure of 17.2 MPa

In Figure 66, Figure 67, and Figure 68, no clear trends were observed among the samples SLL1 to SLL7. However, the axial and radial strains exhibited similar shapes, which indicates the relationship between the two strains. This implies that cores exhibiting higher or lower strain in one direction typically exhibit a corresponding trend of higher or lower strain in the opposite direction. In other words, a strong core demonstrates strength in all directions, while a weak core experiences greater strain in all directions. It is important to note that this trend is not valid for all cores, but it is generally observed.

Therefore, the lack of repeatability in the results can be attributed to the non-optimized sample preparation. As the samples got stuck in the moulds during the removal process, resulting in damage and the formation of bubbles on the sample surfaces, as seen in the Figure 76.

To assess whether the repeatability improved after implementing a change in the procedure, the samples from SLL14 to SLL20 were plotted together in Figure 70, Figure 71, and Figure 72, along with the samples tested at a confining pressure of 17.2 MPa. From Figure 70, Figure 71, and Figure 72, there is a significant improvement in repeatability among the samples SLL14 to SLL20. Figure 70 display that samples SLL14 and SLL17 to SLL19 exhibit axial strains ranging from 0.57% to 0.74% with a similar shape to the stress-strain curve. Similarly, in Figure 71, samples SLL14, SLL18, and SLL19 display radial strains ranging from 0.18% to 0.25%.

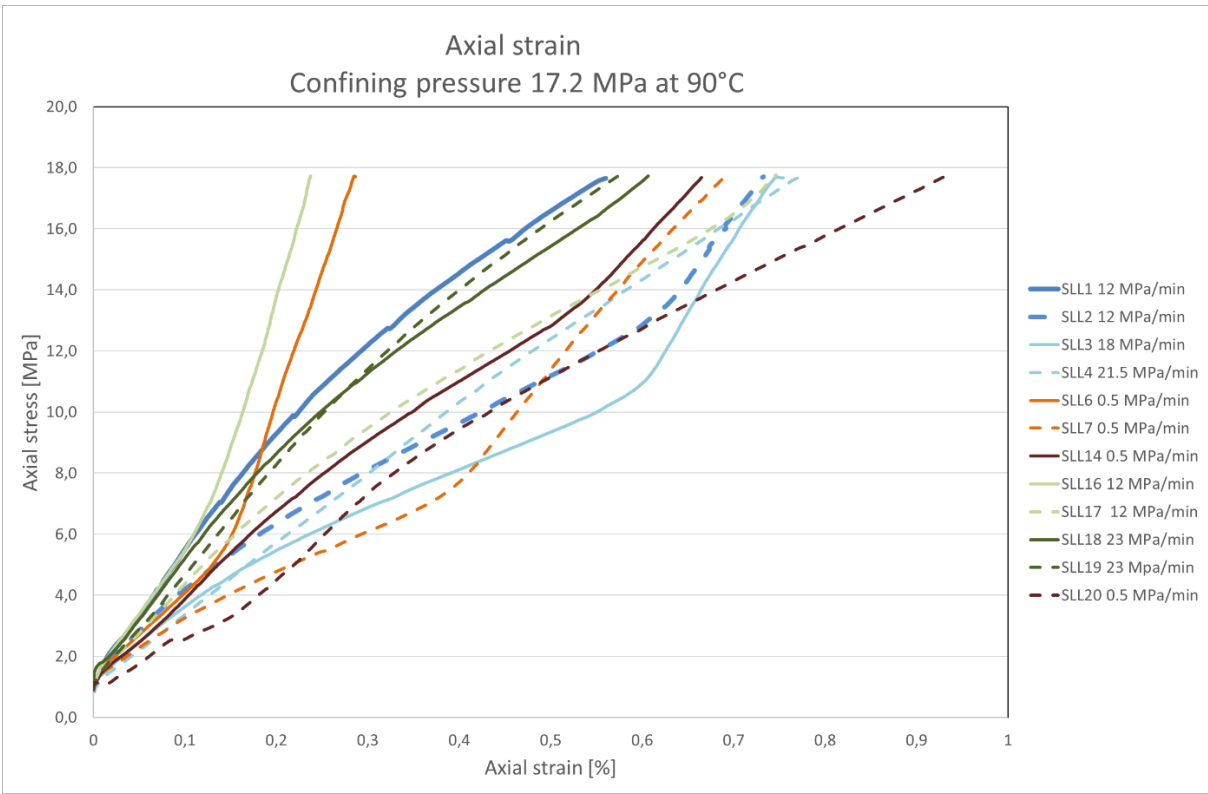


Figure 70 Axial strain for all samples up to Confining pressure of 17.2 MPa at an increase of 1.67 MPa/min

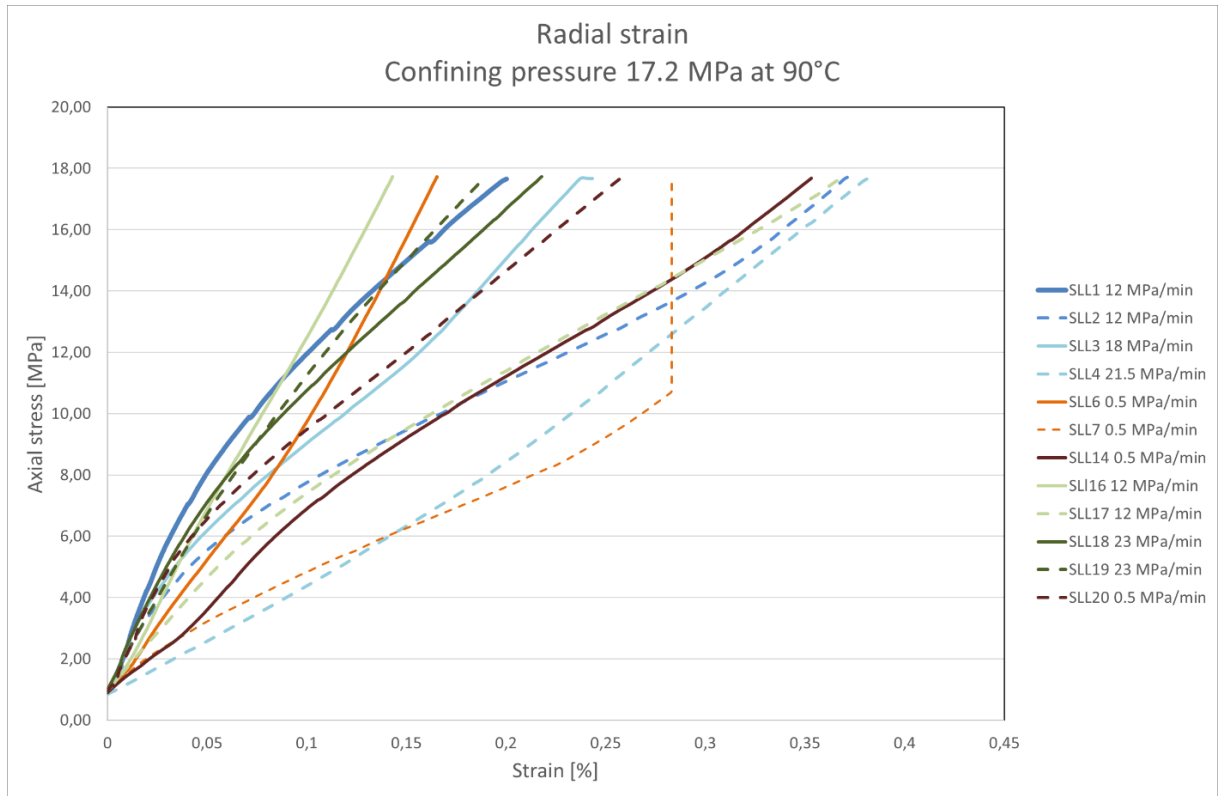


Figure 71 Radial strain for all samples up to Confining pressure of 17.2 MPa at an increase of 1.67 MPa/min

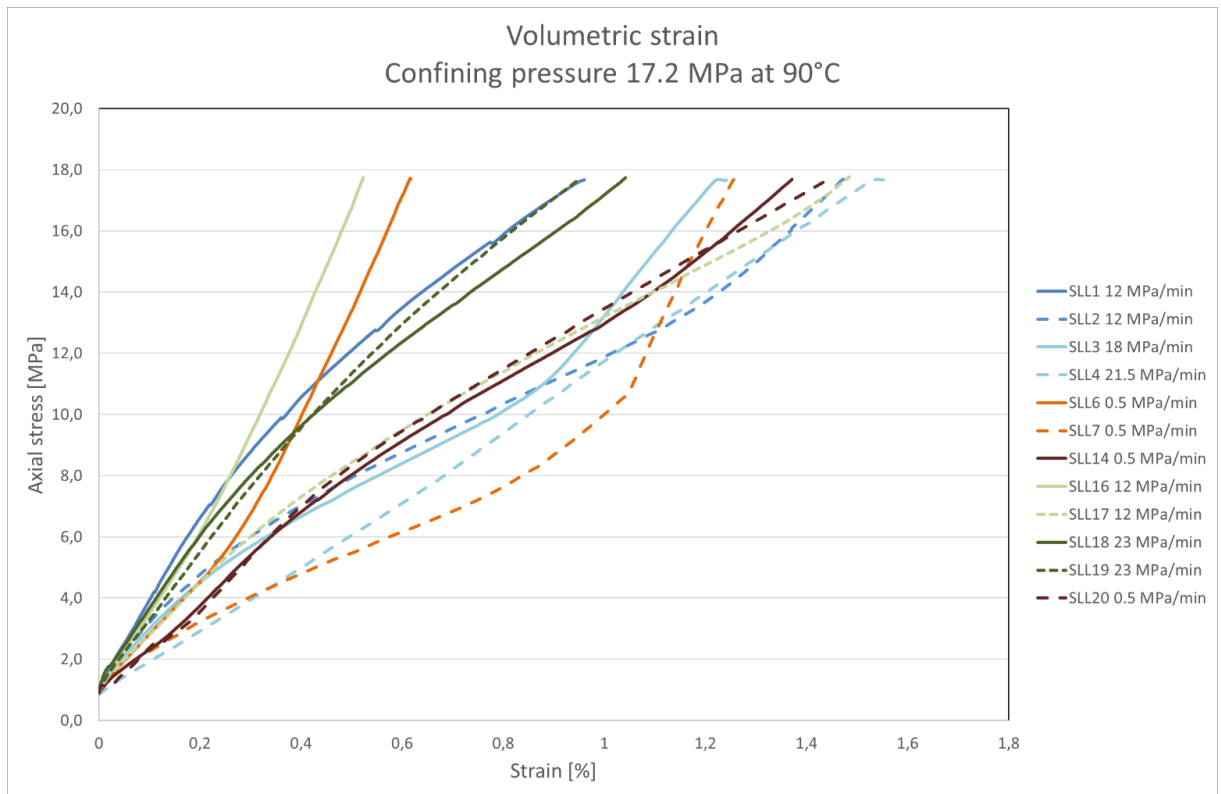


Figure 72 Volumetric strain for all samples up to Confining pressure of 17.2 MPa at an increase of 1.67 MPa/min

In Figure 72, it is evident that the repeatability of the samples from SLL14 to SLL20 is significantly better than that of the samples from SLL1 to SLL7. Notably, two samples from the two different sets of samples exhibited a similar shape in Figure 70, Figure 71, and Figure 72. These samples are SLL6, represented by the orange line, and SLL16, represented by the light green lines. Both of these samples demonstrated a relative stronger response to withstand the deformation sustained during hydrostatic loading phase.

The strains observed in these samples were lower compared to the other samples. The axial strains ranged from 0.23% to 0.28%, radial strain ranged from 0.14% to 0.16% and volumetric strain ranged from 0.51% to 0.61%. These values were approximately half or less than the axial and radial strains observed in the other samples.

4.1.3 Confining pressure 26 MPa

Table 9 Test results for hydrostatic phase for confining pressure 26 MPa at 90°C

Test plug	Confining pressure [MPa]	Axial strain [%] Hydrostatic phase end	Radial strain [%] Hydrostatic phase end	Bulk modulus [GPa] Method 1	Bulk modulus [GPa] Method 2	Bulk modulus [GPa] Method 3
SLL14	26	0.92	0.51	1.10	-	1.05
SLL20	26	1.26	0.39	0.96 (middle)	1.69	0.51
SLL16	26	0.33	0.20	3.51	-	3.22
SLL17	26	1.01	0.51	1.46	1.58	1.07
SLL18	26	0.79	0.33	2.37	2.67	1.28
SLL19	26	0.99	0.32	2.15	1.29	1.19
Average		0.88	0.38	1.92	1.81	1.38

Table 9 presents a summary of the results obtained from the hydrostatic loading of JAW-B geopolymer samples at 26 MPa confining pressure. The loading rate during the hydrostatic phase was of 1.67 MPa/min. Similar to the tests conducted at 8 MPa and 17.2 confining pressure, the focus of the analysis was on the bulk modulus, the axial and radial of the geopolymer samples.

Consistent with the previous confining pressures, the axial strain was consistently larger than the radial strain for all the samples tested at 26 MPa. Among the samples, SLL16 stood out as an outlier, with an axial strain of 0.33% and a radial 0.20%. This value represents a significant difference compared to the rest of the samples. Which exhibited a range 0.92% to 1.26% axial strain and 0.20% to 3.51%. One significant observation is the wide range of value for the bulk modulus, which varied from 0.96 to 3.51 GPa.

Samples 14 and 18, were left to cure for an extra 24 hours in ambient condition, submerged in water. Therefore, the slight difference between SLL14 and SLL20, with SLL14 having the higher bulk modulus, ref. Table 9.

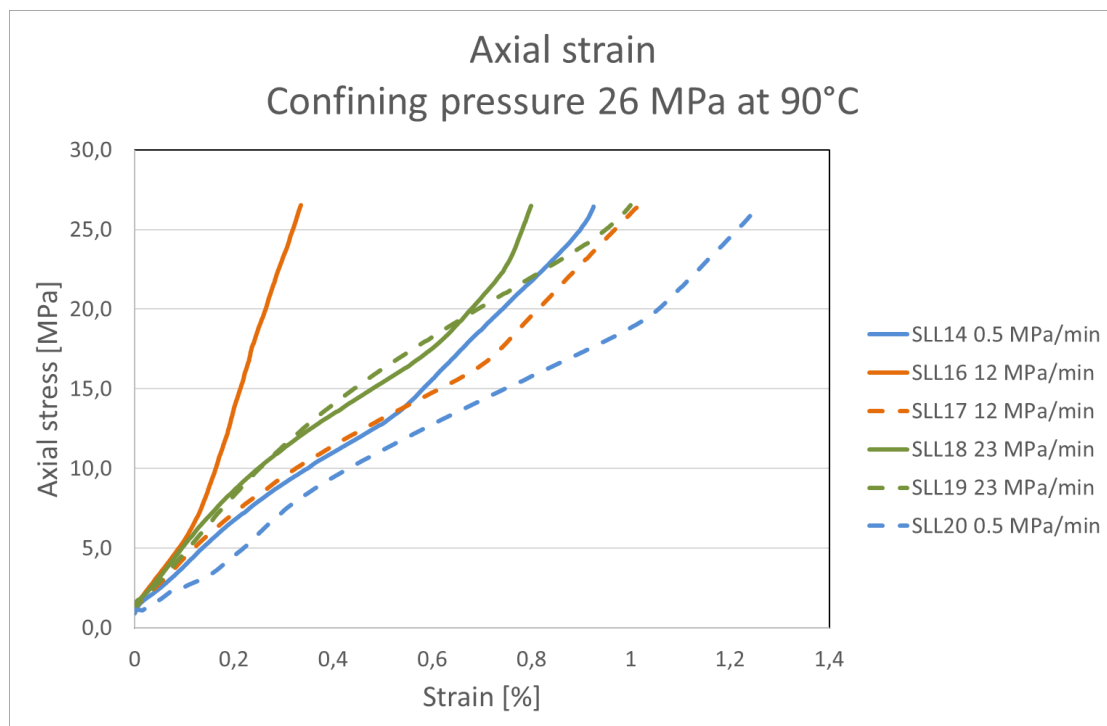


Figure 73 Axial strain for samples SLL14 to SLL20 with confining pressure of 26 MPa at an increase of 1.67 MPa/min

4.1.3.1 Observation of the result of the hydrostatic phase with confining pressure of 26 MPa stress-strain diagrams

Figure 73 illustrates the relationship between the axial stress and axial strain of the geopolymer samples tested at a confining pressure of 26 MPa. The axial stress-strain curves exhibit two outliers, SLL16, represented by the orange line, with an axial strain of 0.33%, and SLL20, represented by the dotted blue line, with an axial strain of 1.26%.

Of particular interest is sample SLL16, which displays a distinct stress-strain behaviour compared to the other samples. At around 6 MPa confining pressure, this sample becomes stiff and displays a more linear response to the increasing pressure. This is evident in its high bulk modulus value of 3.51 GPa, the highest overall value of the samples. On the other hand, sample SLL17, represented by the orange dotted line, becomes stiffer after 15 MPa, while SLL14, represented by the blue line, exhibit stiffness after 14 MPa.

Overall, Figure 73 demonstrates a better repeatability compared to Figure 66. Indicating improvement in consistency in the results from the samples tested at 26 MPa confining pressure.

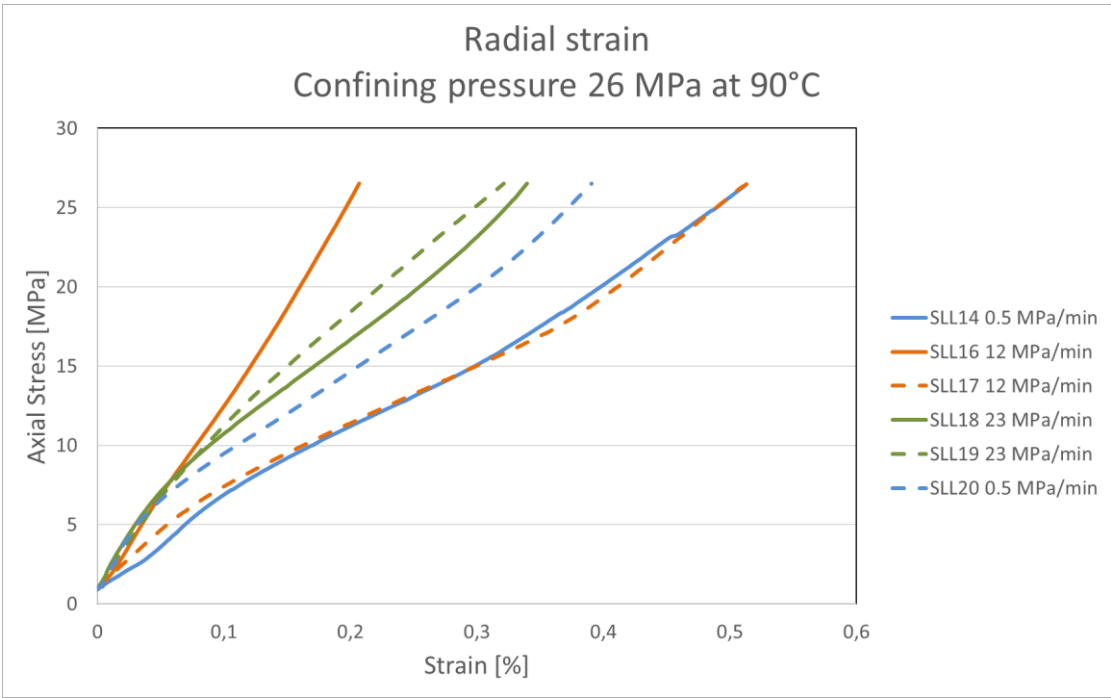


Figure 74 Radial strain for samples SLL14 to SLL20 with confining pressure of 26 MPa at an increase of 1.67 MPa/min

Figure 74 illustrates the relationship between the axial stress and radial strain of samples SLL14 to SLL20 tested at a confining pressure of 26 MPa. Interestingly, Figure 74 the radial strain of both SLL14 and SLL17 exhibited similar strain behaviour, with nearly equal values of 0.32% and 0.33%. While sample SLL16 had the lowest radial strain, and it had the most linear shape out of the six samples of 0.20%. The axial and radial strain curves mirrored each other as in Figure 66 and Figure 67. In contrast, SLL16 displayed the lowest radial strain

amongst the six samples and demonstrated a more linear relationship between stress and strain.

This observation highlights the similarity in behaviour between axial and radial strains, as observed in Figure 66 and Figure 67. The axial and radial strain curves exhibit a mirrored relationship, indicating a consistent pattern across the tested samples.

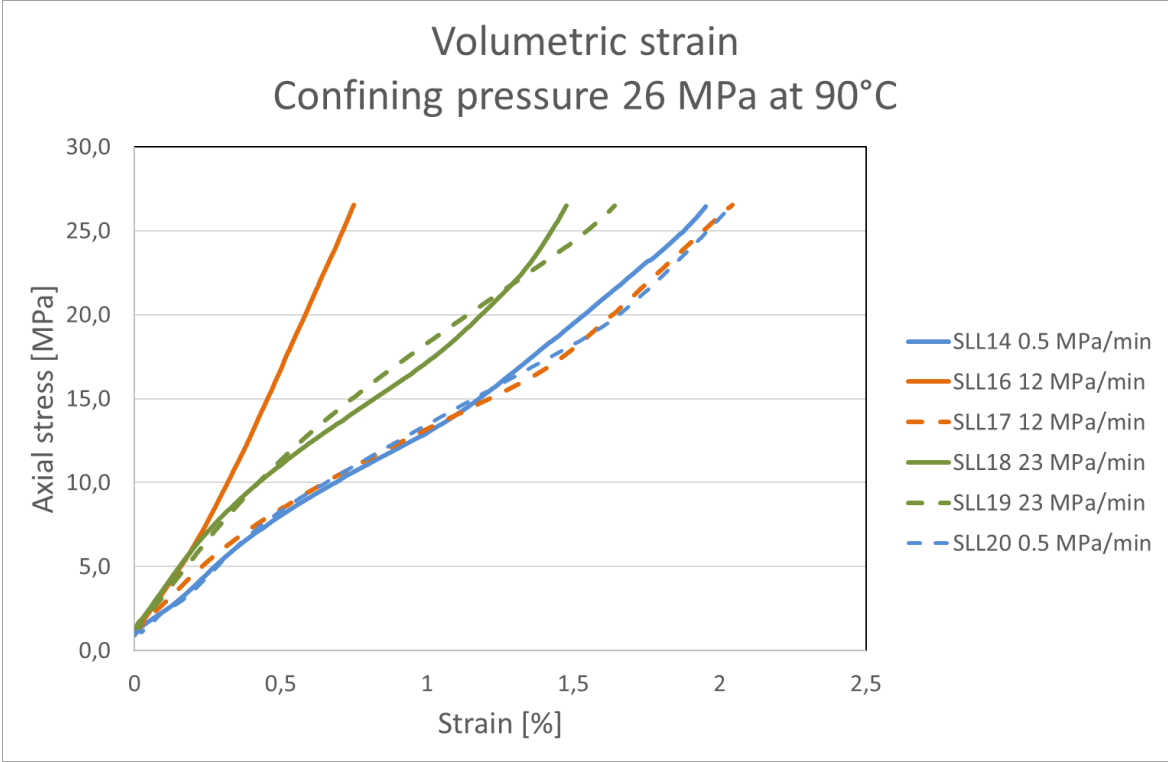


Figure 75 Volumetric strain for samples SLL14 to SLL20 with confining pressure of 26 MPa at an increase of 1.67 MPa/min

Figure 75 depicts the relationship between the axial strain and the volumetric strain for the samples tested at a confining pressure of 26 MPa. The volumetric strain values ranged from 0.74% to 2.04%. Consistent with the trends observed in Figure 73 and Figure 74, SLL16 stood out as an outlier with a volumetric strain of 0.74% and a more linear shape compared to the other samples.

In contrast, the remaining samples exhibited a more curved shape, which was the predominant trend observed in Figure 76. This indicates that the volumetric strain behaviour for the tested samples follows a consistent pattern, with SLL16 displaying a distinct response compared to the rest of the samples.

4.1.4 Discussion of the hydrostatic phase

Bulk modulus is a measurement of volumetric change in a material when the surrounding pressure increases. Which usually results in a decrease in volume, a compression of the material. Therefore, the more resistance a material is to volumetric change the higher the bulk modulus of the material is. At confining pressure 8 MPa the average bulk modulus was calculated to 1.58 GPa, for all 6 samples. With the higher confining pressures 17.2 MPa and 26 MPa, the average bulk modulus was calculated to be 1.77 (1.52 without extreme sample SSL1) GPa and 1.92 (1.6 without extreme sample SSL16) GPa. At higher hydrostatic stresses, it is observed that all cores exhibit increased stiffness, indicating an increase in bulk modulus.

The repeatability of the samples significantly improved after implementing a change to the procedure after samples SLL6 and SLL7. These changes were a change of grease, stirring after conditioning and stopping with the additional water on top of the samples. The samples with the initial procedure, got stuck and had to be forced out of the moulds. Which lead to the samples getting damaged with bobbled surface, as the test sample SLL4 in the below Figure 76. After the change of grease, the samples were easily removed from the moulds and had a smoother surface.



Figure 76 Picture of sample SLL4 (left) after removal from mould and sample SLL8 (right) sample cut and polished

Samples SLL14 and SLL18 had an extra day to cure at atmospheric pressure, room temperature in tap water and there not a sufficient increase in bulk modulus compared to their parallels SLL20 and SLL19.

The overall trend of the hydrostatic phase was the higher confining pressure, the more deformation for both axial and radial direction of the sample. Which is logical as there is more stress acting on the samples.

4.2 Deviatoric phase

The results from the deviatoric phase of the triaxial testing was divided into loading rates and confining pressure. This division was done to get a greater understanding of the effect of the loading rate on the JAW-B geopolymer. The samples were tested with a low piston loading rate of 0.5 MPa, medium piston pressure of 12 MPa/min and a high piston pressure between 17.98 to 23.3 MPa/min.

4.2.1 Piston load rate 0.5 MPa/min

Table 10 Results of test with piston loading rate 0.5 MPa/min

Test plug	Confining pressure [MPa]	Young's modulus [GPa]	Average Young's modulus [GPa]	Poisson's ratio	Compressive strength Deviatoric phase 0.2 % offset [MPa]	Average Compressive strength [MPa]
SLL6	17.2	0.72	0.61	0.32	21.5	21
SLL7	17.2	0.51		0.09	20.5	
SLL8	8	0.73	0.72	0.09	19	18
SLL9	8	0.71		0.13	17	
SLL14	26	1.01	1.05	0.31	34	34.75
SLL20	26	1.09		0.097	35.5	

Table 10 depicts the material strengths and properties derived from the data collected during the deviatoric phase for samples tested with a low loading rate. Excluding the samples tested with a confining pressure of 17.2 MPa, there is a trend of increase of strength when the

confining pressure increases. The young modulus increases from 0.72 GPa to 1.05 GPa, and the compressive strength increased from 18 MPa to 34.75 MPa.

4.2.1.1 Results of loading rate 0.5 MPa/min deviatoric

Figure 77 depicts the axial stress against the axial and radial strain for the samples tested with a load rate of 0.5 MPa/min. where the axial strain is depicted by the solid lines and the radial strain is depicted by the dotted line. A general trend between the axial and radial strain was the radial deviatoric strain was about 60% length of the axial. Which is to be expected as the axial stress is increased until the failure of the sample, while the surrounding pressure is maintained at a constant. The best repeatability is the SLL6 and SLL7 parallels shape wise, however the parallels at 8 MPa confining pressure had the best repeatability when it comes to the Young's modulus.

A strange behaviour was observed with the samples tested at 17.2 MPa confining pressure, the compressive strength was only 3 MPa more than the compressive strength of the samples tested at 8 MPa. The Young's modulus was also lower than the ones tested at 8 MPa. Compared to Figure 79 and

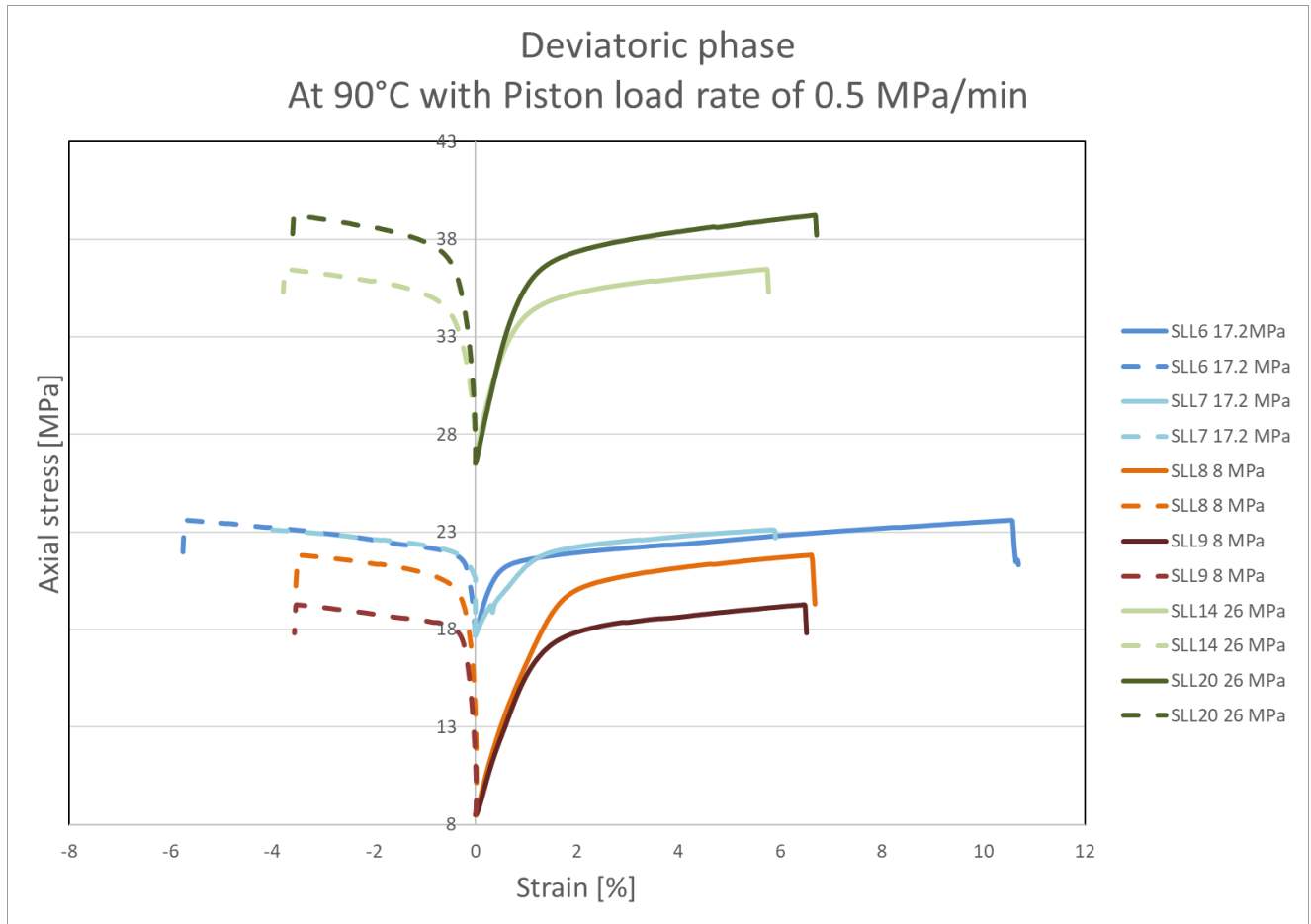


Figure 77 Deviatoric phase with piston load rate of 0.5 MPa/min with different confining pressures

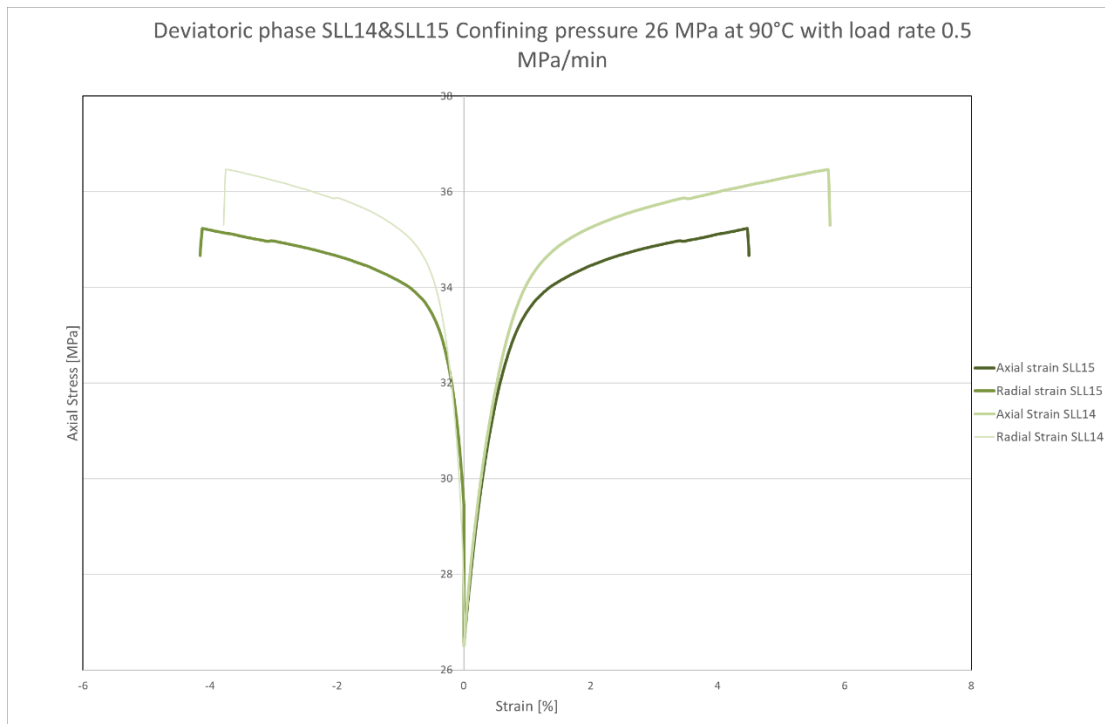


Figure 78 SLL14 and SLL15 deviatoric phase comparison

Figure 78 depicts the two parallels SLL14 and SLL15 and illustrates a good repeatability between the two. However, SLL15 was cut due to during the hydrostatic phase the extensometer read out of range. Therefore, there were no accurate readings for the parallels are more repeatable than the SLL14 and SLL20, although SLL15 was cut due to being out of range for the measurement for radial strain.

4.2.1.2 Discussion of the results of loading rate 0.5 MPa/min

Strange behaviour of SLL6-7, from the samples, lower confining pressure have a higher bulk modulus, while the Young's modulus is higher for the higher confining pressures. This can be due to the different load rate of the pumps, 0.5MPa/ min in the piston for the axial pressure increase and the 1.67 MPa/min for the confining pressure hoop and radial stress, which are equal.

As mentioned in the hydrostatic section, the difference between the sample left to cure for an extra day was not. The difference in young's modulus for samples SLL14 and SLL20, can be due to sample SLL20 being weaker.

4.2.2 Piston Load rate 12 MPa/ min

Table 11 Results of test with piston loading rate 12 MPa/min

Test plug	Confining pressure [MPa]	Young's modulus [GPa]	Average Young's modulus [GPa]	Poisson's ratio	Compressive strength Deviatoric phase 0.2 % offset [MPa]	Average Compressive strength [MPa]
SLL1	17.2	1.75	1.85	0.27	29	28
SLL2	17.2	1.95		0.31	27	
SLL10	8	1.09	1.29	0.17	19.5	20
SLL11	8	1.50		0.09	20.5	
SLL16	26	1.81	1.75	0.43	35.5	35.75
SLL17	26	1.70		0.38	36	

Table 11 relays the material strengths and properties of the geopolymer JAW-B tested with 12 MPa/min loading rate at three different confining pressures. As with Table 10 there was a trend of increased compressive strength, and Young’s modulus as the confining pressure increased from 8MPa to 26 MPa. The young’s modulus increased from 1.29 GPa to 1.75 GPa, and the compressive strength of the material increased from 20 MPa to 35.75 MPa

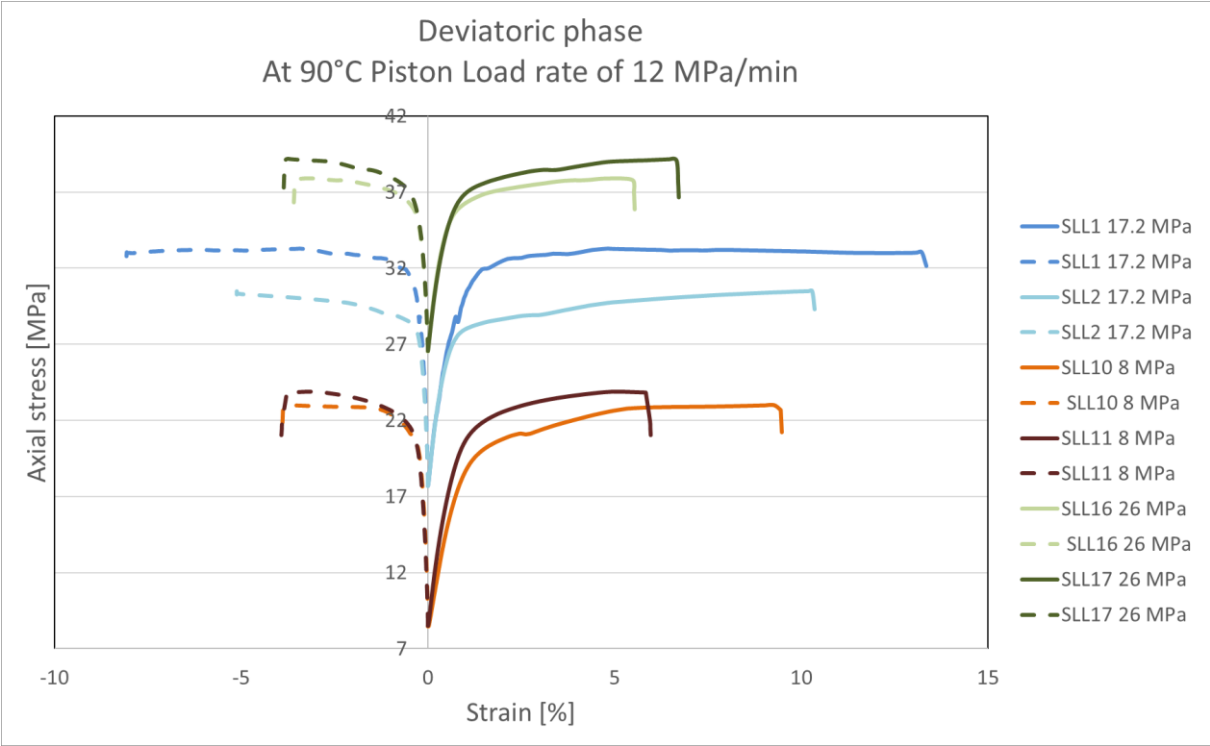


Figure 79 Deviatoric phase with Piston load rate of 12 MPa/min with different confining pressures

4.2.2.1 Results of loading rate 12 MPa/min

Figure 79 illustrates the samples response to the increased axial stress, in both axial and radial strain. Unlike Figure 77, the samples tested at a confining pressure of 17.2 MPa have a higher compressive strength gap between the samples tested at 8 MPa and 17.2 MPa compared (8 MPa difference) the samples in Figure 77.

4.2.2.2 Discussion of the results of loading rate 12 MPa/min

Trend of low young’s modulus and bulk modulus at a lower confining pressure. This could be due to less pressure for the applied axial stress to work against

4.2.3 Piston Load rate 17.97 to 23.3 MPa/min

Table 12 Results of test with piston loading rate between 17.97 to 23.3 MPa/min

Test plug	Piston load rate [MPa/min]	Confining pressure [MPa]	Young's modulus [GPa]	Average Young's modulus [GPa]	Poisson's ratio	Compressive strength Deviatoric phase 0.2 % offset [MPa]	Average Compressive strength [MPa]
SLL3	17.97	17.2	1.97	1.83	0.27	25.5	28
SLL4	21.58	17.2	1.70		0.31	30.5	
SLL12	19.15	8	1.15	1.21	0.41	17	18.25
SLL13	20.89	8	1.27		0.21	19.5	
SLL18	23.3	26	2.32	2.36	0.40	40	40.25
SLL19	23.2	26	2.40		0.38	40.5	

Table 12 relays the material strengths and properties of the geopolymer JAW-B tested with a loading rate between 17.97MPa/min to 23.3 loading rate at three different confining pressures. The loading differs between the samples as the Vindum high pressure pump were unable to pump at a rate of 35 MPa/min. Unlike Table 10 and Table 11 there was a trend of increased compressive strength and Young's modulus with increased confining pressure for all three pressures. The Young's modulus increased from 1.21 GPa to 2.36 GPa, and the compressive strength of the material increased from 18.25 MPa to 40.25 MPa. There is also a trend where the higher load rates yield in turn a higher yield strength (compressive strength). For example, sample SLL13 have a higher piston load rate of 20.89 MPa/min had a of 30.5 MPa which is 5 MPa larger than strength of sample SLL12. Samples SLL19 and SLL18 on the other hand had a similar load rate and compressive strength, Poisson's ratio and Young's modulus, as relayed in Table 12.

Figure 80, also illustrates how the load rate impact the material strengths of the samples as parallels with the largest difference in load rate (SLL3 and SLL4) also have the larger difference in yield stress. While samples SLL18 and SLL19 are very similar for both axial and radial strain. The trend of difference between the length between the axial and radial followed from Figure 79 and Figure 77, with the axial strain being larger than the radial.

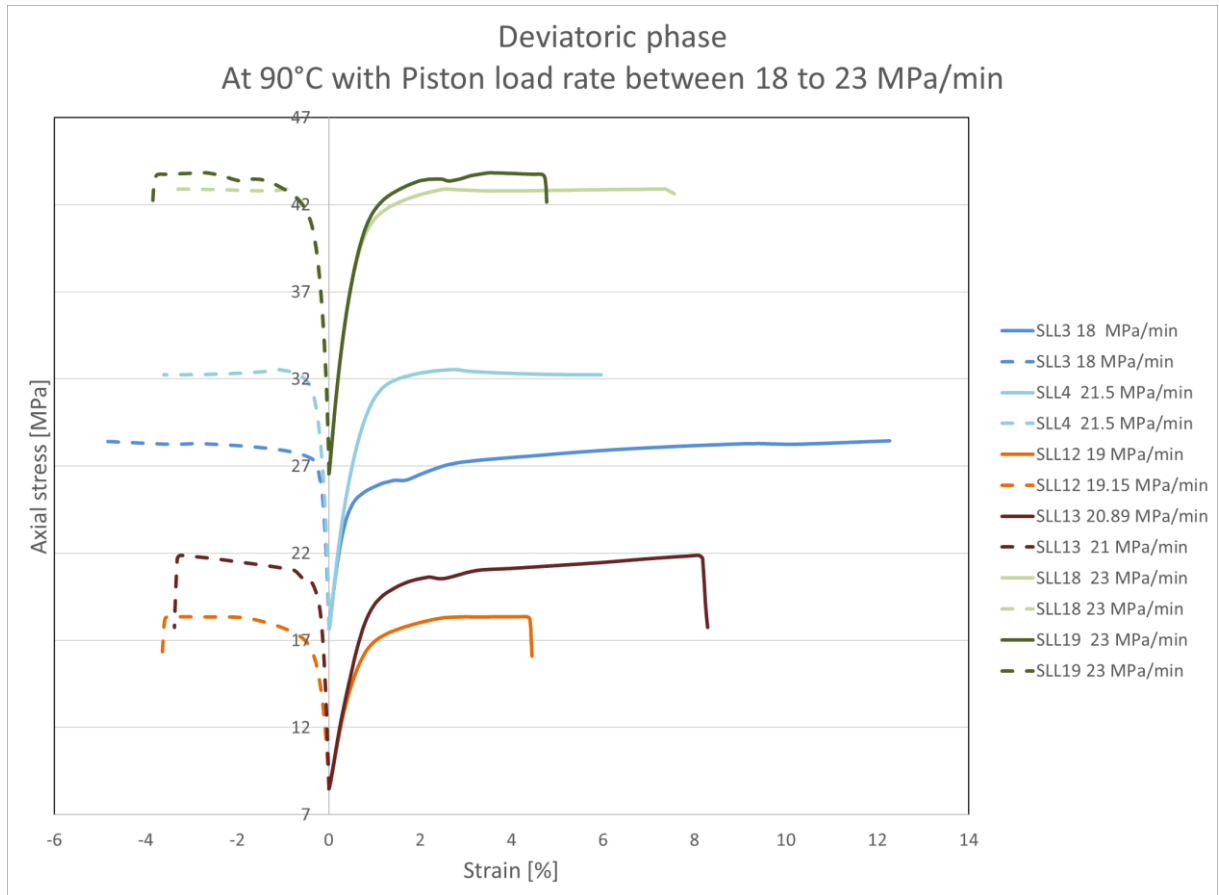


Figure 80 Deviatoric phase with Piston load rate between 17.97 to 23.3 MPa/min with different confining pressures
SLL13 is an outlier very high bulk modulus.

Difference in the results deviatoric phase might also be due to the load rates not being consistent. As since the piston pump was not able to reach 35 MPa/min and different due to the pump not being able to pump the set mode of 35 MPa/min, see the highest difference between the SLL3 and SLL4, while SLL12 and SLL13 have some difference, ref Figure 80 and Table 12. Then for the SLL18 and SLL19, where the piston pump rate is almost the same.

4.2.4 Different load rates at confining pressure 8 MPa

Table 13 Results of the deviatoric phase at 8 MPa confining pressure with different piston load rates

Test plug	Piston load rate [MPa/min]	Confining pressure [MPa]	Young's modulus [GPa]	Poisson's ratio	Compressive strength Deviatoric phase 0.2% offset [MPa]
SLL8	0.5	8	0.73	0.09	19
SLL9	0.5	8	0.71	0.13	17
SLL10	12	8	1.09	0.17	19.5
SLL11	12	8	1.50	0.09	20.5
SLL12	19.15	8	1.15	0.41	17
SLL13	20.89	8	1.27	0.21	19.5

Observe a strange behaviour, for the results in Figure 81 and Table 13. Since ideally the higher the piston load rate, the stiffer the material will reach to the increase in axial stress. Nonetheless, for this low confining pressure it looks like this is not the case for geopolymers samples at a confining pressure of 8 MPa. Where the compressive strength is higher for the samples tested with an axial stress increase of 12 MPa/min, and a sample tested with a load rate of 0.5 MPa/min surpassed the load increase rate of 19.15 MPa/min. This could be due to the sample SLL12 being weaker than sample SLL8. Further testing should be conducted to determine if this was due to a faulty sample or if geopolymers react differently at lower confining pressures, compared to a confining pressure of 17.2. which follows the logic high piston pump rate equals higher compressive strength of the geopolymer.

From Table 13 the Poisson's ratio exhibited a range of values from 0.9 to 0.41. Interestingly, an increase in piston load rate resulted in a higher value of Poisson's ratio. This implies that when axial load from the piston pump increases at a faster rate, the more elastic behaviour the samples displayed. This trend coincided with the corresponding increase of Young's modulus. However, sample SLL11 deviated from this trend with largest value of Young's modulus for but the lowest Poisson's ratio of 0.09. The deviation was also depicted in Figure 81, with the sample reaching the largest value of axial stress before failing.

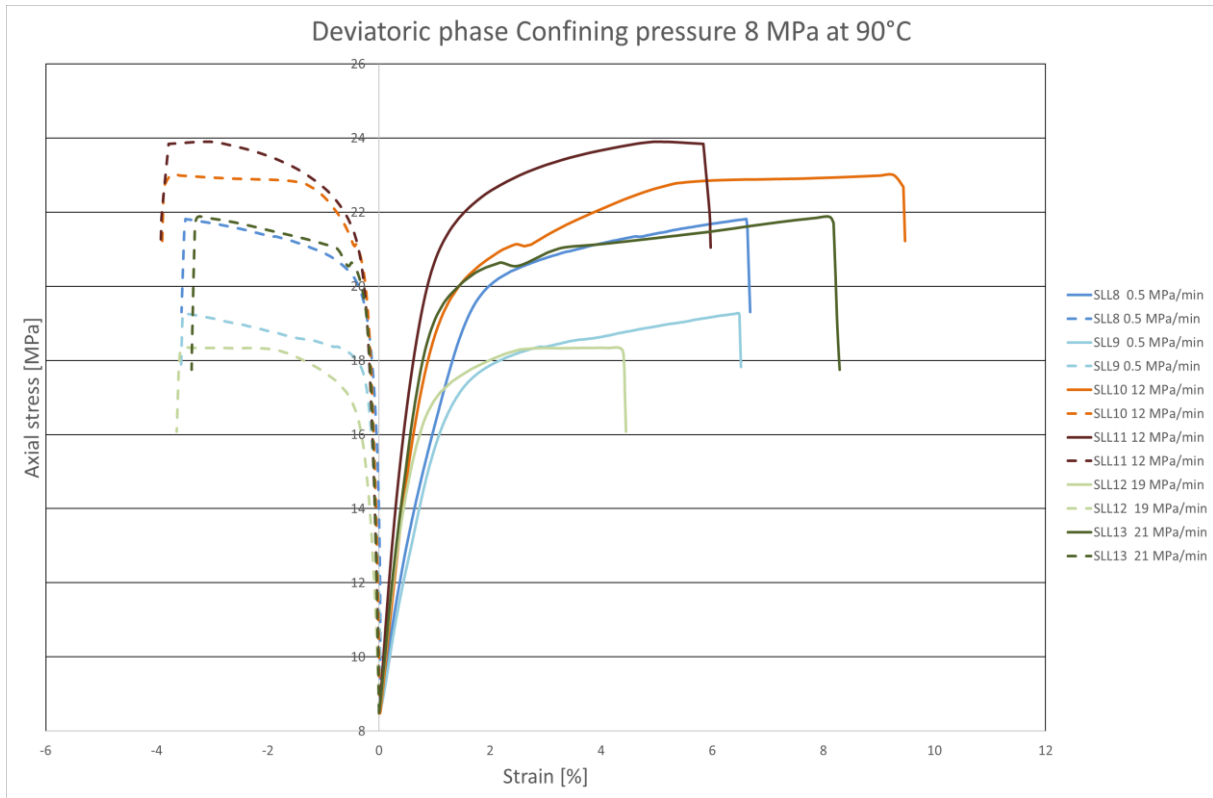


Figure 81 Deviatoric loading phase at 8 MPa with different piston loading rates

4.2.5 Different load rates at confining pressure 17.2 MPa

Table 14 Results of the deviatoric phase at 17.2 MPa confining pressure with different piston load rates

Test plug	Piston load rate [MPa/min]	Confining pressure [MPa]	Young's modulus [GPa]	Poisson's ratio	Compressive strength Deviatoric phase 0.2 % offset [MPa]
SLL1	12	17.2	1.75	0.27	29
SLL2	12	17.2	1.95	0.31	27
SLL3	17.97	17.2	1.97	0.27	25.5
SLL4	21.54	17.2	1.70	0.31	30.5
SLL6	0.5	17.2	0.72	0.32	21.5
SLL7	0.5	17.2	0.51	0.09	20.5

The results from Table 14 follows the trend of higher piston loading rate resulting in a higher compressive strength, expect for sample SLL3. At 17.2 MPa, the parallels tested with a load rate of 0.5 MPa/min showed a good repeatability for the compressive strength. Figure 82

illustrates the response to the increase of the axial stress. Together with the Table 14, Figure 82 shows the discrepancy with sample SLL1 and SLL3, which if it followed the trend of higher load rate equal higher compressive strength for the sample.

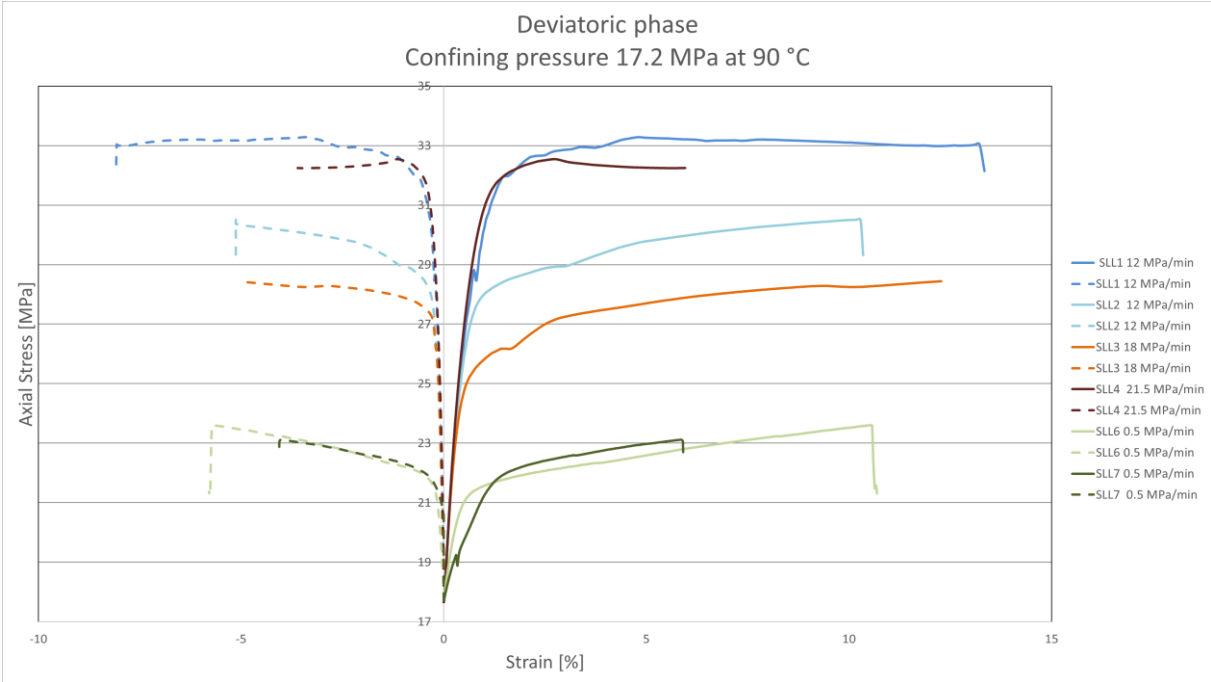


Figure 82 Deviatoric loading phase at 17.2 MPa with different piston loading rates

The Poisson’s ratio presented in Table 14 generally reaffirms the trend observed Table 13, where higher axial stress applied correlate to a larger Poisson’s ratio. The Poisson’s ratio ranged from a value of 0.9 to 0.32. An interesting finding from the collected data at a confining pressure of 17.2, the load rate of 0.5 MPa/min, is that the lowest and highest Poisson’s ratio. While higher piston loads, Poisson’s ratio ranged between 0.27 to 0.31. Thereby there is no clear change from a piston load rate of 12 to 21.5 MPa/min at 17.2 MPa.

4.2.6 Different load rates at confining pressure 26 MPa

Table 15 Results of the deviatoric phase at 26 MPa confining pressure with different piston load rates

Test plug	Piston load rate [MPa/min]	Confining pressure [MPa]	Young's modulus [GPa]	Poisson's ratio	Compressive strength Deviatoric phase 0.2 % offset [MPa]
SLL14	0.5	26	1.01	0.31	34
SLL20	0.5	26	1.09	0.09	35.5
SLL16	12	26	1.81	0.43	35.5
SLL17	12	26	1.70	0.38	36
SLL18	23.3	26	2.32	0.40	40
SLL19	23.2	26	2.40	0.38	40.5

From Table 15 the data presented, indicates a relationship between the samples compressive strength and increasing of piston load rate increased. As the increase from 0.5 MPa/min to 12 MPa/min resulted in a 2 MPa increase of compressive strength. Further, increasing the axial load rate (piston) increased the compressive strength to 40.5 MPa, a 4.5 MPa increase. Figure 83 also depicts the relation between the samples compressive strength, young's modulus and piston load rate.

Furthermore, the samples Young's modulus followed a similar trend, increasing from 1.01 to 2.40 GPa. Moreover, the observation from Table 15 follows Table 13's trend for Poisson's ratio and reaffirms the notion that a higher piston load rate results in a larger value of Poisson's ratio. Increasing from 0.09 to 0.43.

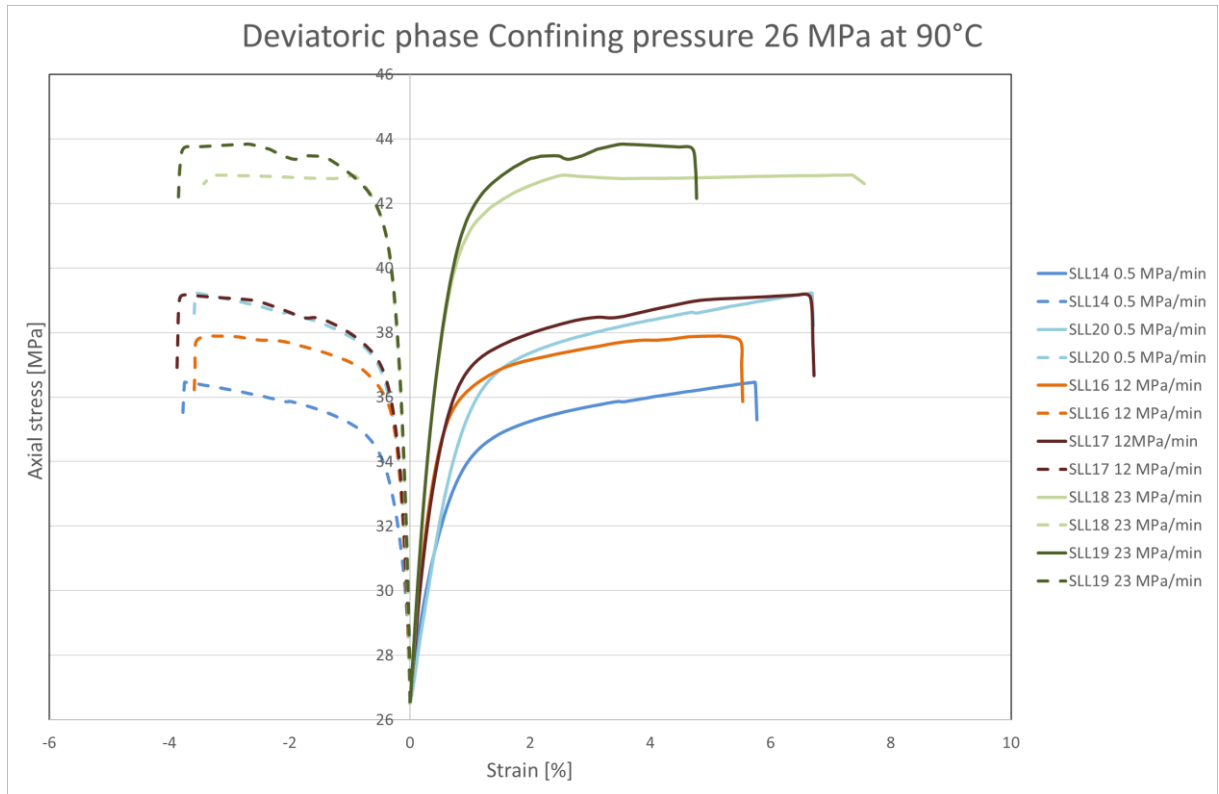


Figure 83 Deviatoric loading phase at 26 MPa with different piston loading rates

4.2.7 Discussion of the Deviatoric phase

The radial deviatoric strain is less than the axial, about 60% length of the axial. Which is to be expected. For the piston load rate of 0.5 MPa the best repeatability is the SLL6 and SLL7 parallels a trend after the change of procedure, after test samples SLL6 and SLL7, the Young's modulus increased.

The observed behaviour of the samples reveals an interesting trend, the lower confining pressures are associated with higher bulk modulus values, while higher confining pressures exhibit higher Young's modulus. This discrepancy can be attributed to the increase in the confining pressure, radial stress, which will work against the applied axial stress. Thereby increasing the stiffness of the material, which results in a higher Young's modulus.

For the samples tested at a load rate of 0.5 MPa/min, the confining pressures of 17.2 MPa and 8 MPa had similar Young's modulus of around 0.72 GPa. This result could be due to the low load rate or due to samples at confining pressure 17.2 MPa was weaker than the one tested at 8 MPa. Which is also reflected in the compressive strength which is also not

significantly larger than the samples tested at 8 MPa. At the highest confining pressure, the Young's modulus and compressive strength was more like the trend for the other loading rates 12 MPa/min and higher.

When considering the tests conducted at a load rate of 12 MPa/min, a trend emerges wherein lower confining pressures correspond to lower values of Young's modulus and bulk modulus. This could be attributed to the higher confining pressure working against the applied axial stress from the piston.

On the other hand, for tests conducted at load rates ranging from 17.97 to 23.3 MPa/min, certain observations stand out. Firstly, SLL13 displays an outlier with a remarkably high bulk modulus value. However, the other samples exhibit a trend wherein higher bulk modulus values correlate with higher Young's modulus values. Notably, SLL18 and SLL19 show better parallels, while SLL4 and SLL3 perform poorly, possibly due to the samples getting stuck as a result of inadequate choice of grease. This was reflected in the compressive strength values having a difference of 5 MPa. While for SLL18 and SLL19 the compressive strength has a difference of 0.5 MPa.

An important note is that the pump's inability to reach a rate of 35 MPa/min leads to a load rate range between 17.97 MPa/min and 23.3 MPa/min for the conducted tests. This is evident in the significant difference between SLL3 and SLL4, whereas SLL12 and SLL13 exhibit some variation. However, for SLL18 and SLL19, where the piston pump rate is nearly the same, the deviation was minimal.

Even though, samples SLL14 and SLL18 had an extra day to cure at atmospheric pressure, room temperature in tap water there was not a sufficient increase in compressive strength, bulk modulus at start compared to their parallels SLL20 and SLL19.

A sample of neat OPC class G was tested with a triaxial cell at confining pressure 17.2 MPa at 90°C with a piston load rate of 14 MPa/min by [Ogienagbonb, 2022]. The compressive strength of the OPC cement class G (NCG) was 67 MPa and a brittle failure with a Young's modulus over 8 GPa. Which is higher than all the samples of JAW-B tested. Sample SLL1 was tested with the close's conditions' as the OPC sample and the compressive

strength was found to be 29 MPa, Young’s modulus 1.75 GPa, and the failure mechanism was more ductile. A way to solve this gap of compressive strength is to add additives and retest the new mixture to see the change in mechanical properties.

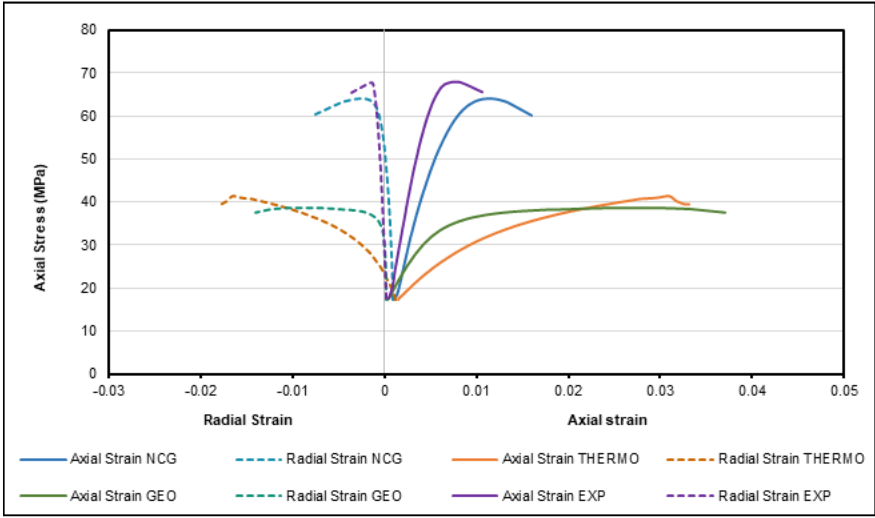


Figure 84 Deviatoric phase of Adijat Ogienagbonb’s study of mechanical behaviour of cementing materials [Adijat Ogienagbonb, 2022]

The data observed in Table 13, Table 14 and Table 15, suggest an overall consistent relationship between the piston load rate and an increase in the Poisson’s ratio of the samples. This increase in Poisson’s ratio can indicate that the samples are becoming more elastic. Allowing for more deformation without the sample suffering large changes to its shape.

4.3 Future improvement for testing JAW-B samples using a triaxial cell

For further investigation of JAW-B geopolymer, the direction of curing samples could be of interest. Changing the Autoclave curing cell from vertical to horizontal direction to see if the change in direction would have any effect on the strengths of the geopolymer. As it was observed that the failure of the samples occurred on the top section of the samples as pictured in Figure 45. Therefore, it could be interesting to see if the sample will be weaker on one half of the test sample cylinder. Further, the curing of the samples could be cured to the wanted test confining pressure to examine if there would be a large change in compressive strength, compared to curing the samples at 2000 psi. By changing the curing pressure could produce a result which simulate better the downhole conditions. An additional change to the curing procedure could be to change the tap water out for either Marcol 82 oil or fresh saltwater. The change to oil in the curing cell could remove the contamination effect from water and make the samples easier to remove from the moulds. While the salt water could be a better

alternative to simulate offshore downhole environments. Thereby, it would be possible to simulate how the geopolymer will cure in marine conditions for setting conductor casing.

Another interesting change could be to test the samples with a shorter length of 65mm and 55mm instead of the original 75mm. To investigate if the mineralogy in the samples changes and if this change will impact the samples bulk modulus to a notable degree. Forwards, changing the number of parallels from two to three might help increasing the repeatability, which was a problem during the hydrostatic loading phase for the radial and volumetric strain for all confining pressures.

During the testing of the 20 samples, the extensometer recording range was surpassed. Yielding results from two of the samples to be useless as half of the data was not logged, for those two samples. A calibration of the extensometer before the testing, could solve this issue, this calibration could be against a steel cylinder with a given circumference and be performed before placing the sample on the bottom of the triaxial cell. The calibration could also help with the repeatability of the samples together with testing three parallels.

As mentioned above the samples continued to fail on the top side of the sample, which was in contact with water during curing. It seems that the water could have mixed with the top slurry layers, thereby diluting the slurry and making the cement weaker at the top. To counter this the extensometer could be moved from the centre of the sample to closer to the bottom of the sample. Which was usually left untouched by the deformation from the deviatoric loading.

5. Conclusion

The thesis examines the influence of Loading Rate to the JAW-B mechanical properties. This was investigated by altering either the applied loading rate or the confining pressure and measuring the effect the alteration had on Young's modulus, the Poisson's ratio, Compressive strength, and the Bulk modulus.

Young's modulus:

Holding the piston load rate constant at **0.5 MPa/min**, increasing confining pressure from 8 MPa to 17.2 MPa, resulted in Young's modulus changing from a range of 0.71-0.73 GPa, to

0.51-0.72 GPa. Increasing confining pressure from 17.2 MPa to 26 MPa resulted an increase to 1.01-1.09 GPa.

Holding the piston load rate constant at **12 MPa/min**, increasing confining pressure from 8 MPa to 17.2 MPa, resulted in Young's modulus changing from a range of 1.09-1.50 GPa, to 1.75-1.95 GPa. Increasing confining pressure from 17.2 MPa to 26 MPa resulted an increase to 1.70-1.81 GPa.

Holding the piston load rate range of **17.97-23.3 MPa/min**, increasing confining pressure from 8 MPa to 17.2 MPa, resulted in Young's modulus changing from a range of 1.15-1.27 GPa, to 1.70-1.97 GPa. Increasing confining pressure from 17.2 MPa to 26 MPa resulted an increase to 2.32 -2.40 GPa.

When increasing the confining from 8 to 26 MPa the finding, shows an increase of young's modulus.

Holding the confining pressure constant at **8 MPa**, increasing piston loading rate from 0.5 MPa/min to 12 MPa/min, resulted in Young's modulus changing from a range of 0.71-0.73 GPa, to 1.09-1.50 GPa. increasing piston pressure load rate from 12 MPa/min to 19-21 MPa/min resulted an Increase to 1.15-1.27 GPa.

Holding the confining pressure constant at **17.2 MPa**, increasing piston loading rate from 0.5 MPa/min to 12 MPa/min, resulted in Young's modulus changing from a range of 0.51-0.72 GPa, to 1.75-1.95 GPa. Increasing piston pressure load rate from 12 MPa/min to 19-21.5 MPa/min resulted an increase to 1.70-1.97 GPa.

Holding the confining pressure constant at **26 MPa**, increasing piston loading rate from 0.5 MPa/min to 12 MPa/min, resulted in Young's modulus changing from a range of 1.07-1.09 GPa, to 1.70-1.81 GPa. increasing piston pressure load rate from 12 MPa/min to 23 MPa/min resulted an Increase to 2.32-2.40 GPa.

When increasing the piston pressure load rate from 0.5 to 23 MPa/min, the findings a similar trend as increasing the confining pressure an increase of Young's modulus. Where the

weakest was 0.71-0.73 MPa the lowest confining pressure and the piston load rate (8 MPa, 0.5 MPa/min) and the stiffest 2.32-2.40 MPa at the highest confining pressure and piston loading rate (26 MPa, 23 MPa/min) (note that samples at 17.2 were damaged during sample creation)

Overall, the findings suggest that increasing the confining pressure or the piston loading rate generally leads to an increase in Young's modulus, indicating a stiffer material with higher elastic properties. However, it is important to note that the damaged samples at 17.2 MPa confining pressure limit the complete assessment of Young's modulus under that condition.

Poisson's ratio:

Holding the piston load rate constant at **0.5 MPa/min**, increasing confining pressure from 8 MPa to 17.2 MPa, resulted in Poisson's ratio changing from a range of 0.09-0.13, to 0.09-0.32. increasing confining pressure from 17.2 MPa to 26 MPa resulted a decrease to 0.09-0.31.

Holding the piston load rate constant at **12 MPa/min**, increasing confining pressure from 8 MPa to 17.2 MPa, resulted in Poisson's ratio changing from a range of 0.09-0.17, to 0.27-0.31. increasing confining pressure from 17.2 MPa to 26 MPa resulted an increase to 0.38-0.43.

Holding the piston load rate constant at **17.97-23.3 MPa/min**, increasing confining pressure from 8 MPa to 17.2 MPa, resulted in Poisson's ratio changing from a range of 0.21-0.41, to 0.27-0.31. increasing confining pressure from 17.2 MPa to 26 MPa resulted an increase to 0.38-0.40.

Increasing the confining pressure to 26 MPa for 12 and 18-23 MPa/min showed an increase in Poisson's ratio with an increase in confining pressure, however this was not the trend at not the case for the load rate of 0.5 MPa/min, were there was no noticeable change from the increase confining pressure from 17.2 to 26 MPa.

Holding the confining pressure constant at **8 MPa**, increasing piston loading rate from 0.5 MPa/min to 12 MPa/min, resulted Poisson's ratio changing from a range of 0.09-0.13, to

0.09-0.17. increasing piston pressure load rate from 12 MPa/min to 19-21MPa/min resulted an increase to 0.21-0.41.

Holding the confining pressure constant at **17.2 MPa**, increasing piston loading rate from 0.5 MPa/min to 12 MPa/min, resulted Poisson's ratio changing from a range of 0.09-0.32, to 0.27-0.31. increasing piston pressure load rate from 12 MPa/min to 19-21MPa/min resulted an "increase" to 0.09-0.32.

Holding the confining pressure constant at **26 MPa**, increasing piston loading rate from 0.5 MPa/min to 12 MPa/min, resulted Poisson's ratio changing from a range of 0.09-0.31, to 0.38-0.43. increasing piston pressure load rate from 12 MPa/min to 19-21MPa/min resulted a decrease to 0.38-0.40.

Overall, the analysis indicates that changes in both confining pressure and piston loading rate can affect Poisson's ratio, suggesting that the test samples become more ductile with higher applied stress. However, the observed trends were not consistent and depended on the specific combinations of confining pressure and piston loading rate.

Compressive strength:

Holding the piston load rate constant at **0.5 MPa/min**, increasing confining pressure from 8 MPa to 17.2 MPa, resulted in Compressive strength changing from a range of 17-19 MPa, to 20.5-21.5 MPa increasing confining pressure from 17. 2 MPa to 26 MPa resulted a decrease to 34-35.5 MPa.

Holding the piston load rate constant at **12 MPa/min**, increasing confining pressure from 8 MPa to 17.2 MPa, resulted in Compressive strength changing from a range of 19.5-20.5 MPa, to 27-29 MPa. increasing confining pressure from 17. 2 MPa to 26 MPa resulted an increase to 35.5-36 MPa

Holding the piston load rate constant at **17.97-23.3 MPa/min**, increasing confining pressure from 8 MPa to 17.2 MPa, resulted in Compressive strength changing from a range of 17-19.5 MPa, to 25.5 to 30.5 MPa. increasing confining pressure from 17. 2 MPa to 26 MPa resulted an increase to 40-40.5 MPa.

Increase in confining pressure resulted in a trend of an increase in compressive strength. This could be due to there being more pressure(=stress) for the axial stress applied on the sample by the piston.

Holding the confining pressure constant at **8 MPa**, increasing piston loading rate from 0.5 MPa/min to 12 MPa/min, resulted Compressive strength changing from a range of 17-19 MPa, to 19.5-20.5 MPa. increasing piston pressure load rate from 12 MPa/min to 19-21MPa/min resulted a decrease to 17-19.5 MPa. (Values like the ones for the slow loading rate)

Holding the confining pressure constant at **17.2 MPa**, increasing piston loading rate from 0.5 MPa/min to 12 MPa/min, resulted Compressive strength changing from a range of 20.5-21.5, to 27-29 MPa. increasing piston pressure load rate from 12 MPa/min to 19-21MPa/min resulted an “increase” to 25.5-30.5 MPa.

Holding the confining pressure constant at **26 MPa**, increasing piston loading rate from 0.5 MPa/min to 12 MPa/min, resulted Compressive strength changing from a range of 34-35.5, to 35.5-36 MPa. increasing piston pressure load rate from 12 MPa/min to 19-21MPa/min resulted a decrease to 40-40.5 MPa.

Overall, the results indicates that changes in both confining pressure and piston loading rate can affect the compressive strength of geopolymers. Higher confining pressures generally led to increased compressive strength, while the effect of piston loading rate was more variable and depended on other factors.

Bulk modulus

Required at a constant confining pump rate of 1.67 MPa/min, the average bulk modulus was for confining pressure 8 MPa $K = 1.58$ GPa, 17.2 MPa $K = 1.77$ GPa, 26 MPa $K = 1.92$. this showed an increase in bulk modulus as the confining pressure increases from 8 to 26 MPa. meaning the samples needed more stress in order to change their cylindrical shape. The analysis indicates that the bulk modulus of JAW-B increases as the confining pressure is raised from 8 to 26 MPa. This suggests that the JAW-B become less compressible and more resistant to changes in shape or volume under higher confining pressures.

Even though, samples SLL14 and SLL18 had an extra day to cure at atmospheric pressure, room temperature in tap water there was not a large change in compressive strength, bulk modulus compared to their parallels SLL20 and SLL19. Where there is a notable difference is to the Young's modulus. Therefore, there is no significant impact to the material strength for the sample to cure for one extra day at standard conditions.

The study provides a foundation for further testing, and JAW-B ought to be tested against OPC benchmark properties to compare results. This would further the validity of the results to see if it can be a viable alternative to OPC in well cementing. Thus, further testing of the JAW-B geopolymer is warranted to further determine the impact of low and high piston load rate at different confining pressures.

References

Adijat Ogienagbon; Mahmoud Khalifeh, Adijat Ogienagbon; Mahmoud. 2022. Research. *Experimental Evaluation of the Effect of Temperature on the Mechanical Properties of Setting Materials for Well Integrity*. SPE Journal 27 (05): 2577-2589. SPE209794

Bellarby, Jonathan. 2009. *Well Completion Design*, Vol. 56: Developments in Petroleum Science, Elsevier. ISBN: 978-0-444-53210-7.

Benjamin C. McLellan, Ross P. Williams, Janine Lay, Arie van Riessen, Glen D. Corder. 2011. *Costs and carbon emissions for geopolymer pastes in comparison to ordinary Portland cemen*, Journal of Cleaner Production, Volume 19, Issues 9–10, Pages 1080-1090. ISSN 0959-6526, <https://doi.org/10.1016/j.jclepro.2011.02.010>.

William D. Callister, Jr., David G. Rethwisch. 2014. *Material Science and Engineering SI version*, Ninth edition, 481-482; 543-545. Singapore: John Wiley & Sons (Asia) Pte Ltd (Wiley). ISBN 978-1-118-31922-2

Colin McPhee, Jules Reed, Izaskun Zubizarreta. 2015. *Core Analysis: A Best Practice Guide*, Chapter 12 - Geomechanics Tests, Developments in Petroleum Science, Volume 64,

Pages 671-779, Elsevier. ISSN 0376-7361, ISBN 9780444635334,
<https://doi.org/10.1016/B978-0-444-63533-4.00012-3>.

Crumpton, Howard. 2018. *Well Control For Completions and Intervention*, 65-85: Golf Professional Publishing. ISBN: 978-0-08-100196-7.

Dominick Rosato, Donald Rosato. 2003. *Plastics Engineered Product Design*, chapter 3 – Design Parameter, Elsevier Science, pages 161-197. ISBN 9781856174169,
<https://doi.org/10.1016/B978-185617416-9/50004-1>.

Erling Fjær, Rune Martin Holt, Per Horsrud, Arne Marius Raaen, Rasmus Risnes. 2008. *Petroleum Related Rock Mechanics*, 2nd edition, Vol. 72: Developments in Petroleum Science, Elsevier, Chapters 1, 4, 7 and 12. ISBN 978-0-444-50260-5.

Giasuddin, Haider M, Sanjayan, Jay G, and Ranjith, PG. 2013. *Stress versus strain behavior of geopolymer cement under triaxial stress conditions in saline and normal water*. Fuel, Volume 107, pages 521-524. ISSN 0016-2361,
<https://doi.org/10.1016/j.fuel.2013.01.035>.

Hibbeler, R.C. 2014. *Mechanics of Materials SI Edition*, Ninth edition, pages 25-26, 68, 85-89, 92-93, 104. Pearson Education South Asia Pte Ltd. ISBN 978-981-06-9436-4.

T. Hemalatha, Ananth Ramaswamy, 2022, *Handbook of Fly Ash*, chapter 18 – Fly Ash, Butterworth-Heinemann, Pages 547-563, ISBN 9780128176863,
<https://doi.org/10.1016/B978-0-12-817686-3.00016-5>.

J. Davidovits. 2013. Geopolymer Cement: A Review. Geopolymer Science and Technics Technical Paper #21, 1-11. www.geopolymer.org.

Liu, Xiangyu, Aughenbaugh, Katherine, Nair, Sriramy, Shuck, Michelle, and Eric van Oort. 2016. *Solidification of Synthetic-Based Drilling Mud Using Geopolymers*. Paper presented at the SPE Deepwater Drilling and Completions Conference, Galveston, Texas,

USA, September 2016. Paper Number: SPE-180325-MS, doi: <https://doi.org/10.2118/180325-MS>.

Mahmoud Khalifeh, Arild Saasen. 2020. *Introduction to Permanent Plug and Abandonment of Wells*: Ocean Engineering & Oceanography, Springer Open. ISBN 978-0-03-39969-6

NORSOK standard D-10. 2021. *Well integrity in drilling and well, operations*, Standards Norway.

Schlumberger. 2006. *Well Cementing*, Second edition, pages 23-27; 30-31; 36-39, 51-53. 225 Schlumberger Drive Sugar Land Texas 77478 USA: Schlumberger, ISBN 978-097885300-6